Electronic Doping and Trap Reduction of Quantum Dots

Amanda Leigh Thorsen

A dissertation
submitted in partial fulfillment of the
requirements for the degree of

Doctor of Philosophy

University of Washington
2014

Reading Committee:
Daniel R. Gamelin, Chair
Bo Zhang
Dennis M. Heinekey

Program Authorized to Offer Degree:
Chemistry

University of Washington

Abstract

Electronic Doping and Trap Reduction of Quantum Dots

Amanda Leigh Thorsen

Chair of the Supervisory Committee:
Professor Daniel R. Gamelin
Department of Chemistry

Both undoped and doped semiconductor quantum dots (QDs) offer unique opportunities for studying the fundamental physics of quantum confinement. Obtaining a thorough understanding of their physical properties is necessary for development of efficient and robust materials for use in a wide range of applications such as optoelectronics (optical switches, light emitting diodes (LEDs), photovoltaics, and lasers), biosensing, and nanoelectronics. This thesis involves studies that look specifically at the effects of electronic doping and trap reduction in undoped and Mn^{2+}-doped QDs. Investigation of the effect of electron-Mn^{2+} exchange interactions on Mn^{2+} luminescence in Mn^{2+}:CdS nanocrystal films through an electrochemical method reveals effective Auger de-excitation of photoexcited Mn^{2+}. The doped QDs demonstrate increased sensitivity to Auger de-excitation *versus* undoped QDs due to the long lifetime of the Mn^{2+} excited state. Photochemical electronic doping of colloidal CdSe nanocrystals is achieved for the first time through the use of a borohydride hole quencher, Li[Et_3BH], and the high spectroscopic quality of the resulting *n*-type nanocrystals allows for advanced characterization by absorption and photoluminescence. Additionally, chemical titrations of the *n*-type nanocrystals confirm electron accumulation and suggest significant electron trapping for some of the nanocrystals. Spectroelectrochemical measurements on undoped and Mn^{2+}-doped ZnSe QDs target charge injection into traps within the semiconductor bandgap. In both the undoped and doped QDs, transfer of electrons into the nanocrystal film is

directly correlated with enhanced photoluminescence quantum yield and dubbed “electrobrightening.” This method of brightening through trap passivation is extended to colloidal systems through the use of outer-sphere reductants and ultimately improves the ensemble photoluminescence quantum yield of Mn^{2+}-doped ZnSe QDs from 14% to 80%.

Table of Contents

List of Figures

List of Abbreviations

E_g	bandgap energy
CB	conduction band
e^-_{CB}	conduction band electron
CV	cyclic voltammagram
DMS	diluted magnetic semiconductor
DMF	dimethylformamide
EB	electrobrightening
EL	electroluminescence
FTO	fluorine doped tin oxide
HOMO	highest occupied molecular orbital
IR	infrared
LED	light emitting diode
LUMO	lowest unoccupied molecular orbital
MCD	magnetic circular dichroism
MPTMS	3-mercaptopropyl-trimethoxysilane
NC	nanocrystal
ODE	octadecene
OA	oleic acid
PB	photobrightening
PL	photoluminescence
PLE	photoluminescence excitation
PC	propylene carbonate
QD	quantum dot
QY	quantum yield
TBAP	tetrabutylammonium perchlorate
THF	tetrahydrofuran
ITO	tin doped indium oxide
TOP	tri-octyl-phosphine
TOPO	tri-octyl-phoshpine oxide
UV/Vis	ultraviolet/visible
VB	valence band
h^+_{VB}	valence band hole
XRD	x-ray diffraction

Acknowledgments

I would like to express my deepest gratitude towards those who have supported me through this academic journey. I would like to especially thank Professor Daniel Gamelin for his excellent mentorship. His enthusiasm, scholarly guidance, and support over the years had a profound effect on my pursuit of a PhD. I am extremely grateful for the former and current members of the Gamelin group who have been excellent sources of knowledge and friendship both at work and at various establishments all over Seattle. In addition, I would like to thank the faculty and staff at the Department of Chemistry for their support and assistance. Finally, my success over the last few years would not have been possible without the undying love and support of my family and boisterous friends who have guided me through both misfortune and merriment.

The Gamelin Group:

Prof. Daniel R. Gamelin	Dr. Pradip Chakraborty	G. Z. (Mike) Carroll
Prof. Victor Polinger	Dr. Kelly Whitaker	Charles Barrows
Prof. Rémi Beaulac	Dr. Claire Johnson	Kimberly Hartstein
Prof. Kevin R. Kittilstved	Dr. Michael White	Heidi Nelson
Prof. Andreas Hauser	Dr. Diane Zhong	Katherine Bryant
Dr. Stefan Ochsenbein	Dr. Alicia Cohn	Rob Johns
Dr. Nils Janßen	Dr. Vladimir Vlaskin	Brigit Miller
Dr. Jillian Dempsey	Curtis Deer	Troy Kilburn
Dr. Emily McLaurin	Alina Schimpf	Michael De Siena
Dr. Jeffrey Rinehart	Liam Bradshaw	Carolyn Gunthardt
Dr. Kathyrn Knowles	Patrick Whitham	Xing Yee Gan

Dedication

To my parents,

for always believing in me,

and to Tyler,

for his encouragement and lasting love.

Chapter 1

Charging in Semiconductor Nanocrystals

1.1 Introduction to Colloidal Quantum Dots

Over the last few decades, semiconductors have provided the basis for much of our modern technology including transistors, solar cells, and light-emitting diodes. In semiconductors, electrical conductivity arises when electrons occupy states that are delocalized across the material. Control over the number of carriers in these materials allows for their physical properties to be tailored for specific applications. Semiconductor conductivity changes with the introduction of impurity dopants or by interaction with an electric field or light. Photoexcitation of a semiconductor will promote an electron from the valence band (VB) to the conduction band (CB), leaving behind a hole in the valence band. This electron-hole pair, or exciton, will recombine and emit as either photons (radiation) or phonons (thermal energy).

The exciton Bohr radius is determined by the coulombic interaction between the electron and the hole, and is usually on the order of a few nanometers. In bulk semiconductors, the exciton is able to move freely in all directions. Reducing the size of the semiconductor material to the same order as the exciton Bohr radius causes quantum confinement of the exciton and alters the semiconductor electronic structure.[1]

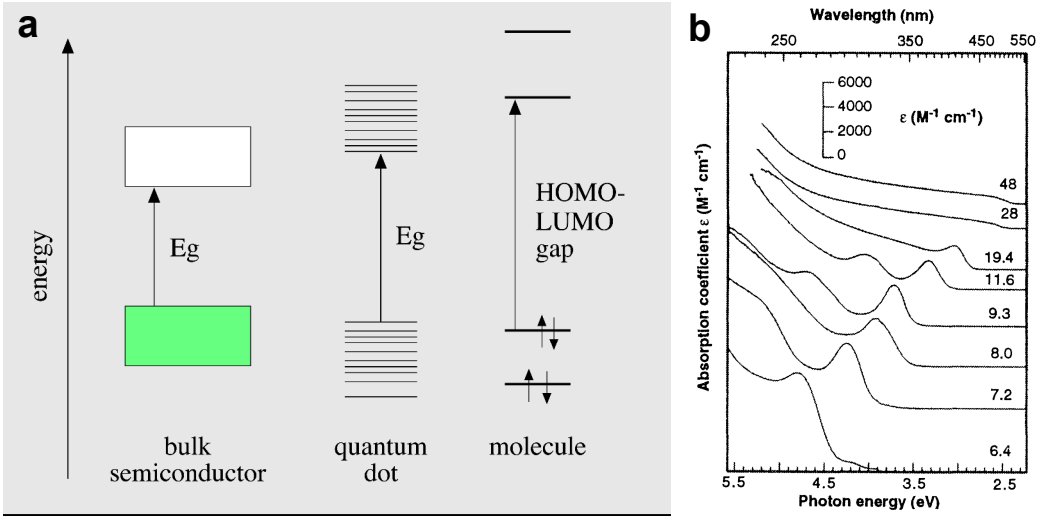

Figure 1.1: The effects of quantum confinement on semiconductor electronic structure. **(a)** Energy level diagram comparing a bulk semiconductor, a QD, and a molecular cluster. The bulk semiconductor has delocalized electrons in bands whereas the molecule has electrons in molecular orbitals. The bandgap energy (E_g) in the bulk semiconductor and QD is analogous to the HOMO-LUMO energy gap in the molecule. (b) The absorption spectra for a series of CdSe nanocrystals. As the size of the nanocrystal is reduced, the spectra shift to higher energy. Adapted from Ref. 2 and 3.

Quantum confined colloidal semiconductor nanocrystals, or quantum dots (QDs), continue to provide cross-disciplinary interest for the fields of chemistry, physics, and engineering due to their processing flexibility and unique optical and electronic properties. Three dimensional confinement of the exciton causes the optical, physical, and chemical properties of QDs to be sensitive to the size of the nanocrystal. As the exciton becomes more confined, the splitting between the energy levels of the CB and VB increases, and thereby the bandgap – the energy splitting between the highest energy level of the VB (HOMO) and the lowest energy level of the CB (LUMO) – increases significantly with decreasing nanocrystal size (see Figure 1.1). The onset of light absorption for the first exciton occurs at the bandgap energy (E_g) and will red-shift (shift to lower energy) with increasing size. Similarly, the radiative emission of the exciton will red-shift with increasing size. Consequently, absorption and photoluminescence (PL) measurements of QDs are utilized frequently as tools for probing the electronic structure and physical characteristics of QDs. Colloidal bottom-up processing facilitates size manipulation and allows for wet-chemical applications that also improve

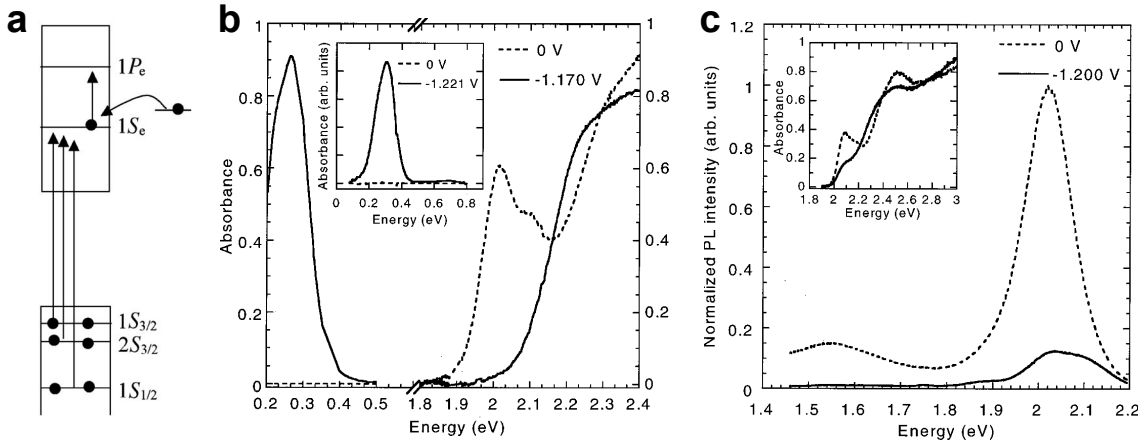

Figure 1.2: Optical spectroscopic signatures of introducing e^-_{CB} into QDs. **(a)** A schematic diagram of the optical transitions involved in electron transfer. **(b)** IR and UV/Vis absorption spectra of a 5.8 nm CdSe QD film at different potentials. At 0 V the QD film is neutral. At -1.170 V, electrons are injected into the CB of the QD film causing the bleach of the first excitonic transition and the appearance of an intra-band mid-IR peak. **(Inset)** IR absorption spectra of a 5.0 nm CdSe QD film at different potentials. **(c)** PL spectra of a 5.0 nm CdSe QD film at different potentials. **(Inset)** Simultaneously recorded UV/Vis spectra of the film showing a 50% bleach corresponding to an average of one e^-_{CB} per QD. Adapted from Ref. 7 and 8.

scalability and reduce cost manufacturing.

1.2 Charge Injection

1.2.1 Spectroscopic Signatures

The introduction of free charge carriers into QDs has a profound effect on many of their physical properties.[4] The injection of either a conduction band electron (e^-_{CB}) or a valence band hole (h^+_{VB}) will have similar effects on the optical properties.[5] It has been shown that introduction of a charge carrier will partially fill the lowest energy level of the corresponding band ($1\mathrm{S}_e$ for e^-_{CB} and $1\mathrm{S}_h$ for h^+_{VB}) and lead to a bleach in the first excitonic transition[6] (Figure 1.2). Two electrons can occupy the $1\mathrm{S}_e$ energy level, therefore injection of one electron per QD corresponds to a 50% bleach of the first excitonic transition, and 2 electrons per QD corresponds to a 100% bleach.

A second characteristic feature in the electronic absorption of "charged" QDs is the appearance

of a new intra-band transition. A QD with an electron in the $1S_e$ energy level can absorb infrared (IR) light to promote the electron to the $1P_e$ energy level. The energy of the IR absorption has been shown to be dependent on QD size.[9] Figure 1.2 shows a schematic diagram and corresponding spectra of the optical transitions affected by introduction of a e^-_{CB}. The presence of the IR peak and first excitonic bleach in electronic absorption are considered reliable signatures for the existence of at least one delocalized carrier per QD. Additional higher energy carriers will produce similar higher energy bleaches of the excitonic absorption and increased intensity of the intra-band transition absorption. Removal of e^-_{CB} by reoxidation results in a concurrent full recovery of the absorption bleach and disappearance of the IR peak.[4,6]

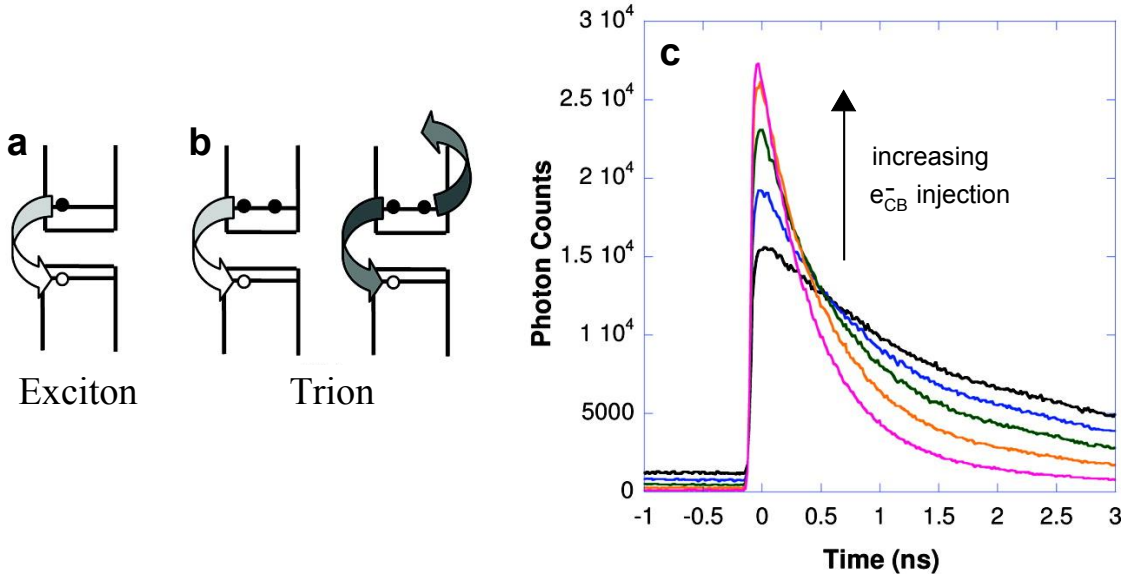

Figure 1.3: Trion decay in charged QDs. (a) A schematic diagram comparing radiative recombination of an exciton and nonradiative trion Auger recombination. (b) Time-resolved PL spectra of a CdSe/CdS QD thin-film at different charging levels. Adapted from Ref. 10.

When a QD with a free charge carrier is photoexcited, a new nonradiative recombination pathway becomes available. The recombination of the exciton can result in fast energy transfer to the free charge carrier to promote it to a higher energy level in the band[6] (Figure 1.3a). This mechanism, referred to as trion Auger de-excitation, is fast compared to excitonic emission and will effectively quench radiative emission.[10,11] Figure 1.2c shows an example of PL quenching in a

QD film charged by electrochemical charge injection (see Section 1.2.3). In Figure 1.3 the time-resolved PL for charged QDs decays faster than the neutral QDs due to the appearance of a fast component attributed to the increased rate of nonradiative Auger recombination of the trion.[10] The increased PL at short times comes from a fast radiative process between the exciton and the e^-_{CB} (trion emission) that is competitive with trion Auger recombination.

While PL quenching can be used to monitor the reduction of QDs, full recovery of the PL happens long after all of the e^-_{CB} have been removed from the QD. It has been proposed that trapped electrons in surface states can lead to an alternative PL quenching mechanism[6] (see Section 1.3). Changes in the optical absorption are synchronous with e^-_{CB} removal and therefore allow confirmation of QD reoxidation during PL measurements.

1.2.2 Chemical & Photochemical

One of the most direct methods of charge injection is by exposure to chemical reductants such as sodium metal or biphenyl radical.[4,6] Anhydrous suspensions of CdSe QDs charged with biphenyl radical were found to be stable over the course of many weeks at 20 K, but at room temperature the intra-band transition peak decays within 30 minutes to 24 hours.[4] Intentional exposure to air results in reoxidation within minutes and shows that charging is easily and fully reversible.[4] After reoxidation, the QDs can be reduced again upon reexposure to reducing agent. Since charged QDs can be easily oxidized by O_2 and water,[4,5,12,13] most methods of stable charge injection are conducted in anyhydrous solvents and under inert atmosphere to prevent reoxidation.

Chemical reduction is limited to systems where the reducing potential of the reductant is large enough to directly reduce the $1S_e$ CB level. An alternative approach involves photoexcitation of the QD to yield an exciton and subsequent reduction of the h^+_{VB} by a weak reducing agent (such as ethanol) to yield a free electron.[13–15] Historically, this method was used with ZnO and TiO_2 QDs[6,15–17] and only recently has been extended to chalcogenide QDs (see Chapter 3). When using either of these methods, the possiblity of reducing electron surface traps on colloidal QDs makes

it difficult to distinguish the number of electrons injected into traps *versus* the CB.

1.2.3 Electrochemical

Electrochemical charge injection has been one of the more popular methods of introducing charge carriers into QDs due to the ease of control over the number of charge carriers in the QDs and the ability to distinguish between reduction of surface traps and reduction of the CB.[18] While initial studies looked at colloidal suspensions of QDs,[12] studies on QD thin-films quickly took precedence as they provide better control over the charge carrier density, faster response times, and improved stability to rogue oxidants.[5,8,19–25] Typical spectroelectrochemical cells consist of an anhydrous solvent (such as THF, DMF, or PC) with 0.1 M TBAP as supporting electrolyte, a platinum counter electrode and a silver pseudo-reference electrode.[8,12] A platinum or gold disc working electrode was originally used in combination with reflectance spectroscopy to monitor absorption and PL changes in charged colloidal QD suspensions[12] and in QD thin-films that were drop-cast directly onto the working electrode.[8] Later studies switched to working electrodes consisting of a transparent conducting oxide electrode (such as FTO or ITO) with a 3-mercaptopropyl trimethoxysilane treated surface to facilitate binding of the nanocrystals to the electrode surface and included a careful cross-linking procedure to minimize the presence of oxidants in the film and improve conductivity.[19–21,23,25]

Under anaerobic conditions, tuning the applied potential of the working electrode allows careful control of the reducing potential of the injected charge carriers. As was mentioned previously, quantum confinement size effects will change the energy of the CB and VB levels and thereby the reduction potential of the QDs. Consequently, larger dots charge at lower applied potentials than smaller dots.[8,12] Capping ligands can also affect the reduction potential with as much as a 300 meV difference between CdSe QDs capped with octanethiol and those capped with TOPO.[12]

Correlation of cyclic voltammetry measurements and optical bleach changes can be used to quantify charge injection into the QDs and demonstrate the sequential filling of the $1S_e$ and $1P_e$ CB

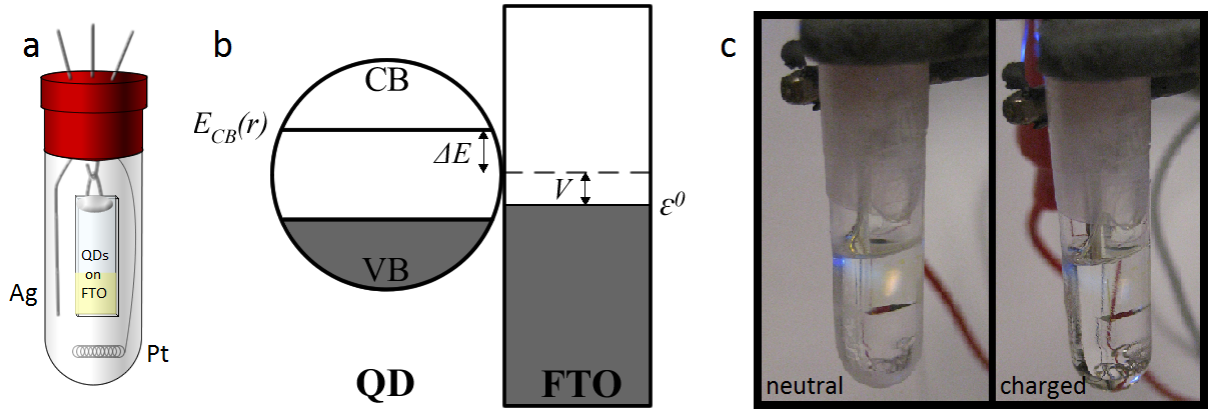

Figure 1.4: The spectroelectrochemical cell. **(a)** Schematic diagram of the spectroelectrochemical cell. **(b)** Energy diagram showing how applied potential (V) is adjusted with respect to the conduction band energy (E_{CB}) to allow charge injection into the QD film. **(c)** Photos of the spectroelectrochemical cell used in Chapter 2 while under photoexcitation with a 405 nm laser pointer. The Mn^{2+} : CdS QD film exhibits characteristic orange-yellow Mn^{2+} PL when neutral, and the PL is quenched upon charge injection.

levels.[5,19,20,23,26] The electrochemical method can also be used to reversibly inject h^+_{VB} into QDs, but has only been successful in PbSe due to the instability of long-lived h^+_{VB} in CdS,[26] CdSe,[27] CdTe,[28] and PbS[29] which often leads to QD degradation and non-reversible PL quenching.

1.3 Charge Trapping

One of the predominant differences between self-assembled and colloidal QDs is the nature of the surface. Colloidal QDs are highly susceptible to defects due to continuous restructuring of the ligand shell that passivates the QD surface.[3,30–32] Defects in turn become efficient electron or hole traps (see Figure 1.5) and lead to a significant decrease in the luminescence quantum yield as the trapped carriers provide fast nonradiative pathways for electron-hole recombination.[33] Fortunately, advanced surface passivation techniques can be used to eliminate some of these defects (such as annealing with more stable ligands or growth of a wider bandgap shell), but these methods involve more time and processing while rarely eliminating traps completely.[31,34–37]

Electron trap states lying within the semiconductor bandgap may be passivated by injected

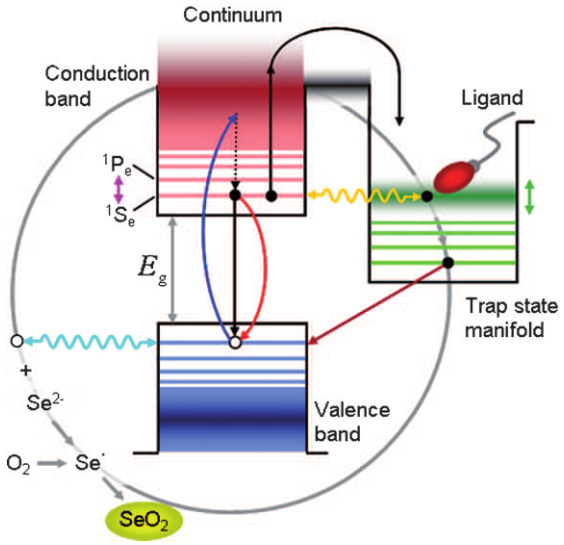

Figure 1.5: Schematic energy level diagram of the photophysical transitions in a QD. The semiconductor midgap states associated with defects and surface traps are shown with comparison to the CB and VB. Arrows indicate electronic transitions: absorption (blue), internal conversion (dotted black), radiative excitonic emission (red), Auger ionization through recombination of an exciton and charge ejection or trapping of the hot electron (solid black), electron transfer to trap states via tunnelling (yellow). Hole migration to a single surface state (light blue), and deep trap recombination (maroon). Trap-mediated recombination is predominantly nonradiative but can also lead to radiative emission.[38] Hole trapping at unpassivated "dangling" bonds of Se on the surface leads to radical anion formation which can be oxidized in the presence of O_2 to form SeO_2 (lime). Adapted from Ref. 39.

electrons in the electrochemical experiments mentioned above, but in these experiments, the trion Auger process appears to dominate the PL spectral changes. It is possible to enhance the QY of wide bandgap QDs (such as ZnSe) by targeting low-lying trap states with lower applied potentials thereby eliminating exciton-trap nonradiative pathways (see Chapter 4). Voltammetric analysis shows that negative charges injected into surface states lead to a shift in the reduction potential of the QD due to the coulombic interactions between the trapped electrons and e^-_{CB}.[18]

1.3.1 Blinking

Single particle PL measurements revealed a fluorescence intermittency phenomenon where photoluminescence of the QD fluctuates between "on" and "off" states (Figure 1.6a).[40] The proposed mechanism for fluorescence intermittency (or blinking) suggested that when more than one exci-

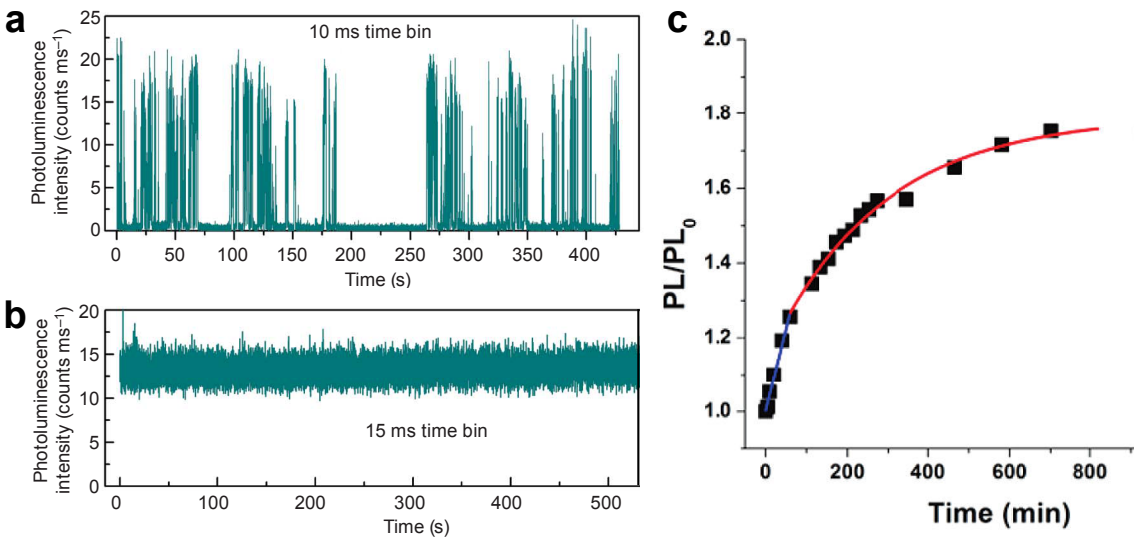

Figure 1.6: Blinking and brightening in QDs. Time dependent photoluminescence intensity traces from **(a)** a single CdSe/ZnS nanocrystal that exhibits characteristic blinking and **(b)** a single alloyed core/shell CdZnSe/ZnSe nanocrystal that displays continous photoluminescence with no fluctuations between the "on" and "off" states. **(c)** Plot of PL/PL$_0$ for a continuously photoexcited thin film of CdSe QDs that photobrightens to almost double the initial QY. Adapted from Ref. 43 and 44.

ton is present in the QD, the energy released by the annhilation of one exciton can be transferred to the e^-_{CB} (or h^+_{VB}) of another exciton and eventually lead to ejection of the charge carrier into the surrounding matrix or to a surface trap defect *via* Auger recombination (see Figure 1.5). This results in a charged QD due to the remaining resident h^+_{VB} (e^-_{CB}). Further photogenerated excitons undergo trion Auger recombination with the resident h^+_{VB} (e^-_{CB}) until the ejected charge carrier returns to neutralize the QD.[40] Temperature dependent and excitation intensity studies on single QDs revealed that a single exciton can result in a photoionized "dark" QD simply by trapping of a charge carrier.[41,42] Surface traps not only lead to decreased quantum yield of the emissive "on" state, but they also contribute towards initiation and duration of the "off" state.

Passivation of the surface by growing a "giant" shell (>14 monolayers or >5 nm thick) on CdSe cores can eliminate blinking of a single QD over a long time scale (Figure 1.6b).[45–47] Electrochemical passivation of surface traps has also been shown to reduce blinking and revealed two types of blinking.[48] "A-type" blinking occurs via the conventional mechanism mentioned above

whereby the QD is charged and discharged. "B-type" blinking occurs due to the role of surface states that are able to capture "hot" electrons before they relax to the emitting core states.[48] When surface states are passivated by electrochemical charge injection, "B-type" blinking is eliminated.

1.3.2 Photobrightening

Photobrightening (PB), the gradual photoenhancement of QD PL under photoexcitation (Figure 1.6c), has been studied extensively in both core and core-shell CdSe, as well as CdS, PbS, and PbSe QDs.[44,49–62] PB occurs when nonradiative trapping of excitonic charge carriers is inhibited[50] through any one of a number of mechanisms including photoinduced annealing,[50,63,64] photooxidation and photoreduction,[56] surface ligand chemical reactions,[51] photoinduced adsorption of molecules to passivate trap sites,[49,65–67] and photoelectrification.[54,55,59] Using an electrochemical method to introduce charge carriers into a film of QDs allows precise control over charge injection into surface traps and produces enhanced PL QY similar to photobrightening (see Chapter 4). Similarly, redox brightening of QDs is observed upon exposure to a chemical reducing agent (see Chapter 5).

1.4 Impurity Dopants

The introduction of "donor" and "acceptor" impurities in bulk semiconductors will alter the number of charge carriers by adding an electron (*n*-type) or hole (*p*-type), respectively. While there are many studies on the introduction of excess charge carriers by aliovalent doping (where the dopant has a different oxidation state than the atom it is replacing) in oxide QDs[68] there has been little success in chalcogenide QDs. Instead, typical impurity dopants are chosen based on their ability to interact with the exciton. Luminescence activators, such as Mn^{2+} and Eu^{2+}, behave like traps by providing new nonradiative relaxation pathways that lead to sensitized impurity luminescence; they are attractive dopants for electroluminescence (EL) applications. Sensitized impurity lumi-

nescence is activated by energy transfer to the dopant from the QD excited state. Additionally, the fast energy transfer from the exciton to the luminescent center competes with other nonradiative processes in the QD, improving the QY. Some of these dopants are also paramagnetic and introduce a localized spin into the QD yielding complementary physical properties; these diluted magnetic semiconductors (DMSs) have been of particular interest for their use in spin-based electronics (or spintronics).

1.4.1 Manganese(II) in II-VI QDs

Mn^{2+} is an example of a dopant that behaves as a luminescent activator. Depending on the host lattice, the lowest excited state may be the Mn^{2+} excited states ($^4T_1$) or the excitonic excited states; the relative position of these excited states determines the physical properties. In dilute Mn^{2+}-doped chalcogenide II-VI semiconductor QDs where the Mn^{2+} excited state lies within the bandgap (Figure 1.7a), excitonic absorption leads to fast energy transfer to the dopant (k_{ET}), quenching excitonic PL and yielding efficient, sensitized Mn^{2+} PL through the spin-forbidden $^4T_1 \rightarrow {}^6A_1$ ligand field transition (Figure 1.7b).[69] Quantum size effects allow tuning of the difference in energy between the Mn^{2+} excited states and the excitonic excited states. In cases where this energy difference is small, temperature-dependent dual emission is observed from both excited states as thermally assisted energy transfer from the Mn^{2+} excited state *back* to the excitonic excited states occurs due to the long Mn^{2+} excited state lifetime .[70]

Mn^{2+}-doped QDs also exhibit *sp-d* exchange interactions between the Mn *d*-electrons and charge carriers in the semiconductor host lattice leading to the "giant Zeeman effect"[72]. Despite the potential for interesting interplay between free charge carriers and magnetic dopants in QDs very few studies have focused on these types of systems. One such study looked at the effect of photochemical reduction on the absorption of Mn^{2+} : ZnO and Co^{2+} : ZnO.[14] The characteristic absorbance bleach of the first excitonic transition and appearance of the IR intra-band transition were shown to be consistent with that of undoped ZnO.

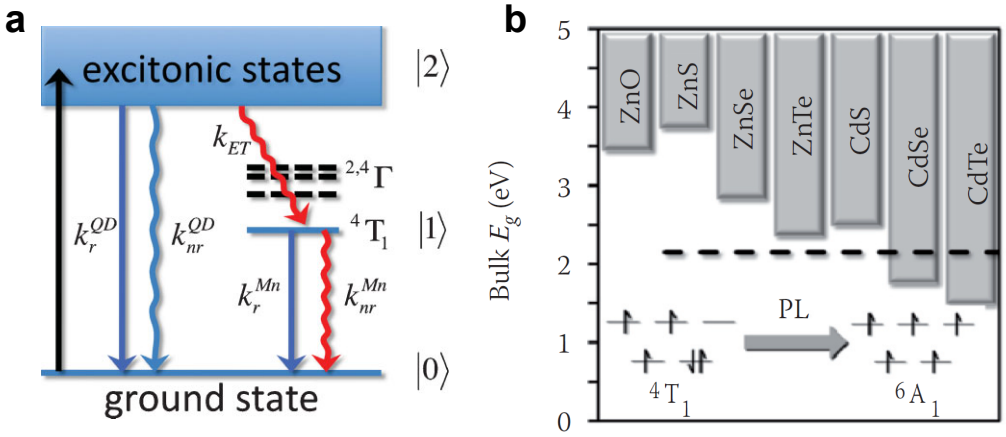

Figure 1.7: Mn^{2+}-doped QD electronic structure. **(a)** Schematic illustration of kinetic pathways of the semiconductor (k^{QD}) and dopant (k^{Mn}) in a Mn^{2+}-doped QD. Straight arrows represent radiative processes (k_r) and curved arrows represent nonradiative processes (k_{nr}). **(b)** The energy of the Mn^{2+} $^4T_1$ excited state is shown with respect to band gap energies of typical II-VI semiconductors. The electronic configurations for the $^4T_1 \rightarrow {}^6A_1$ ligand field transition are shown at the bottom. Adapted from Ref. 71 and 69.

Another study explored the magnetic properties of photochemically charged Mn^{2+} : ZnO and showed that the ferromagnetic *s-d* exchange interaction of the e^-_{CB} with Mn^{2+} was strong enough to break the antiferromagnetic exchange interaction between Mn^{2+}-Mn^{2+} dimers in a magnetic field.[73] Additionally, it has been shown that an exciton in Mn^{2+}:CdSe is capable of forming an excitonic magnetic polaron due to the even stronger *p-d* exchange interaction between Mn^{2+} and h^+_{VB} with generated effective internal magnetic fields on the order of 100 T.[74]

1.5 Conclusions

The following chapters present results focused on understanding more about the methods of charge injection and how free carriers affect the physical properties in undoped and doped QDs. In Chapter 2, electrochemical methods are used to study the Auger quenching of Mn^{2+} PL in Mn^{2+}-doped CdS thin films. Chapter 3 focuses on the discovery and characterization of a photochemical electronic doping method for colloidal CdSe nanocrystals and its extension to other chalcogenide systems. In Chapter 4, the effect of electron trap passivation in undoped ZnSe and Mn^{2+}-doped ZnSe

thin-films *via* electrochemical charge injection is shown to dramatically enhance the photoluminescence quantum yield in both systems. Finally, in Chapter 5 the electrobrightening described in Chapter 4 is adapted to colloidal suspensions through the use of chemical reductants. As a whole, these studies provide further understanding of the physical properties of undoped and Mn^{2+}-doped QDs that may prove useful in the development of future QD-based technologies.

1.6 Notes to Chapter 1

[1] Brus, L. *J. Phys. Chem.* **1986**, *90*, 2555–2560.

[2] Murphy, C. J.; Coffer, J. L. *Appl. Spectrosc.* **2002**, *56*, 16A–27A.

[3] Alivisatos, A. P. *Science* **1996**, *271*, 933–937.

[4] Shim, M.; Guyot-Sionnest, P. *Nature* **2000**, *407*, 981–983.

[5] Wehrenberg, B. L.; Guyot-Sionnest, P. *J. Am. Chem. Soc.* **2003**, *125*, 7806–7807.

[6] Shim, M.; Wang, C.; Guyot-Sionnest, P. *J. Phys. Chem. B* **2001**, *105*, 2369–2373.

[7] Shim, M.; Wang, C.; Norris, D. J.; Guyot-Sionnest, P. *MRS Bull.* **2001**, *26*, 1005–1008.

[8] Wang, C.; Shim, M.; Guyot-Sionnest, P. *Appl. Phys. Lett.* **2002**, *80*, 4–6.

[9] Guyot-Sionnest, P.; Hines, M. A. *Appl. Phys. Lett.* **1998**, *72*, 686–688.

[10] Jha, P. P.; Guyot-Sionnest, P. *ACS Nano* **2009**, *3*, 1011–1015.

[11] Leising, G. *Adv. Mater.* **1993**, *5*, 67–67.

[12] Wang, C.; Shim, M.; Guyot-Sionnest, P. *Science* **2001**, *291*, 2390–2392.

[13] Haase, M.; Weller, H.; Henglein, A. *J. Phys. Chem.* **1988**, *92*, 482–487.

[14] Liu, W. K.; Whitaker, K. M.; Kittilstved, K. R.; Gamelin, D. R. *J. Am. Chem. Soc.* **2006**, *128*, 3910–3911.

[15] Liu, W. K.; Whitaker, K. M.; Smith, A. L.; Kittilstved, K. R.; Robinson, B. H.; Gamelin, D. R. *Phys. Rev. Lett.* **2007**, *98*, 186804.

[16] Haase, M.; Weller, H.; Henglein, A. *J. Phys. Chem.* **1988**, *92*, 482–487.

[17] Schimpf, A. M.; Gunthardt, C. E.; Rinehart, J. D.; Mayer, J. M.; Gamelin, D. R. *J. Am. Chem. Soc.* **2013**, *135*, 16569–16577.

[18] Houtepen, A. J.; Vanmaekelbergh, D. *J. Phys. Chem. B* **2005**, *109*, 19634–19642.

[19] Guyot-Sionnest, P.; Wang, C. *J. Phys. Chem. B* **2003**, *107*, 7355–7359.

[20] Yu, D.; Wang, C.; Guyot-Sionnest, P. *Science* **2003**, *300*, 1277–1280.

[21] Wang, W.; Lee, T.; Reed, M. A. *J. Phys. Chem. B* **2004**, *108*, 18398–18407.

[22] Yu, D.; Wehrenberg, B. L.; Jha, P.; Ma, J.; Guyot-Sionnest, P. *J. Appl. Phys.* **2006**, *99*, 104315.

[23] Jha, P. P.; Guyot-Sionnest, P. *J. Phys. Chem. C* **2007**, *111*, 15440–15445.

[24] Guyot-Sionnest, P. *Microchim. Acta* **2008**, *160*, 309–314.

[25] Jha, P. P.; Guyot-Sionnest, P. *J. Phys. Chem. C* **2010**, *114*, 21138–21141.

[26] Haram, S. K.; Quinn, B. M.; Bard, A. J. *J. Am. Chem. Soc.* **2001**, *123*, 8860–8861.

[27] Gooding, A. K.; Gomez, D. E.; Mulvaney, P. *ACS Nano* **2008**, *2*, 669–676.

[28] Jin, L.; Shang, L.; Zhai, J.; Li, J.; Dong, S. *J. Phys. Chem. C* **2010**, *114*, 803–807.

[29] Chen, S.; Truax, L. A.; Sommers, J. M. *Chem. Mater.* **2000**, *12*, 3864–3870.

[30] Kilina, S.; Ivanov, S.; Tretiak, S. *J. Am. Chem. Soc.* **2009**, *131*, 7717–7726.

[31] Bryant, G. W.; Jaskolski, W. *J. Phys. Chem. B* **2005**, *109*, 19650–19656.

[32] Morris-Cohen, A. J.; Malicki, M.; Peterson, M. D.; Slavin, J. W. J.; Weiss, E. A. *Chem. Mater.* **2012**,

[33] Denzler, D.; Olschewski, M.; Sattler, K. *J. Appl. Phys.* **1998**, *84*, 2841–2845.

[34] Matylitsky, V. V.; Shavel, A.; Gaponik, N.; Eychmuller, A.; Wachtveitl, J. *J. Phys. Chem. C* **2008**, *112*, 2703–2710.

[35] Hines, M. A.; Guyot-Sionnest, P. *J. Phys. Chem.* **1996**, *100*, 468–471.

[36] Li, J. J.; Wang, Y. A.; Guo, W.; Keay, J. C.; Mishima, T. D.; Johnson, M. B.; Peng, X. *J. Am. Chem. Soc.* **2003**, *125*, 12567–12575.

[37] Reiss, P.; ProtiÃšre, M.; Li, L. *Small* **2009**, *5*, 154–168.

[38] Kuno, M.; Lee, J. K.; Dabbousi, B. O.; Mikulec, F. V.; Bawendi, M. G. *J. Chem. Phys.* **1997**, *106*, 9869–9882.

[39] Lee, D., Steven F.; Osborne, D., Mark A. *ChemPhysChem* **2009**, *10*, 2174–2191.

[40] Nirmal, M.; Dabbousi, B. O.; Bawendi, M. G.; Macklin, J. J.; Trautman, J. K.; Harris, T. D.; Brus, L. E. *Nature* **1996**, *383*, 802 – 804.

[41] Banin, U.; Bruchez, M.; Alivisatos, A. P.; Ha, T.; Weiss, S.; Chemla, D. S. *J. Chem. Phys* **1999**, *110*, 1195–1201.

[42] Kuno, M.; Fromm, D. P.; Hamann, H. F.; Gallagher, A.; Nesbitt, D. J. *J. Chem. Phys* **2001**, *115*, 1028–1040.

[43] Wang, X.; Ren, X.; Kahen, K.; Hahn, M. A.; Rajeswaran, M.; Maccagnano-Zacher, S.; Silcox, J.; Cragg, G. E.; Efros, A. L.; Krauss, T. D. *Nature* **2009**, *459*, 686.

[44] Tice, D. B.; Frederick, M. T.; Chang, R. P. H.; Weiss, E. A. *J. Phys. Chem. C* **2011**, *115*, 3654–3662.

[45] Chen, Y.; Vela, J.; Htoon, H.; Casson, J. L.; Werder, D. J.; Bussian, D. A.; Klimov, V. I.; Hollingsworth, J. A. *J. Am. Chem. Soc.* **2008**, *130*, 5026–5027.

[46] Mahler, B.; Spinicelli, P.; Buil, S.; Quelin, X.; Hermier, J.-P.; Dubertret, B. *Nat. Mater.* **2008**, *7*, 659–664.

[47] Vela, J.; Htoon, H.; Chen, Y.; Park, Y. S.; Ghosh, Y.; Goodwin, P. M.; Werner, J. H.; Wells, N. P.; Casson, J. L.; Hollingsworth, J. A. *J. Biophotonics* **2010**, *3*, 706–17.

[48] Galland, C.; Ghosh, Y.; Steinbeck, A.; Sykora, M.; Hollingsworth, J. A.; Klimov, V. I.; Htoon, H. *Nature* **2011**, *479*, 203–207.

[49] Cordero, S. R.; Carson, P. J.; Estabrook, R. A.; Strouse, G. F.; Buratto, S. K. *J. Phys. Chem. B* **2000**, *104*, 12137–12142.

[50] Jones, M.; Nedeljkovic, J.; Ellingson, R. J.; Nozik, A. J.; Rumbles, G. *J. Phys. Chem. B* **2003**, *107*, 11346–11352.

[51] Asami, H.; Abe, Y.; Ohtsu, T.; Kamiya, I.; Hara, M. *J. Phys. Chem. B* **2003**, *107*, 12566–12568.

[52] Myung, N.; Bae, Y.; Bard, A. J. *Nano Lett.* **2003**, *3*, 747–749.

[53] Maenosono, S. *Chem. Phys. Lett.* **2003**, *376*, 666–670.

[54] Kimura, J.; Uematsu, T.; Maenosono, S.; Yamaguchi, Y. *J. Phys. Chem. B* **2004**, *108*, 13258–13264.

[55] Uematsu, T.; Kimura, J.; Yamaguchi, Y. *Nanotechnology* **2004**, *15*, 822.

[56] Wang, Y.; Tang, Z.; Correa-Duarte, M. A.; Pastoriza-Santos, I.; Giersig, M.; Kotov, N. A.; Liz-Marzan, L. M. *J. Phys. Chem. B* **2004**, *108*, 15461–15469.

[57] Nazzal, A. Y.; Wang, X.; Qu, L.; Yu, W.; Wang, Y.; Peng, X.; Xiao, M. *J. Phys. Chem. B* **2004**, *108*, 5507–5515.

[58] Zhelev, Z.; Jose, R.; Nagase, T.; Ohba, H.; Bakalova, R.; Ishikawa, M.; Baba, Y. *J. Photochem. Photobiol., B* **2004**, *75*, 99–105.

[59] Uematsu, T.; Maenosono, S.; Yamaguchi, Y. *J. Phys. Chem. B* **2005**, *109*, 8613–8618.

[60] Peterson, J. J.; Krauss, T. D. *Phys. Chem. Chem. Phys.* **2006**, *8*, 3851–3856.

[61] Oda, M.; Hasegawa, A.; Iwami, N.; Nishiura, K.; Ando, N.; Nishiyama, A.; Horiuchi, H.; Tani, T. *J. Lumin.* **2007**, *127*, 198–203.

[62] Duncan, T. V.; Polanco, M. A. M.; Kim, Y.; Park, S.-J. *J. Phys. Chem. C* **2009**, *113*, 7561–7566.

[63] Hess, B. C.; Okhrimenko, I. G.; Davis, R. C.; Stevens, B. C.; Schulzke, Q. A.; Wright, K. C.; Bass, C. D.; Evans, C. D.; Summers, S. L. *Phys. Rev. Lett.* **2001**, *86*, 3132.

[64] Manna, L.; Scher, E. C.; Li, L.-S.; Alivisatos, A. P. *J. Am. Chem. Soc.* **2002**, *124*, 7136–7145.

[65] Oda, M.; Hasegawa, A.; Iwami, N.; Nishiura, K.; Ando, N.; Nishiyama, A.; Horiuchi, H.; Tani, T. *Colloids Surf., B* **2007**, *56*, 241–245.

[66] Oda, M.; Tsukamoto, J.; Hasegawa, A.; Iwami, N.; Nishiura, K.; Hagiwara, I.; Ando, N.; Horiuchi, H.; Tani, T. *J. Lumin.* **2007**, *122-123*, 762–765.

[67] Simurda, M.; Nemec, P.; Trojnek, F.; Mal, P. *Thin Solid Films* **2004**, *453-454*, 300–303.

[68] Schimpf, A. M.; Ochsenbein, S. T.; Buonsanti, R.; Milliron, D. J.; Gamelin, D. R. *Chem. Commun.* **2012**, *48*, 9352–9354.

[69] Beaulac, R.; Ochsenbein, S. T.; Gamelin, D. R. In *Nanocrystal Quantum Dots*, 2nd ed.; Klimov, V. I., Ed.; Taylor & Francis: London, 2010.

[70] Vlaskin, V. A.; Janssen, N.; van Rijssel, J.; Beaulac, R.; Gamelin, D. R. *Nano Lett.* **2010**, *10*, 3670–3674.

[71] Beaulac, R.; Archer, P. I.; Ochsenbein, S. T.; Gamelin, D. R. *Adv. Funct. Mater.* **2008**, *18*, 3873–3891.

[72] Furdyna, J. K. *J. Appl. Phys.* **1988**, *64*, R29–R64.

[73] Ochsenbein, S. T.; Feng, Y.; Whitaker, K. M.; Badaeva, E.; Liu, W. K.; Li, X.; Gamelin, D. R. *Nat. Nanotechnol.* **2009**, *4*, 681–687.

[74] Beaulac, R.; Schneider, L.; Archer, P. I.; Bacher, G.; Gamelin, D. R. *Science* **2009**, *325*, 973–976.

Chapter 2

Electrochemically Controlled Auger Quenching of Mn^{2+} Photoluminescence in Doped Semiconductor Nanocrystals

Auger processes in colloidal semiconductor nanocrystals have been scrutinized extensively in recent years. Whether involving electron–exciton, hole–exciton, or exciton–exciton interactions, such Auger processes are generally fast and hence have been considered prominent candidates for interpreting fast processes relevant to photoluminescence blinking and multiexciton decay. With recent advances in the chemistries of nanocrystal doping, increasing attention is now being paid to analogous photophysical properties of colloidal-doped semiconductor nanocrystals. Here, we report the first investigation of the effects of electron-dopant exchange interactions on dopant luminescence in doped semiconductor nanocrystals. Using electrochemical techniques, electrical control of charge-carrier densities in films of colloidal Mn^{2+}-doped CdS quantum dots has been achieved and used to demonstrate remarkably effective Auger de-excitation of photoexcited Mn^{2+}. The doped nanocrystals are found to be substantially more sensitive to Auger de-excitation than their undoped analogues, a result shown to arise primarily from the long Mn^{2+} excited-state lifetime. This observation of exceptionally effective Auger quenching has broader implications in

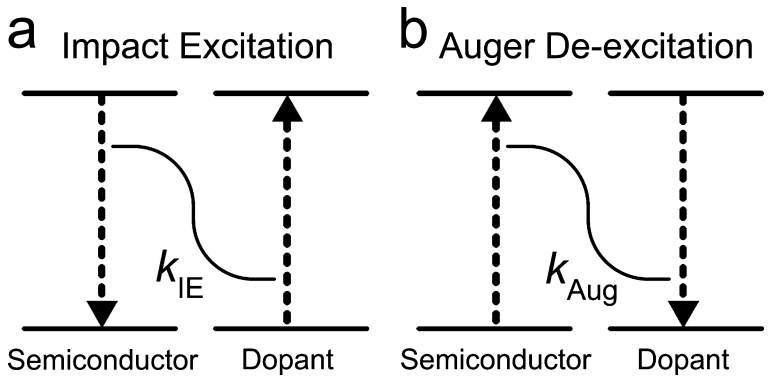

Figure 2.1: Impact excitation and Auger de-excitation processes. **(a)** Impact excitation of a dopant ion in a semiconductor involves nonradiative energy transfer from a highly energetic carrier to the dopant, yielding a relaxed carrier and the dopant in an electronic excited state. **(b)** Auger de-excitation of an excited dopant in a semiconductor involves nonradiative energy transfer from the dopant to a band carrier, yielding a relaxed dopant and a highly excited carrier. k_{IE} and k_{Aug} are the rate constants associated with impact excitation and Auger de-excitation, respectively. Auger de-excitation is the microscopic reverse of impact excitation.

areas of high-power, single-particle, or electrically driven luminescence of doped semiconductor nanocrystals, and also suggests interesting opportunities for modulating Mn^{2+} photoluminescence intensities on sublifetime time scales, or for imaging charge carriers in nanocrystal-based devices. The work in this chapter is reprinted with permission from White, M. A., Weaver, A. L., Gamelin, D. R. *ACS Nano*, **2011**, *5*, 4158-4168. Copyright 2011 American Chemical Society.

2.1 Introduction

Transition-metal and rare-earth ions serve as activators in numerous electroluminescent (EL) devices based on impact excitation.[1–3] In this process, a conduction-band (CB) electron accelerated by an electric field imparts some of its excess energy to excite a dopant ion (Figure 2.1a), which may then relax radiatively back to its ground state. Impact excitation has been proposed to underpin many Mn^{2+}-doped II-VI EL devices, including recently reported Mn^{2+}-doped nanocrystal EL devices prepared by soft processing.[4–8] The microscopic reverse of impact excitation is Auger de-excitation. In this process, energy is transferred from an excited dopant to a charge carrier to

yield the ground-state dopant and an excited charge carrier (Figure 2.1b). Auger de-excitation can be a major nonradiative loss channel that ultimately limits the efficiencies of such EL devices.[9–12] Auger de-excitation also limits gain in SiO_2 optical wave guides containing both Er^{3+} ions and Si nanocrystals,[13] although Er^{3+} is not within the nanocrystals themselves.[14,15]

Advances in the chemistries of colloidal nanocrystal doping have recently provided access to entirely new forms of doped semiconductor nanostructures, and the rich physical properties displayed by such structures are now attracting broad interdisciplinary interest.[16–39] However, whereas electron-exciton and biexciton Auger de-excitation processes in undoped colloidal semiconductor nanocrystals have received tremendous attention,[40,41] partly in relation to multiexciton decay[42,43] and nanocrystal blinking,[44–48] analogous carrier-dopant and exciton-dopant Auger quenching processes in doped semiconductor nanocrystals have not yet been examined.* To the contrary, recent publications have suggested that Mn^{2+} PL is not affected by ionization of the nanocrystal host,[31] and that nonlinear PL power dependencies of doped nanocrystals can be interpreted in terms of biexciton Auger de-excitation[37] or Mn^{2+} excitation saturation[35] without consideration of Mn^{2+}-centered Auger de-excitation processes.

Here, we report the use of electrochemical techniques to control Mn^{2+} photoluminescence (PL) in Mn^{2+}:CdS quantum dot (QD) films. Introduction of CB electrons into these QDs is shown to very effectively quench Mn^{2+} PL by Auger de-excitation. Steady-state and time-resolved PL measurements performed as a function of charging allow the fundamental electron-Mn^{2+} Auger rate constant to be determined. Poor carrier mobility is concluded to limit Auger quenching at extremely low charging levels. The exceptionally high sensitivity of Mn^{2+}-doped QDs to Auger de-excitation is shown to be associated primarily with the long Mn^{2+} excited-state lifetime. These results highlight the need to consider dopant-based Auger processes explicitly when interpreting

*The ubiquitous exciton-to-dopant energy transfer process that gives rise to sensitized dopant PL is sometimes also described as an Auger process. (see for example: Chernenko, A. V.; Brichkin, A. S.; Sobolev, N. A.; Carmo, M. C. *J. Phys.-Cond. Matter.* 2010, *22*, 355306.) We refer here specifically to Auger de-excitation (*i.e.,* dopant PL quenching) processes.

excitation power dependence, blinking, and electroluminescence efficiencies from doped semiconductor nanocrystals.

2.2 Results & Discussion

2.2.1 Colloidal Mn^{2+}-Doped CdS Quantum Dots

Figure 2.2a shows 295 K absorption, PL, and PL excitation (PLE) spectra of colloidal wurtzite 0.5% Mn^{2+}:CdS nanocrystals synthesized by modification of literature methods.[26] Owing to quantum confinement, the first excitonic absorption maximum occurs at 2.8 eV, ∼0.3 eV higher than in bulk CdS, corresponding to an average QD diameter of $d_{QD} \approx 4.5$ nm.[49] This diameter and Mn^{2+} concentration yield, on average, ∼5 Mn^{2+}/QD. The PL spectrum is dominated by intense Mn^{2+} $^4T_1 \rightarrow {}^6A_1$ *d-d* luminescence centered at 2.10 eV, with a room-temperature quantum yield (QY) of 29%. The PLE spectrum collected monitoring this *d-d* PL (Figure 2.2a) confirms sensitization by the CdS host. No excitonic PL is observed, reflecting rapid energy transfer to Mn^{2+}.[36,50–52] Figure 2.2b shows a room-temperature electron paramagnetic resonance (EPR) spectrum of 0.5% Mn^{2+}:CdS QDs. The hyperfine splitting parameter $A = (65.5 \pm 0.2) \times 10^{-4}$ cm^{-1} agrees well with that of bulk Mn^{2+}:CdS (65.3×10^{-4} cm^{-1}).[53] Figure 2.2c shows 5 K 0-6 T magnetic circular dichroism (MCD) spectra of a drop-coated film of 0.5% Mn^{2+}:CdS QDs. The lowest energy excitonic transition is characterized by strong positive intensity at its leading edge that follows the $S = 5/2$ magnetization of Mn^{2+} (Figure 2.2c, inset). An excitonic Zeeman splitting energy at saturation of $\Delta E^{sat}_{Zeeman} = 13.2$ meV is estimated[16] from these data, with a low-field 5 K g value of ∼70, confirming the existence of giant excitonic Zeeman splittings dominated by Mn^{2+}-exciton *sp-d* exchange coupling.[16,54] X-ray diffraction (XRD) data (Figure 2.2d) confirm the wurtzite structure and show peak widths consistent with $d_{QD} \approx 4.5$ nm $\pm$ 0.5 nm. Overall, these data confirm successful synthesis of the target Mn^{2+}:CdS QDs, which were then used in electrochemical exper-

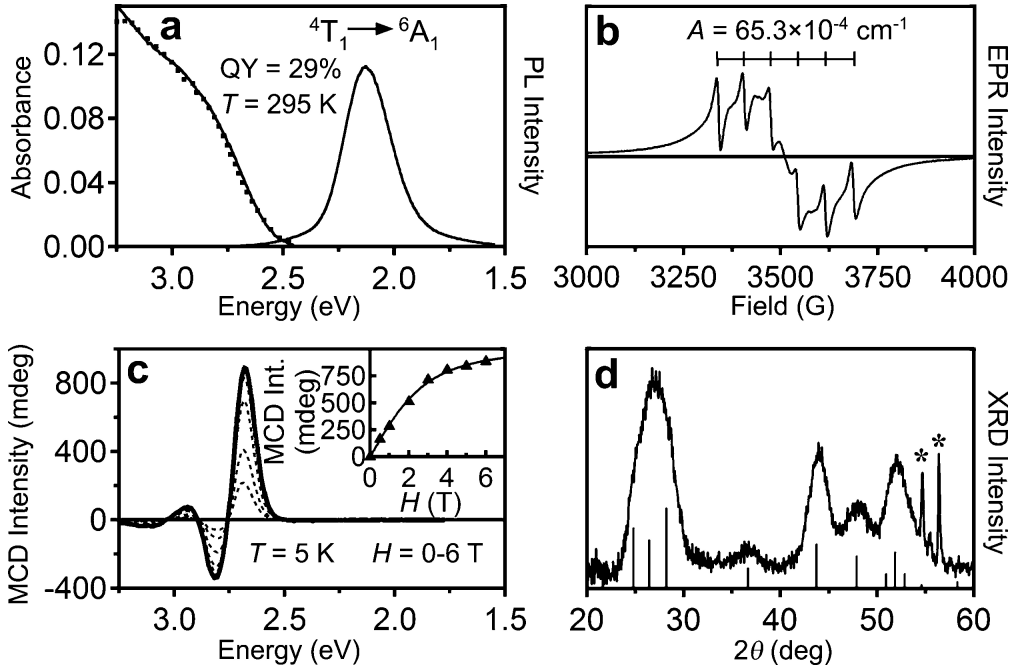

Figure 2.2: Colloidal Mn^{2+}:CdS quantum dots. **(a)** Room-temperature absorption (solid, left axis), photoluminescence (solid, right axis), and photoluminescence excitation (dashed, right axis) spectra of colloidal $d_{QD} = 4.5$ nm, 0.5% Mn^{2+}:CdS nanocrystals suspended in toluene. The PL quantum yield of the colloidal Mn^{2+}:CdS nanocrystals under nitrogen atmosphere is 29%. **(b)** Room-temperature EPR spectrum of colloidal $d_{QD} = 4.5$ nm, 0.5%Mn^{2+}:CdS QDs suspended in toluene, showing the characteristic six-line hyperfine pattern. The literature hyperfine coupling constant for Mn^{2+} in CdS is indicated.[53] **(c)** Variable field (0-6 T), 5 K MCD spectra of a drop-coated film of colloidal $d_{QD} = 4.5$ nm, 0.5% Mn^{2+}:CdS QDs. The inset shows the field dependence of the MCD intensity at 2.66 eV (▲). The solid line plots the anticipated MCD magnetization curve ($g_{Mn} = 2.0$, $S = 5/2$, and T = 5 K). **(d)** Powder XRD of $d_{QD} = 4.5$ nm, 0.5% Mn^{2+}:CdS nanocrystals. The literature powder diffraction intensities for wurtzite CdS are shown as black bars. The sharp peaks (✻) are associated with the Si substrate.

iments.

2.2.2 Electrochemical Reduction of Mn^{2+}-Doped Quantum Dots

Mn^{2+}:CdS QD films were prepared by depositing the above colloids onto 3-mercaptopropyltrimethoxysilane (MPTMS) treated $F^- : SnO_2$ (FTO) electrodes and cross-linking with 1,7-heptanediamine following literature procedures.[41,55–57] Figure 2.3a shows cyclic voltammograms (CVs) of a representative Mn^{2+}:CdS QD film (thickness $\approx$ 200 nm), measured at 210 K. A reduction wave is observed at *ca.* 1.2 V *versus* Ag^0. Similar reduction waves in undoped II-VI QDs have

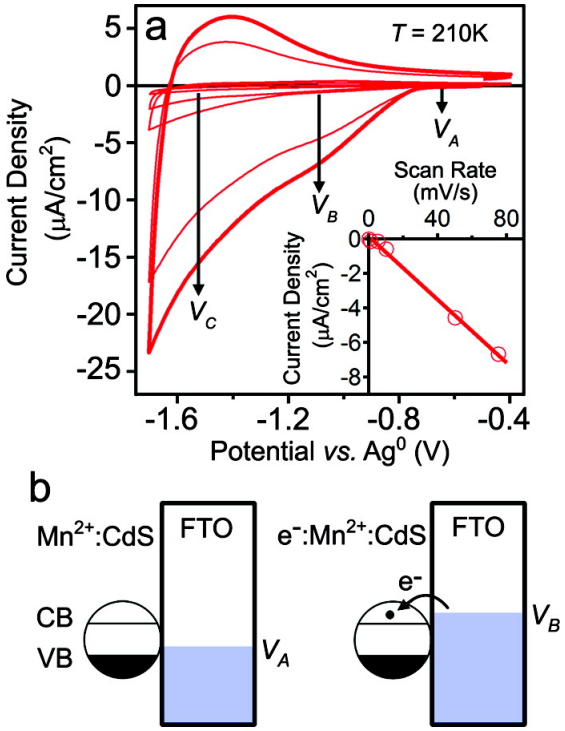

Figure 2.3: Cyclic voltammetry of a Mn^{2+}:CdS quantum dot film. **(a)** Cyclic voltammograms collected as a function of scan rate (v) for a drop-coated film of $d_{QD} = 4.5$ nm, 0.5% Mn^{2+}:CdS QDs on FTO in a 0.1 M TBAP solution in DMF at 210 K (scan rates: 1, 5, 10, 50, and 75 mV/s). Points V_A, V_B, and V_C indicate the uncharged, reduction peak maximum (partial $1S_e$ filling), and completion of the first reduction wave (complete $1S_e$ filling, onset of $1P_e$ filling), respectively, as determined by absorption spectroscopy. **(Inset)** Scan rate dependence of the peak current measured at VB. The asymmetry between forward and reverse scans is partly attributable to FTO, see Appendix A. **(b)** Scheme for charging of Mn^{2+}:CdS quantum dots. At V_A, the energy gap between the Fermi level and the $1S_e$ levels in the CdS nanocrystal film is large, so there is no electron transfer. At V_B, electrons can tunnel into the film ($N_{e^-} \approx 1\ e^-_{CB}$/QD).

been interpreted as electron injection into the $1S_e$ CB levels of the nanocrystals.[55–58]

The onset of a second reduction peak is observed at more negative potentials (Figure 2.3a) and tentatively interpreted as filling of the $1P_e$ CB levels.[57] The peak current density at the first reduction wave depends linearly on scan rate (Figure 2.3a, inset), consistent with reduction of adsorbed species.[59] Reoxidation is slow, so the observed oxidation wave is smaller than the reduction wave. This slow return is also present in control experiments with MPTMS-treated FTO substrates without QDs (see Appendix A), and therefore does not come entirely from the nanocrystals themselves. Likewise, the FTO electrodes themselves also show current flow in this potential window, which

likely contributes to the asymmetry between forward and reverse waves (see Appendix A). Similar contributions from substrates appear to be generally observed in related literature studies.[56,60]

As in other QD films,[60] the exact potential of the first reduction wave differed for different films of the same QDs, and even drifted over extended times (tens of hours), presumably reflecting surface fluctuations and the use of an Ag^0 pseudoreference. For comparison across samples, we therefore identify three special points in the CV that are common to all samples, as illustrated in Figure 2.3a. V_A denotes a potential far below any detectable charging, V_B denotes the peak potential of the first reduction wave (50% $1S_e$ filling), and V_C denotes a potential after completion of the first reduction wave (complete $1S_e$ filling, onset of $1P_e$ filling). The electrode at potentials V_A and V_B is shown schematically in Figure 2.3b.

Figure 2.4a (top) shows the film's absorption spectrum measured as a function of applied potential. Increasing from V_A to V_C causes bleaching of the excitonic absorption at $\sim$2.8 eV, which recovers fully upon reoxidation. Figure 2.4a (bottom) shows the difference absorption spectra as a function of potential ($\Delta A/A = (A(V) - A(V_A))/A$, where A is the absorbance at 2.8 eV and at V_A). The peak in $\Delta A/A$ gradually shifts to higher energy with potential, because larger particles with lower $1S_e$ energies are generally reduced at lower potentials than smaller particles.[55,60,61] As the potential approaches V_C, the maximum change in $\Delta A/A$ converges to *ca.* -0.5, the remaining absorbance being attributed to broad higher energy excitonic transitions.[60] The bleach of the lowest excitonic level is thus reported using $\Delta A/A_0$, where $A_0 = A(V_A) - A(V_C)$ at 2.8 eV; by definition, $\Delta A/A_0$ ranges from 0 to -1. As in previous studies,[56,57,60] the bleach in excitonic absorption was used to measure N_{e^-}, the average number of $1S_e$ e^-/QD. V_B is defined as the potential at which $\Delta A/A_0 = 0.5$. At V_B, $N_{e^-} = 1.0\ e^-_{CB}$/QD. Identification of V_B is thus independent of the number of QDs or the film thickness, and does not rely on detailed knowledge of the QD extinction coefficients. Identification of V_B also does not rely on CV measurements, which generally overestimate the number of conduction band electrons.[56,60] For example, using the time-integrated current of a potential sweep from V_A to V_B and the film thickness determined from its optical density,[49] an

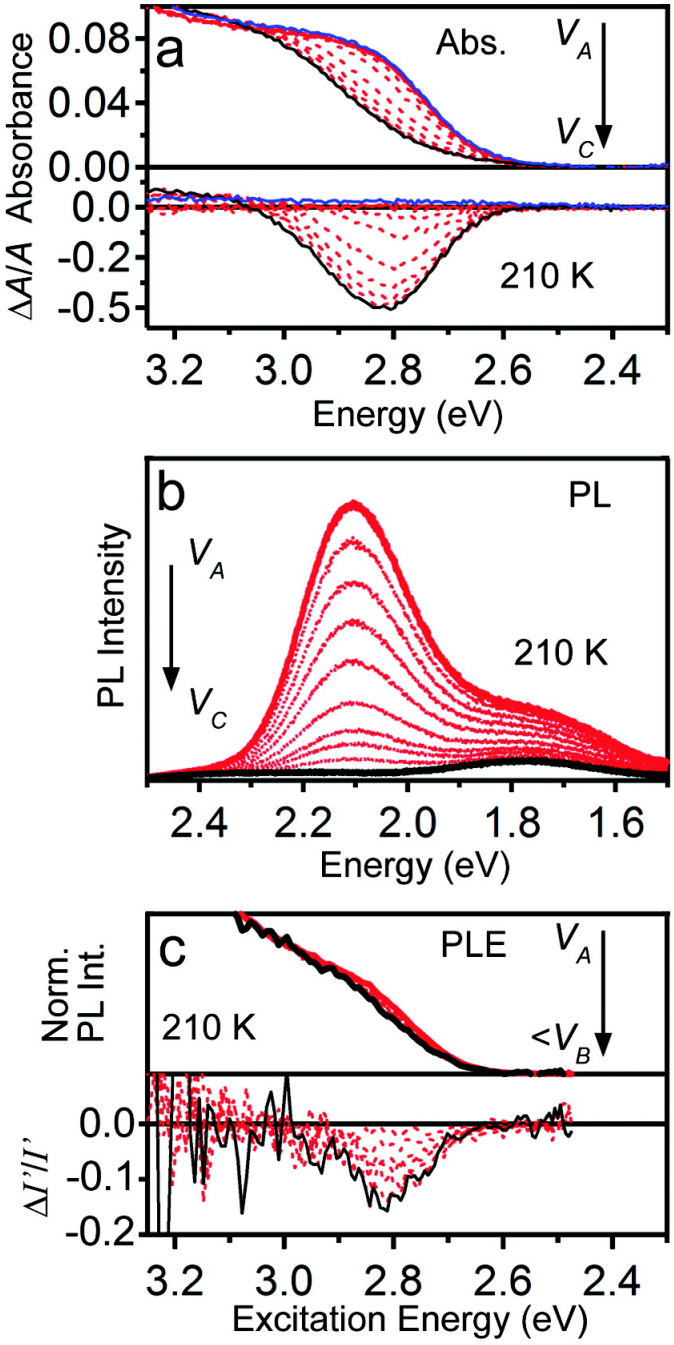

Figure 2.4: Optical response of a Mn^{2+}:CdS quantum dot film to electron injection. **(a) (Top)** 210 K absorption spectra collected at various potentials from V_A to V_C (red and black solid, respectively), and with the potential returned to V_A (blue solid). **(Bottom)** Difference absorption ($\Delta A/A$) spectra at various potentials. **(b)** 210 K PL spectra collected at various potentials from V_A to V_C (red and black solid, respectively). (c) (Top) 210 K photoluminescence excitation (PLE) spectra collected monitoring the integrated PL intensity between 2.0 and 2.5 eV, with potentials ranging from V_A (red solid) to below V_B (i.e., 1.1 V in Figure 2.5a, black). The PLE curves were normalized at 3.03 eV. **(Bottom)** Difference PLE spectra at various potentials ($\Delta I'/I'$, where prime indicates intensities from normalized PLE spectra).

average of $\sim$1.5 e^-/QD is estimated at V_B in Figure 2.3a, consistent with partial filling of the $1S_e$ level[55,57] but greater than the number indicated by the optical data.

As with the colloids, the PL of films made from these QDs (e.g., Figure 2.4b) is dominated by the Mn^{2+} $^4T_1 \rightarrow {}^6A_1$ transition, but a broad trap luminescence band is now observed, centered at $\sim$1.75 eV.[†] For the film shown in Figure 2.4b, the 295 K Mn^{2+} PL QY dropped from 29% to 6%. Similar QY losses have been reported for other nanocrystal films, for example dropping from $\sim$30% in CdSe/CdS colloids to $\sim$2% in a film.[57] The Mn^{2+} PL QY of this film was improved to 42% by lowering the temperature to 210 K, and all electrochemistry measurements were therefore performed at this temperature. With charging, the PL intensity decreases over the entire spectral range (Figure 2.4b). Interestingly, the Mn^{2+} PL intensity drops substantially faster than the trap emission with potential, suggesting that Mn^{2+} PL is more sensitive to CB electrons (*vide infra*). Both PL bands recover fully upon returning to V_A. All films showed spectroelectrochemical properties similar to those seen in Figure 2.4b.

Figure 2.4c (top) shows PLE spectra collected at different potentials. To account for the overall PL decrease with charging, the PLE intensities have been normalized at 3.05 eV, where the absorbance does not change with potential. Like the absorption, the PLE intensity at the absorption edge also bleaches upon charging. A smaller overall difference is seen by PLE only because the range of potentials that can be sampled before the PL is entirely quenched is small. Quantitatively, the exciton's PLE bleach (Figure 2.4c, bottom) agrees well with its absorption bleach (Figure 2.4a, bottom) at the same potential, for example, when $\Delta A/A_0 = 0.16$, $\Delta I'/I' = 0.16$ (where $\Delta I' = I'(V) - I'(V_A)$ and I' is the exciton's PLE intensity when the PLE spectrum is normalized at 3.05 eV).

To quantify the difference between PL quenching and absorption bleaching, absorption and PL data were collected simultaneously for another Mn^{2+}:CdS QD film during the course of a linear

[†]The relative magnitude of the trap emission appears to depend on the duration of the heating step in the QD cross-linking process, with less trap emission usually observed for shorter heating times.

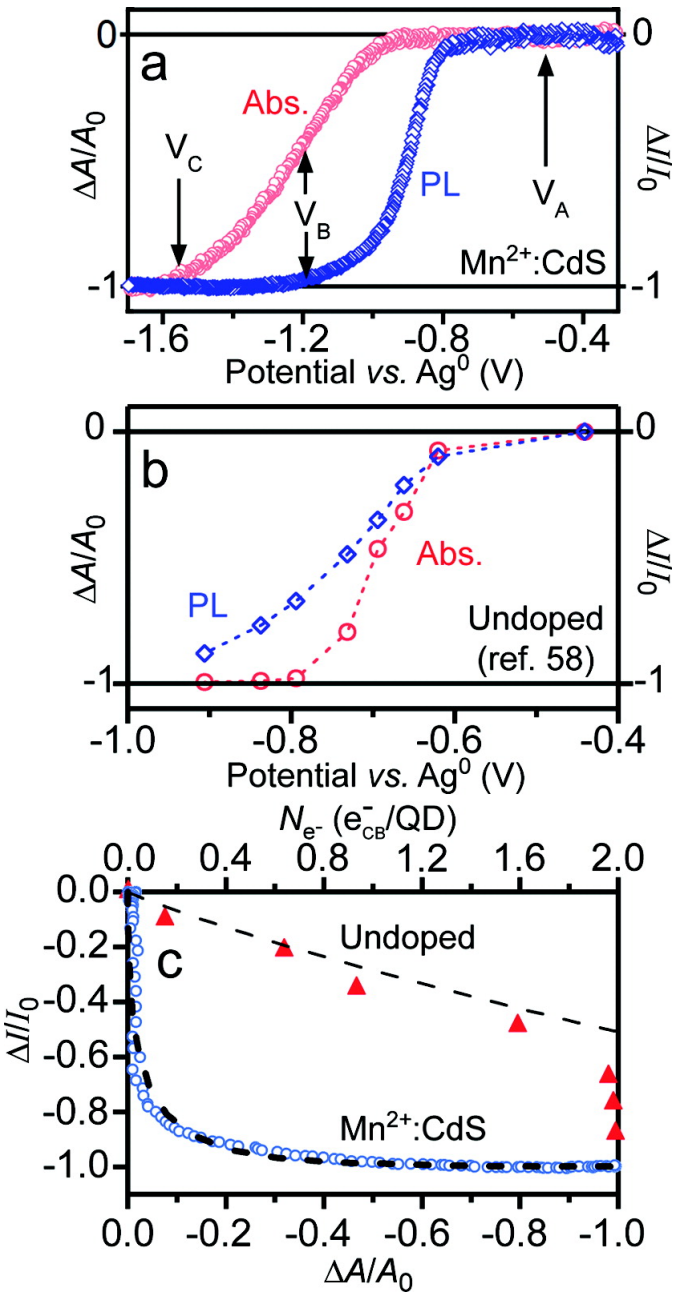

Figure 2.5: Comparison of doped and undoped QDs. **(a)** $\Delta A/A_0$ at 2.8 eV (red open circle) and $\Delta I/I_0$ integrated between 2.0 and 2.5 eV (diamond) for Mn^{2+}:CdS QDs, collected simultaneously during a linear sweep voltammogram ($v = 10$ mV/s) at 210 K. **(b)** $\Delta A/A_0$ (red open circle) and $\Delta I/I_0$ (diamond) for undoped CdSe/CdS nanocrystals collected at room temperature in a similar electrochemical configuration, adapted from ref 57. **(c)** Plots of $\Delta I/I_0$ vs $\Delta A/A_0$ for undoped CdSe/CdS (red triangle, from ref 57) and Mn^{2+}:CdS (open circle) QDs. The dashed lines in panel **c** were calculated using eq 2.5 as described in the text.

sweep voltammogram (Figure 2.5a). Importantly, the Mn^{2+} PL intensity begins to drop well before any detectable absorption bleach. Although separated by $\sim$0.32 V, the two responses are roughly parallel, with the PL curve being slightly steeper at low potentials. Mn^{2+} PL is quenched by $\sim$75% ($\Delta I/I_0 = -0.75$) when excitonic absorption is bleached by only 3% ($\Delta A/A_0 = -0.03$), and it is quenched by 98% at V_B, where excitonic absorption is bleached by only 50%. This response is strikingly different from that of undoped CdSe/CdS QDs, where excitonic PL is quenched by only $\sim$33% at V_B (Figure 2.5b).[57] This major qualitative difference between Auger quenching of doped and undoped QDs is emphasized by plotting $\Delta I/I_0$ *versus* $\Delta A/A_0$ for both in Figure 2.5c, and constitutes the central new observation of the present study.

It is conceivable that the vastly increased sensitivity of the Mn^{2+}-doped QDs to Auger quenching could be related to surface traps, but this possibility can be eliminated experimentally. Figure 2.6a shows the voltage dependence of the PL spectrum of a Mn^{2+}:CdS QD film prepared by heating the nanocrystal film for a shorter time after the ligand exchange, which reduces surface trap emission intensity by approximately a factor of 3 relative to the Mn^{2+} PL shown in Figure 2.4b, and by over a factor of 5 relative to the film used for the data in Figure 2.5a. With applied potential, Mn^{2+} PL quenching is again observed. The Mn^{2+} PL is fully recovered upon film reoxidation. Figure 2.6b plots $\Delta I/I_0$ and $\Delta A/A_0$ versus potential for this film as in Figure 2.5a. For easy comparison with the data from Figure 2.5a, the x axis is referenced to V_B (where $\Delta A/A_0 = 0.5$) and the data from Figure 2.5a are included on the same scale. The raw data are provided in Appendix A. Notable from Figure 2.6b is the fact that the voltage difference between absorption and PL curves is essentially identical for the two samples ($\sim$0.32 V). The absorption and PL curves are again roughly parallel, a feature predicted by the Fermi-Dirac model discussed below, and elimination of surface traps makes the PL response to applied voltage sharper and more complete at lower potentials; that is, the electrochemical quenching of Mn^{2+} PL becomes more pronounced, not less pronounced as might be anticipated were traps responsible. The sharpening of the electrochemical response when traps are eliminated is interpreted as reduced Stark-effect broadening of the distri-

bution of CB potentials. Overall, these results provide compelling experimental evidence against any pivotal role played by surface trap states in the electrochemical PL quenching of these Mn^{2+}-doped CdS nanocrystals. This conclusion is consistent with previous demonstrations that surface trapped electrons are unable to effectively quench the excitonic luminescence of undoped QDs,[57] because the probability densities of the highly localized Mn^{2+} d wave functions at the QD surfaces are even smaller than those of the excitonic wave functions.

Time-resolved PL data were also measured as a function of QD charging (Figure 2.7). The PL decay at V_A is multiexponential (Figure 2.7, inset), with a slow component comparable to that of the colloidal Mn^{2+}:CdS QDs ($\tau_{Mn} = 1.4$ ms, Appendix A). Faster contributions are also observed, attributable to nonradiative relaxation processes. The decay constant of the slow component in Figure 2.7(inset) is essentially independent of applied potential between V_A and V_B, despite the overall decrease in PL intensity by $\sim$98% over this range (Figure 2.4b). This result indicates that some Mn^{2+} ions are unaffected by partial charging of the QD film, while others are deactivated on submillisecond time scales. The main panel of Figure 2.7 shows the same time-resolved PL data over a shorter time window, now normalized at 5 ms to emphasize changes at shorter times. These data reveal a short time scale nonradiative Mn^{2+} decay channel growing in with QD charging. As shown below, these time-resolved PL results are precisely what should be expected from e^-_{CB}-Mn^{2+} Auger de-excitation.

2.2.3 Kinetic Model

The sharp contrast between the absorption and PL responses in Figures 4, 5a, and 6, and that between the PL responses of doped and undoped QDs (Figure 2.5c), both reflect the fact that absorption spectroscopy probes instantaneous charging levels, whereas PL spectroscopy is sensitive to dynamical processes. The results above were therefore analyzed using a kinetic model in which Mn^{2+} excited-state decay is described by an effective decay rate constant (k_{eff}) having contributions from both charge-independent (intrinsic) and charge-dependent (Auger) processes:[62,63]

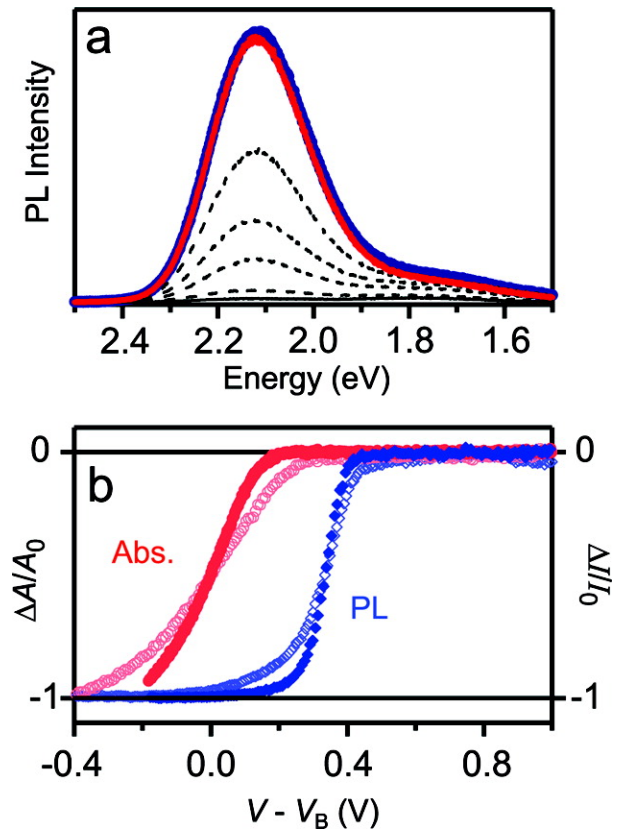

Figure 2.6: Comparison of Mn^{2+}:CdS QD films with different surface trap concentrations. **(a)** 210 K photoluminescence (PL) spectra collected at various potentials from V_A to V_C (red and black solid, respectively), for a film of Mn^{2+}:CdS QDs with minimal surface trap PL. The surface trap PL intensity is decreased by over a factor of 5 relative to the film of Figure 2.5a (and by a factor of 3 relative to Figure 2.4b). The Mn^{2+} PL is quenched with applied potential, and is recovered upon film reoxidation (blue solid). **(b)** Voltage response of $\Delta A/A_0$ at 2.8 eV (solid red circle) and $\Delta I/I_0$ integrated between 2.0 and 2.5 eV (solid blue diamond) for the Mn^{2+}:CdS QDs from panel **a**, plotted *vs* V-V_B to allow direct comparison with the data from Figure 2.5a (open red circle and open diamond). Although the shapes of the two data sets differ, the voltage difference between $\Delta A/A_0$ and $\Delta I/I_0$ curves is essentially identical ($\sim$0.32 V). Elimination of surface traps makes the electrochemical PL quenching more pronounced.

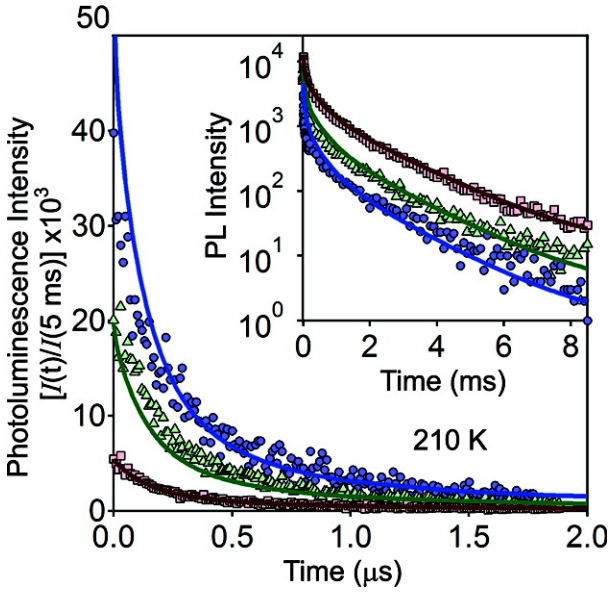

Figure 2.7: Voltage dependence of the Mn^{2+} photoluminescence decay times. 210 K photoluminescence time dependence for a Mn^{2+}:CdS QD film held at V_A (red solid square) and at two potentials more negative than V_B corresponding to 65% (green triangle) and 80% (black solid circle) bleach of the steady-state photoluminescence intensity. The curves have been normalized to the value at 5 ms to emphasize short-time dynamics. **(Inset)** Semilog plot of the same data over a broader time scale. These data have not been normalized. The similar Mn^{2+} PL intensities at $t \approx 0$ ns indicates that quenching occurs after Mn^{2+} excitation. The solid lines show photoluminescence decay curves calculated using the model described in Sec. 2.2.3 and parameters from fits of steady-state absorption and photoluminescence data (see Sec. 2.2.3).

$$k_{\text{eff}}(E_{\text{CB}},V) = k_{\text{Mn}} + k_{\text{Aug}}\rho_{\text{e}^-}(E_{\text{CB}},V) \tag{2.1}$$

Here, k_{Mn} is the Mn^{2+} $^4T_1 \rightarrow {}^6A_1$ total decay rate constant (radiative plus nonradiative) in the absence of additional electrons, and k_{Aug} is the nonradiative Auger de-excitation rate constant (approximated to be size independent over the range of diameters in this ensemble). $\rho_{\text{e}^-}(E_{\text{CB}},V)$ describes the average number of CB electrons per QD for the subset of QDs having $1S_e$ energies of E_{CB}, when the system is held at potential V. $\rho_{\text{e}^-}(E_{\text{CB}},V)$ can take values of 0-2.

The possibility that the apparent Mn^{2+} PL quenching could stem from electron-exciton (negative trion) Auger de-excitation occurring before energy transfer to Mn^{2+}, instead of from electron-Mn^{2+} Auger de-excitation occurring after energy transfer to Mn^{2+}, can be eliminated on the basis of two key observations. First, the Mn^{2+} PL intensity immediately after the excitation pulse is not reduced upon charge injection (see Figure 2.7 inset, $t \approx 0$ ns), indicating that Mn^{2+} sensitization proceeds independent of the charge state of the film within this experimental range. This observation demonstrates that PL quenching occurs *after* Mn^{2+} excitation. These dynamics are consistent with reports of exciton-to-Mn^{2+} energy transfer times that are at least 50 times faster than electron-exciton Auger de-excitation times.[36,41] Second, Mn^{2+} PL is substantially quenched even when the number of electrons per QD is small (see Figure 2.5c), that is, when the probability of photoexciting a QD that already contains an electron is small. Electron-exciton Auger de-excitation therefore cannot be responsible for the Mn^{2+} PL quenching observed here.

$\rho_{\text{e}^-}(E_{\text{CB}},V)$ can be determined experimentally by modeling the QD absorption bleach with charging.[61] In the limit of fast electron diffusion, $\rho_{\text{e}^-}(E_{\text{CB}},V)$ is governed by Fermi-Dirac statistics as described by eq 2.2, where E_{CB} is the CB potential, k_{B} is the Boltzmann constant, T is the temperature, and $g_{1S_e} = 2$ is the multiplicity of the $1S_e$ level. The energy (E_{rep}) associated with adding an electron to a QD with a charged neighbor, and with adding a second electron to a QD, is described by eq 2.3,[60] where e is the elementary charge, ε is the dielectric constant of the QD

film, ε_0 is the permittivity of vacuum, and λ accounts for electrolyte screening.[60] J_{ee} describes the average Coulomb energy associated with introducing a second electron into a QD ($J_{ee} = 0$ for $\rho_{e^-}(E_{CB}, V) \leq 1$, and > 0 for $\rho_{e^-}(E_{CB}, V) > 1$).[60,64]

$$\rho_{e^-}(E_{CB}, V) = \frac{g_{1S_e}}{1 + \exp\left(\frac{E_{CB} + E_{rep} - V}{k_B T}\right)} \tag{2.2}$$

$$E_{rep}(E_{CB}, V) = (1 - \lambda)\frac{3eN_{e^-}^{1/3}}{d_{QD}\pi\varepsilon\varepsilon_0} = (\rho(E_{CB}, V) - 1)J_{ee} \tag{2.3}$$

Within this model, $\Delta A(V)/A_0$ can be calculated using eq 2.4, where the second term accounts for inhomogeneous broadening of E_{CB} due to the finite QD size distribution and surface effects. Using $d_{QD} = 4.5$ nm and parameters similar to those found for undoped QD films ($J_{ee} = 85$ meV, λ = 0.92, and ε = 30 estimated from the solvent, ligands, and counterions[60]), eq 2.4 reproduces the experimental $\Delta A(V)/A_0$ data well for $E_0 = 1.15$ eV and σ = 0.14 eV (Figure 2.8a).

$$\frac{\Delta A(V)}{A_0} = -\int \frac{1}{2}\rho_{e^-}(E_{CB}, V) \times \frac{\exp\left(\frac{-(E_{CB} - E_0)^2}{2\sigma^2}\right)}{\sigma\sqrt{2\pi}} dE_{CB} \tag{2.4}$$

With $\rho_{e^-}(E_{CB}, V)$ defined by the absorption measurement, the steady-state PL intensity at any given electrochemical potential can now be analyzed using eq 2.1, where k_{Aug} is the only unknown parameter. For example, at the potential where the Mn^{2+} PL is quenched 50% ($\Delta I/I_0 = -0.5$), $k_{Mn} = k_{Aug}\rho_{e^-}(E_{CB}, V)$ from eq 2.1. Using $\rho_{e^-}(E_{CB}, V)$ at this potential determined from Figure 2.8a and the experimental PL time dependence at V_A, a value of $k_{Aug} \approx 0.2 \times 10^{10}$ $s^{-1}(e^-/QD)^{-1}$ is estimated. Interestingly, $\rho_{e^-}(E_{CB}, V)$ at this potential corresponds to ~25 QDs per CB electron; that is, *each CB electron must quench multiple photoexcited QDs*. For comparison with literature values, k_{Aug} is converted to units of cm^3s^{-1} (per e^-), yielding $k_{Aug} = 1.0 \times 10^{-10}$ cm^3s^{-1}. Auger rate constants of 5×10^{-10} cm^3s^{-1} and between 4×10^{-10} and 20×10^{-10} cm^3s^{-1} have been reported for bulk Mn^{2+}:ZnSe and Mn^{2+}:ZnS, respectively,[62,63] and 8×10^{-15} cm^3s^{-1} has been

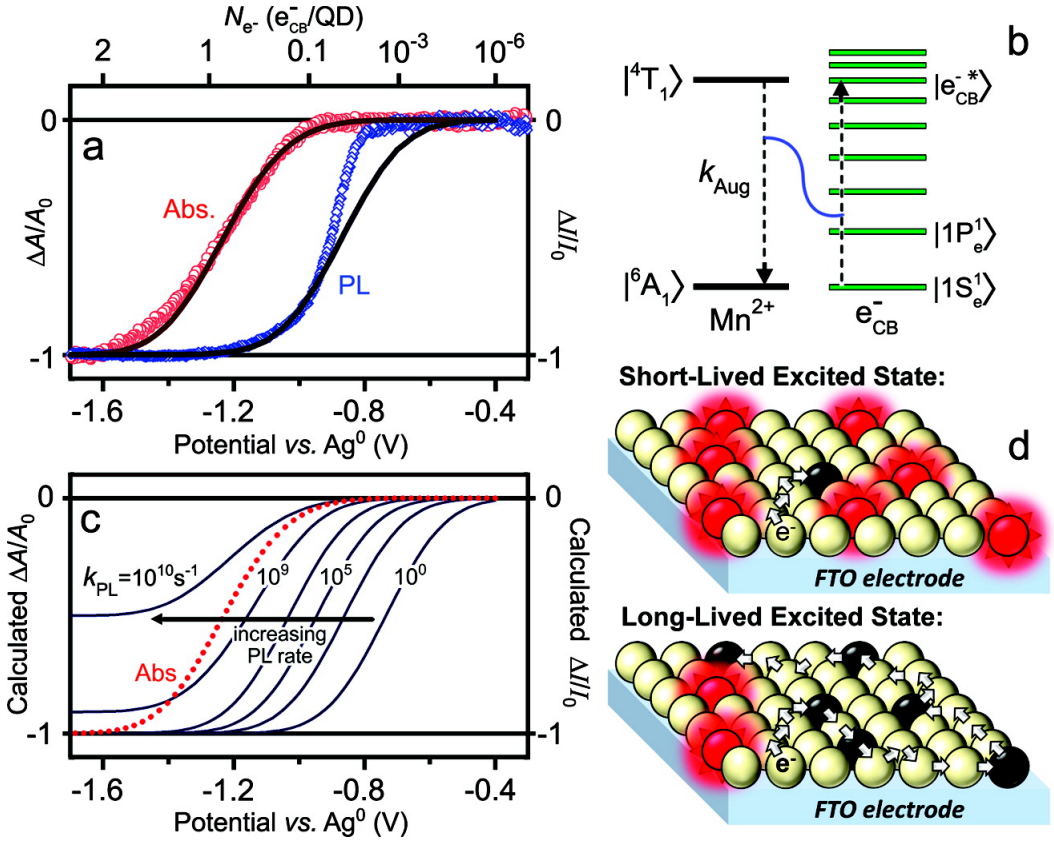

Figure 2.8: Modeling Auger de-excitation in Mn^{2+}:CdS QD films. **(a)** Experimental $\Delta A/A_0$ (red open circle) and $\Delta I/I_0$ (open diamond) as a function of applied potential, from Figure 2.4. The solid lines show calculated absorption and PL responses to nanocrystal charging as described in the text. This analysis yields $k_{\text{Aug}} = 0.25 \times 10^{10}$ $s^{-1}(e^-/\text{QD})^{-1}(2.5 \times 10^{-10}$ $cm^3s^{-1})$. See text for details. **(b)** Schematic representation of the e^-_{CB}-Mn^{2+} Auger de-excitation in Mn^{2+}:CdS QDs. Nonradiative energy transfer deactivates the Mn^{2+} $^4T_1$ state and promotes a $1S_e$ electron to a highly excited state. The process is energy conserving. **(c)** Calculated absorption ($\Delta A/A_0$, dashed red) and PL ($\Delta I/I_0$, solid blue) vs potential curves for various excited-state decay rate constants, k_{PL} (10^{10}, 10^9, 10^7, 10^5, 10^3, and 10^0 s^{-1}). Decreasing k_{PL} increases sensitivity of the film to Auger de-excitation. Undoped semiconductor nanocrystals frequently show PL decay rate constants on the order of 10^9 s^{-1}, compared to $\sim 10^3$ s^{-1} for Mn^{2+}. **(d)** Schematic illustration of the role of excited-state lifetimes in Auger de-excitation of undoped and Mn^{2+}-doped QD films. Red spheres represent photoexcited QDs, and black spheres represent those that have undergone Auger de-excitation. The arrows represent the electron's diffusion path. Because the Mn^{2+} excited-state lifetime in the doped QD film is $\sim 10^5$ times longer than the exciton lifetime in the undoped QD film, the electron can sample more of the doped QD film on the time scale of the excited-state decay, thus making Auger de-excitation more competitive with PL.

reported for bulk Mn^{2+}:CdF_2.[9] The value of k_{Aug} measured here for Mn^{2+}-doped nanocrystals thus agrees well with literature values measured for Mn^{2+}-doped bulk semiconductors. We note that these previous measurements have all used temperature to vary electron concentrations. The electrochemical approach here excels in providing fine control over electron concentrations.

The $\Delta I(\mathrm{V})/I_0$ curve of Figure 2.5a can also be simulated using eq 2.5. With a similar value for k_{Aug} (0.5×10^{10} $s^{-1}(e^-_{CB}/QD)^{-1}$, or 2.5×10^{-10} cm^3s^{-1}), eq 2.5 reproduces the experimental data well at all but the lowest electron concentrations ($\sim 10^{-8} < N_{e^-} <\sim 0.05$ e^-_{CB}/QD, Figure 2.8a), where it predicts greater quenching than observed experimentally. Below a critical value of N_{e^-}, the added electrons cannot sample the entire QD film on the time scale of the Mn^{2+} excited-state decay, despite adequate thermal energy, and the assumption underpinning eq 2.2 that electron distributions are simply dictated by Fermi-Dirac statistics breaks down. In the low-charging regime, Auger de-excitation rates (and hence PL intensities) are determined by electron mobilities. This conclusion is supported by previous reports of extremely small electron mobilities in this regime.[61,65–67]

$$\frac{I(V)}{I_0} = \int \frac{k_{Mn}}{k_{Mn} + k_{Aug}\rho_{e^-}(E_{CB},V)} \times \frac{\exp\left(\frac{-(E_{CB}-E_0)^2}{2\sigma^2}\right)}{\sigma\sqrt{2\pi}} dE_{CB} \tag{2.5}$$

As an independent test of the above analysis, the same model and fitting parameters were used to predict the PL time dependence as a function of QD charging. Equation 2.6 describes the time-dependent PL intensities as a function of V. Using fixed parameters from Figure 2.8a and the experimental PL decay curve at V_A in place of the single-exponential decay implied by eq 2.6, decay curves at other potentials were calculated and compared with experimental data in Figure 2.7. The PL quenching dynamics are reproduced remarkably well, particularly considering that these calculations involved no adjustable parameters. This excellent agreement strongly supports the above analysis.

$$I(V,t) = \int \exp\left(-\left[k_{Mn} + k_{Aug}\rho_{e^-}(E_{CB},V)\right]t\right) \times \frac{\exp\left(\frac{-(E_{CB}-E_0)^2}{2\sigma^2}\right)}{\sigma\sqrt{2\pi}} dE_{CB} \tag{2.6}$$

2.2.4 Microscopic Origins of the Highly Effective Auger De-excitation

The results presented above reveal highly effective Auger de-excitation of dopants by CB electrons in Mn^{2+}-doped semiconductor nanocrystals. Such effective Auger de-excitation of Mn^{2+} is remarkable because of the highly localized nature of the Mn^{2+} *d-d* transition involved, as it implies strong interaction between localized Mn^{2+} *d* electrons and delocalized CB electrons. It is therefore of considerable interest and importance to understand why this e^-_{CB}-Mn^{2+} Auger de-excitation is so effective.

Electron-Mn^{2+} Auger de-excitation can be described microscopically as energy transfer from an excited Mn^{2+} ion to a CB electron (Figure 2.8b), followed by relaxation of the hot electron *via* phonon emission. k_{Aug} can thus be expressed in the general form of Fermi's golden rule eq 2.7.[1,63] The initial state in eq 2.7 corresponds to the $^4T_1$ excited state of Mn^{2+} coupled to the CB electron in its $1S_e$ ground electronic state, denoted here as $|i\rangle = \left|^4T_1,1S_e^1\right\rangle$. The state formed by the Auger process involves ground-state Mn^{2+} ($^6A_1$) coupled to a highly excited conduction band electron, denoted $\langle f| = \left\langle ^6A_1,e^{-\star}_{CB}\right|$. For conservation of energy, the electron's excited state must lie ~2.1 eV above its $1S_e$ state. $r(E)$ describes the density-of-states (DOS)-weighted overlap factor.

$$k_{Aug} = \frac{2\pi}{\hbar}\left|\langle f\left|H'\right|i\rangle\right|^2 r(E) \tag{2.7}$$

As noted previously,[1] the matrix elements $\langle f\,|H'|\,i\rangle$ are similar to those describing the *s-d* exchange, which contributes, for example, to the giant excitonic Zeeman splittings observed by MCD in Figure 2.2c. Qualitatively, it can be postulated that k_{Aug} is related to *s-d* exchange as the exciton-to-Mn^{2+} energy-transfer rate constant (k_{ET}) is related to the sum of *s-d* and *p-d* exchange contributions. Values of $k_{ET} = 10^{10} - 10^{12}$ s^{-1} (per Mn^{2+}) have been measured in various doped semiconductor nanostructures.[36,50–52] Given that the *s-d* exchange is ~9 times weaker than the *p-d* exchange in bulk Mn^{2+}:CdS,[68] $k_{Aug} \approx 2.5 \times 10^{10}$ $s^{-1}(e^-/QD)^{-1}$ is a reasonable order of magnitude for a process mediated by *s-d* exchange.

The dominant orbital interaction behind this *s-d* exchange is hybridization between the CB-edge and empty Mn^{2+}(4s) orbitals.[69] The location of the participating Mn^{2+}(4s) orbital only ~2.4 eV above the bulk CdS CB edge[69] is conducive to Mn^{2+}(4s)-CB hybridization throughout the CB width. A DOS valley (X point) also resides ~2 eV above the CB edge in bulk CdS, providing ample energy conserving pathways for Auger de-excitation of Mn^{2+} to form $e_{CB}^{-\star}$,[1,70] even though such $e_{CB}^{-\star}$ states aren't observed spectroscopically at 2.1 eV above the $1S_e$ ground state (because of small oscillator strengths). The large Auger de-excitation rate constant in Mn^{2+}-doped CdS QDs is thus understood in terms of substantial Mn^{2+}(4s)-CB hybridization (large $\langle f\,|H'|\,i\rangle$) and a large density of e_{CB}^{-} excited states ~2.1 eV above the $1S_e$ state (large $r(E)$).

The large k_{Aug} alone cannot explain the significantly greater sensitivity of Mn^{2+} PL to Auger de-excitation than seen for excitonic PL in undoped QDs (Figure 2.5c), however. The e_{CB}^{-}-Mn^{2+} Auger rate constant found here (2.5×10^{-10} cm^3s^{-1}) is in fact essentially indistinguishable from that reported for $e_{CB}^{-\star}$-exciton (negative trion) Auger relaxation in undoped semiconductor nanocrystals (0.88×10^{-10} cm^3s^{-1} for CdSe/CdS QDs,[41] see Appendix A). To understand this most prominent qualitative difference between Mn^{2+}- doped and undoped QDs, the important role of excited-state lifetime must be acknowledged. As seen from eq 2.1, Auger de-excitation competes against intrinsic relaxation. Modification of the PL decay kinetics therefore alters the competitiveness of the Auger quenching process.

Figure 2.8c shows simulated PL versus potential curves calculated as a function of PL rate constant (replacing k_{Mn} in eq 2.1 with k_{PL}) using the same model and parameters outlined above. This figure shows that the voltage difference between absorption and PL response curves is a function of excited-state PL decay time. Increasing k_{PL} shifts the PL quenching to more negative potentials. Excitonic PL in many undoped QDs decays with $k_{PL} \approx 10^9$ s^{-1}, and the PL quenching curve for this rate constant reproduces the general experimental observations[41,57] of Auger de-excitation for such QDs, showing near coincidence of absorption bleach and PL quenching, and incomplete PL quenching even after complete filling of the $1S_e$ shell. More quantitatively, the

dashed line in Figure 2.5c shows the quenching predicted for undoped CdSe/CdS QDs, calculated using the above model and the reported values of $k_{ex} = 3.4 \times 10^9$ s^{-1} (ref 57) and $k_{Aug} = 0.88 \times 10^{-10}$ $cm^3 s^{-1}$ (ref 41), with all other parameters fixed at the values used to simulate the Mn^{2+}:CdS QD data (see Appendix A). The calculated and experimental results agree very well.

This analysis demonstrates that the exceptionally effective Auger de-excitation of Mn^{2+}-doped QDs is primarily attributable to the very long Mn^{2+} excited-state lifetime, which makes Auger de-excitation kinetically highly competitive according to eq 2.1.[‡] This kinetic competition is summarized schematically in Figure 2.8d, which illustrates less effective Auger de-excitation of short-lived excited states because of the smaller volume sampled by the CB electron on the excited-state decay time scale.

2.3 Conclusion

Complete and reversible quenching of Mn^{2+}-doped CdS QD photoluminescence has been achieved through reversible introduction of CB electrons into these QDs by electrochemical methods. The data show that these Mn^{2+}-doped QDs are far more sensitive to Auger quenching than their undoped QD analogues. This remarkably effective Auger de-excitation is understood in terms of energy transfer from Mn^{2+} in its $^4T_1$ excited state to a CB electron, enabled by strong *s-d* exchange, a large density of acceptor states at the correct energies, and in particular the long Mn^{2+} excited-state lifetime. The large voltage difference between absorption and PL responses of the Mn^{2+}: CdS QDs is primarily a consequence of the very long Mn^{2+} excited-state lifetime. The striking sensitivity of Mn^{2+}-doped nanocrystal PL to Auger quenching strongly suggests that the impact of Auger processes on studies of blinking[25,31] or high-power photoexcitation[35–37] of doped semiconductor nanocrystals should be exacerbated compared to undoped nanocrystals. Such ef-

[‡]For the same reason, the less effective quenching of trap PL with charging observed in Figure 2.4b is consistent with the faster trap PL decay ($k_{PL} \approx 4 \times 10^7$ s^{-1}, see Appendix A).

fective Auger de-excitation could also define the fundamental limits of doped-nanocrystal-based electroluminescent devices.[48]

The deviation from the thermal equilibrium model observed at very low electron concentrations ($\sim 10^{-8} < N_{e^-} <\sim 0.05\ e^-_{CB}$/QD) is also interesting. This deviation suggests that Auger de-excitation of Mn^{2+} PL could potentially provide a useful optical measure of electron mobilities in other QD films at such low carrier densities, where the usual methods are limited.[61,66] For example, QD Schottky junction solar cells[71] constitute an important class of devices where detailed information about mobilities at very low carrier densities (e.g., under ambient illumination) would be desirable. Electron-Mn^{2+} Auger quenching has been used for imaging charge carriers in semiconductor devices previously, allowing demonstration of spatial separation of the acceleration and impact excitation processes in high-field electroluminescence devices made from bulk Mn^{2+}:CaF_2.[9] With this precedent, the demonstration here of effective Auger de-excitation in Mn^{2+}-doped QD films suggests that Auger-based imaging might now be accessible in QD devices. This proposed application could be extended to other colloidal doped nanocrystal films with long-lived electronic excited states, such as Er^{3+}-doped colloidal Si nanocrystals.

Finally, the ability to quench Mn^{2+} PL so effectively with very few electrons may provide a mechanism for switching Mn^{2+} PL on time scales shorter than its intrinsic PL decay time, which would normally define the lower limit. In QD films, this possibility would rely on charge injection and diffusion being fast relative to Mn^{2+} PL decay. Experiments are presently underway to explore this possibility.

2.4 Notes to Chapter 2

[1] Allen, J. W. *J. Phys. C: Solid State Phys.* **1986**, *19*, 6287.

[2] Bringuier, E. *J. Appl. Phys.* **1991**, *70*, 4505.

[3] Bringuier, E. *J. Appl. Phys.* **1994**, *75*, 4291–4312.

[4] Adachi, D.; Hasui, S.; Toyama, T.; Okamoto, H. *Appl. Phys. Lett.* **2000**, *77*, 1301–1303.

[5] Yang, H.; Holloway, P. H. *J. Phys. Chem. B* **2003**, *107*, 9705–9710.

[6] Yang, H.; Holloway, P. H.; Ratna, B. B. *J. Appl. Phys.* **2003**, *93*, 586–592.

[7] Adachi, D.; Morimoto, T.; Hama, T.; Toyama, T.; Okamoto, H. *J. Non-Cryst. Solids* **2008**, *354*, 2740–2743.

[8] Wood, V.; Halpert, J. E.; Panzer, M. J.; Bawendi, M. G.; Bulovic, V. *Nano Lett.* **2009**, *9*, 2367–2371.

[9] Langer, J. M.; Lemanska-Bajorek, A.; Suchocki, A. *Appl. Phys. Lett.* **1981**, *39*, 386–388.

[10] Suchocki, A.; Langer, J. M. *Phys. Rev. B* **1989**, *39*, 7905.

[11] Palm, J.; Gan, F.; Zheng, B.; Michel, J.; Kimerling, L. C. *Phys. Rev. B* **1996**, *54*, 17603–17615.

[12] Priolo, F.; Franzo, G.; Coffa, S.; Carnera, A. *Phys. Rev. B* **1998**, *57*, 4443–4455.

[13] Kik, P. G.; Polman, A. *J. Appl. Phys.* **2002**, *91*, 534–536.

[14] Kik, P. G.; Polman, A. *J. Appl. Phys.* **2000**, *88*, 1992–1998.

[15] Maurizio, C.; Iacona, F.; D'Acapito, F.; Franzo, G.; Priolo, F. *Phys. Rev. B* **2006**, *74*, 205428.

[16] Beaulac, R.; Ochsenbein, S. T.; Gamelin, D. R. In *Nanocrystal Quantum Dots*, 2nd ed.; Klimov, V. I., Ed.; Taylor & Francis: London, 2010.

[17] Suyver, J. F.; Wuister, S. F.; Kelly, J. J.; Meijerink, A. *Phys. Chem. Chem. Phys.* **2000**, *2*, 5445–5448.

[18] Norris, D. J.; Yao, N.; Charnock, F. T.; Kennedy, T. A. *Nano Lett.* **2000**, *1*, 3–7.

[19] Schwartz, D. A.; Norberg, N. S.; Nguyen, Q. P.; Parker, J. M.; Gamelin, D. R. *J. Am. Chem. Soc.* **2003**, *125*, 13205–13218.

[20] Archer, P. I.; Santangelo, S. A.; Gamelin, D. R. *J. Am. Chem. Soc.* **2007**, *129*, 9808–9818.

[21] Archer, P. I.; Santangelo, S. A.; Gamelin, D. R. *Nano Lett.* **2007**, *7*, 1037–1043.

[22] Pradhan, N.; Peng, X. *J. Am. Chem. Soc.* **2007**, *129*, 3339–3347.

[23] Beaulac, R.; Archer, P. I.; van Rijssel, J.; Meijerink, A.; Gamelin, D. R. *Nano Lett.* **2008**, *8*, 2949–2953.

[24] Beaulac, R.; Archer, P. I.; Liu, X.; Lee, S.; Salley, G. M.; Dobrowolska, M.; Furdyna, J. K.; Gamelin, D. R. *Nano Lett.* **2008**, *8*, 1197–1201.

[25] Zhang, Y.; Gan, C.; Muhammad, J.; Battaglia, D.; Peng, X.; Xiao, M. *J. Phys. Chem. C* **2008**, *112*, 20200–20205.

[26] Nag, A.; Chakraborty, S.; Sarma, D. D. *J. Am. Chem. Soc.* **2008**, *130*, 10605–10611.

[27] Beaulac, R.; Schneider, L.; Archer, P. I.; Bacher, G.; Gamelin, D. R. *Science* **2009**, *325*, 973–976.

[28] Bussian, D. A.; Crooker, S. A.; Yin, M.; Brynda, M.; Efros, A. L.; Klimov, V. I. *Nat. Mater.* **2009**, *8*, 35–40.

[29] Vlaskin, V. A.; Beaulac, R.; Gamelin, D. R. *Nano Lett.* **2009**, *9*, 4376–4382.

[30] Ochsenbein, S. T.; Feng, Y.; Whitaker, K. M.; Badaeva, E.; Liu, W. K.; Li, X.; Gamelin, D. R. *Nat. Nanotech.* **2009**, *4*, 681–687.

[31] Ishizumi, A.; Kanemitsu, Y. *J. Phys. Soc. Jpn.* **2009**, *78*, 083706–1 to 083706–4.

[32] Yu, J. H. et al. *Nat. Mater.* **2010**, *9*, 47–53.

[33] Vlaskin, V. A.; Janssen, N.; van Rijssel, J.; Beaulac, R.; Gamelin, D. R. *Nano Lett.* **2010**, *10*, 3670–3674.

[34] Li, Z.; Cheng, L.; Sun, Q.; Zhu, Z.; Riley, M. J.; Aljada, M.; Cheng, Z.; Wang, X.; Hanson, G. R.; Qiao, S.; Smith, *Angew. Chem. Int. Ed.* **2010**, *49*, 2777–2781.

[35] Chen, O.; Shelby, D. E.; Yang, Y.; Zhuang, J.; Wang, T.; Niu, C.; Omenetto, N.; Cao, Y. C. *Angew. Chem. Int. Ed.* **2010**, *49*, 10132–10135.

[36] Chen, H.-Y.; Chen, T.-Y.; Son, D. H. *J. Phys. Chem. C* **2010**, *114*, 4418–4423.

[37] Taguchi, S.; Ishizumi, A.; Kanemitsu, Y. *J. Phys. Soc. Jpn.* **2010**, *79*, 063710.

[38] Zu, L.; Wills, A. W.; Kennedy, T. A.; Glaser, E. R.; Norris, D. J. *J. Phys. Chem. C* **2010**, *114*, 21969–21975.

[39] Ochsenbein, S. T.; Gamelin, D. R. *Nat. Nanotech.* **2011**, *6*, 112–115.

[40] Carreras, J.; Bonafos, C.; Montserrat, J.; Dominguez, C.; Arbiol, J.; Garrido, B. *Nanotechnology* **2008**, *19*, 205201.

[41] Jha, P. P.; Guyot-Sionnest, P. *ACS Nano* **2009**, *3*, 1011–1015.

[42] Klimov, V. I.; McGuire, J. A.; Schaller, R. D.; Rupasov, V. I. *Phys. Rev. B* **2008**, *77*, 195324.

[43] Wehrenberg, B. L.; Wang, C.; Guyot-Sionnest, P. *J. Phys. Chem. B* **2002**, *106*, 10634–10640.

[44] Efros, A. L.; Rosen, M. *Phys. Rev. Lett.* **1997**, *78*, 1110.

[45] Frantsuzov, P.; Kuno, M.; Janko, B.; Marcus, R. A. *Nat. Phys.* **2008**, *4*, 519–522.

[46] Zhao, J.; Nair, G.; Fisher, B. R.; Bawendi, M. G. *Phys. Rev. Lett.* **2010**, 157403.

[47] Krauss, T. D.; Peterson, J. J. *J. Phys. Chem. Lett.* **2010**, *1*, 1377–1382.

[48] Rosen, S.; Schwartz, O.; Oron, D. *Phys. Rev. Lett.* **2010**, *104*, 157404.

[49] Yu, W. W.; Qu, L.; Guo, W.; Peng, X. *Chem. Mater.* **2003**, *15*, 2854–2860.

[50] Chung, J. H.; Ah, C. S.; Jang, D.-J. *J. Phys. Chem. B* **2001**, *105*, 4128–4132.

[51] Toropov, A. A.; Sorokin, S. V.; Kuritsyn, K. A.; Ivanov, S. V.; Pozina, G.; Bergman, J. P.; Wagner, M.; Chen, W. M.; Monemar, B.; Waag, A.; Yakovlev, D. R.; Sas, C.; Ossau, W.; Landwehr, G. *Physica E* **2001**, *10*, 362–367.

[52] Seufert, J.; Bacher, G.; Scheibner, M.; Forchel, A.; Lee, S.; Dobrowolska, M.; Furdyna, J. K. *Phys. Rev. Lett.* **2002**, *88*, 027402.

[53] Dorain, P. B. *Phys. Rev.* **1958**, *112*, 1058.

[54] Furdyna, J. K., Kossut, J., Eds. *Semiconductors and Semimetals*; Semiconductors and Semimetals; Elsevier, 1988; Vol. 25; pp ii –.

[55] Haram, S. K.; Quinn, B. M.; Bard, A. J. *J. Am. Chem. Soc.* **2001**, *123*, 8860–8861.

[56] Guyot-Sionnest, P.; Wang, C. *J. Phys. Chem. B* **2003**, *107*, 7355–7359.

[57] Jha, P. P.; Guyot-Sionnest, P. *J. Phys. Chem. C* **2007**, *111*, 15440–15445.

[58] Wehrenberg, B. L.; Guyot-Sionnest, P. *J. Am. Chem. Soc.* **2003**, *125*, 7806–7807.

[59] Bard, A. J.; Faulkner, L. R. *Electrochemical Methods: Fundamentals and Applications*, 2nd ed.; John Wiley & Sons, Inc: New York, 2001.

[60] Houtepen, A. J.; Vanmaekelbergh, D. *J. Phys. Chem. B* **2005**, *109*, 19634–19642.

[61] Yu, D.; Wang, C.; Guyot-Sionnest, P. *Science* **2003**, *300*, 1277–1280.

[62] Gordon, N. T.; Allen, J. W. *Solid State Commun.* **1981**, *37*, 441–443.

[63] Ayling, S. G.; Allen, J. W. *J. Phys. C.: Solid State Phys.* **1987**, *20*, 4251–4257.

[64] Lannoo, M.; Delerue, C.; Allan, G. *Phys. Rev. Lett.* **1995**, *74*, 3415.

[65] Vanmaekelbergh, D.; Liljeroth, P. *Chem. Soc. Rev.* **2005**, *34*, 299–312.

[66] Yu, D.; Wehrenberg, B. L.; Jha, P.; Ma, J.; Guyot-Sionnest, P. *J. Appl. Phys.* **2006**, *99*, 104315.

[67] Liu, Y.; Gibbs, M.; Puthussery, J.; Gaik, S.; Ihly, R.; Hillhouse, H. W.; Law, M. *Nano Lett.* **2010**, *10*, 1960–1969.

[68] Nawrocki, M.; Lascaray, J. P.; Coquillat, D.; Demianiuk, M. *MRS Onl. Proceed. Lib.* **1986**, *89*.

[69] Beaulac, R.; Gamelin, D. R. *Phys. Rev. B* **2010**, *82*, 224401.

[70] Rohlfing, M.; Kruger, P.; Pollmann, J. *Phys. Rev. Lett.* **1995**, *75*, 3489.

[71] Luther, J. M.; Law, M.; Beard, M. C.; Song, Q.; Reese, M. O.; Ellingson, R. J.; Nozik, A. J. *Nano Lett.* **2008**, *8*, 3488–3492.

Chapter 3

Photochemical Electronic Doping of Colloidal CdSe Nanocrystals

A method for electronic doping of colloidal CdSe nanocrystals (NCs) is reported. Anaerobic photoexcitation of CdSe NCs in the presence of a borohydride hole quencher, Li[Et_3BH], yields colloidal *n*-type CdSe NCs possessing extra conduction-band electrons compensated by cations deposited by the hydride hole quencher. The photodoped NCs possess excellent optical quality and display the key spectroscopic signatures associated with NC *n*-doping, including a bleach at the absorption edge, appearance of a new IR absorption band, and Auger quenching of the excitonic photoluminescence. Although stable under anaerobic conditions, these spectroscopic changes are all reversed completely upon exposure of the *n*-doped NCs to air. Chemical titration of the added electrons confirms previous correlations between absorption bleach and electron accumulation and provides a means of quantifying the extent of electron trapping in some NCs. The generality of this photodoping method is demonstrated by initial results on colloidal CdE (E = S, Te) NCs as well as on CdSe quantum dot films. The work in this chapter is reprinted with permission from Rinehart, J. D., Schimpf, A. M., Weaver, A. L., Cohn, A. W., Gamelin, D. R. *J. Am. Chem. Soc.*, **2013**, *135*, 18782-18785.

3.1 Introduction

The generation and manipulation of charge carriers in semiconductor nanostructures is central to emerging solar,[1–5] battery,[6,7] nanoelectronics,[8] and nanospintronics[9–11] technologies, as well as to nanocrystal (NC) blinking and multicarrier Auger processes that impact the use of such nanostructures as phosphors in display, lasing, or imaging technologies.[12–14] To study the physical properties of semiconductor nanostructures possessing "extra" charge carriers, chemical reduction of colloidal NCs,[15] electrochemical reduction of quantum dot (QD) solids,[16] and low-temperature charge separation[17] have been used to introduce the carriers. Many of these processes involve harsh reductants, require precipitation and ligand exchange, or only occur at cryogenic temperatures. A general method for introducing additional charge carriers to freestanding colloidal NCs would enable a wide variety of experiments and applications involving electronically doped semiconductor NCs.

Photochemistry offers a convenient *in situ* method for modulating carrier densities in colloidal NCs. For photochemical *n*-doping, capture of photogenerated holes by suitable hole quenchers strands extra electrons inside the NCs, compensated by cations deposited upon quencher oxidation. This method has been applied successfully with several oxide semiconductor NCs.[18–21] Although chalcogenide semiconductor NCs are frequently used as sensitizers in solar photochemistry, photovoltaic, and photoelectrochemical devices because of their strong visible absorption and ability to separate photogenerated charges,[1–5] photochemical electronic doping of this class of nanomaterials has not been explored. In contrast with oxides, chalcogenides such as CdE (E = S, Se, Te) possess shallow valence bands and are consequently not as reactive toward many hole quenchers commonly used with oxides. For generality, more reactive hole quenchers are thus required. Here, we report facile and reversible photodoping of colloidal CdSe NCs using a reactive borohydride, $Li[Et_3BH]$, as the hole quencher (Figure 3.1). This photodoping allows formation of kinetically stable colloidal *n*-type CdSe NCs without the surface degradation caused by chemical reductants

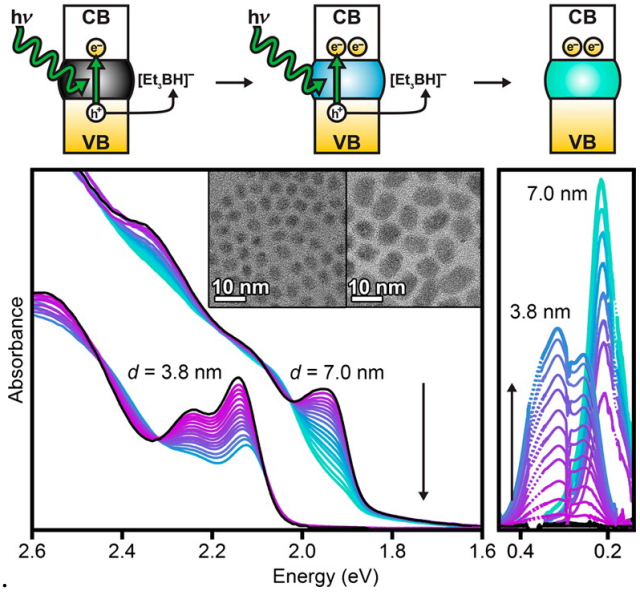

Figure 3.1: Top: Nanocrystal photodoping using Li[Et_3BH]. The photogenerated hole (h^+) is quenched by Li[Et_3BH], leaving an electron (e^-) in the conduction band. Further photoexcitation can add more electrons. **Bottom:** Absorption spectra of $d = 3.8$ nm and $d = 7.0$ nm CdSe NCs at various stages of photodoping starting from no prior photoexcitation (black) to maximum photodoping (teal). The data show exciton bleach and growth of IR absorption with photodoping. **Inset:** TEM images of these NCs.

examined previously. Moreover, this approach allows CdSe NCphotodoping even in the presence of ZnSe shells that impede direct electron injection. Although the present work is focused on colloidal CdSe QDs, it is expected to be broadly applicable for preparing *n*-type NCs in various forms. Proof-of-concept results confirm successful CdE (E = S, Te) QD photodoping, as well as photodoping of CdSe QD solids.

3.2 Results & Discussion

3.2.1 Photodoping

Colloidal trioctylphosphine-oxide-ligated CdSe NCs with average diameters (d) of 3.8 and 7.0 nm, as determined by excitonic absorption and transmission electron microscopy (Figure 3.1), were prepared by established synthetic procedures.[22] These NCs were transferred to dry, deoxygenated

toluene and stored in the presence of excess trioctylphosphine oxide under inert atmosphere. Under these conditions, exposure to visible or UV radiation does not alter the NC spectra or cause sample degradation. After addition of $Li[Et_3BH]$ to these suspensions, exposure to light exceeding the band gap energy causes a bleach of the first excitonic absorption feature (Figure 3.1). This bleach occurs even with excitation solely by ambient room light, but no absorption changes are detected without photoexcitation (Figure B.3). The absorption bleach approaches an asymptotic limit with extended photoexcitation. When the absorption spectrum is unchanged over $\sim$30 s of photoexcitation, the samples are considered to have reached their maximum photodoping. Photodoping can be halted at any intermediate stage, the partially photodoped CdSe NCs used for spectroscopic measurements, and the photoexcitation then resumed to increase photodoping up the asymptotic limit. After spectroscopic or other measurements are complete, exposure of these *n*-doped NCs to an oxidant such as O_2 (air) completely reverses the absorption bleach (*vide infra*).

The absorption bleach is a signature of the presence of one or more delocalized electrons in the quantum-confined CdSe NC conduction band.[15] This bleach is accompanied by a concurrent redshift of the first two excitonic absorption bands (*e.g.*, ~ -15 meV for the d = 3.8 nm CdSe NCs at maximum photodoping in Figure 3.1, see Figure B.4). This redshift is comparable to that of trion luminescence relative to neutral exciton luminescence in other CdSe QDs[23,24] and is thus tentatively attributed to the reduced energy required for trion formation by photoexcitation of *n*-doped CdSe NCs. Electrostatic exciton stabilization by localized charges may also contribute to the redshift. Infrared absorption spectroscopy verifies the presence of extra quantum confined electrons, showing intense new absorption corresponding to intra-band excitations of the newly introduced conduction electrons (Figure 3.1), with an energy that increases with decreasing NC diameter. A per-electron molar extinction coefficient of $(8.9 \pm 0.6) \times 10^4$ $M_e^{-1} \cdot cm^{-1}$ is estimated at the IR absorption maximum (0.32 eV) of d = 3.8 nm CdSe NCs (Figure B.10). This IR absorption verifies that the added electrons do not simply reside in localized trap states. Interestingly, the IR absorption of the smaller NCs shows distinct structure. Similar structure has been seen

previously in chemically reduced CdSe NCs[15] and may reflect a low-symmetry splitting of the $1P_e$ degeneracy. The IR absorption grows with photodoping (Figure 3.1), and in some cases blueshifts slightly. These blueshifts are small compared to those observed in ZnO NCs heavily photodoped (average electron density, $\langle N_{\max} \rangle \approx 6 \times 10^{20}$ cm^{-3}) using the same hole quencher,[21] suggesting smaller carrier densities in the photodoped CdSe NCs. The IR spectroscopic changes are also fully reversed upon NC reoxidation by exposure to air.

3.2.2 Electron Density

To quantify the maximum (average) number of excess electrons per NC ($\langle n_{\max} \rangle$) achievable by these methods, the magnitude of the absorption bleach was analyzed. Previous studies have established a linear correlation between the number of CdSe conduction-band electrons and the fractional bleach at the first excitonic absorption maximum, where a 100% bleach corresponds to 2 conduction-band electrons.[19,25] By Gaussian deconvolution of the data in Figure 3.1 (Figure B.4), we find a maximum bleach of 41% for the d = 3.8 nm CdSe NCs and 98% for the d = 7.0 nm CdSe NCs. The data in Figure 3.1 thus suggest $\langle n_{\max} \rangle \approx 0.8$ $\left(\langle N_{\max} \rangle \approx 2.8 \times 10^{19} \text{ cm}^{-3}\right)$ and 2 $\left(\langle N_{\max} \rangle \approx 1.1 \times 10^{19} \text{ cm}^{-3}\right)$, respectively.

An attractive aspect of the photodoping method described here is that the resulting n-type NCs are amenable to direct chemical titration of the added electrons, something not possible with chemically reduced NCs because of the excess reductant present under equilibrium conditions. Chemical titration of excess electrons in chalcogenide NCs has not been described previously. Figure 3.2 shows electronic absorption spectra of the 3.8 nm CdSe NCs from Figure 3.1 before photodoping, at maximum photodoping, and at various stages of reoxidation by $[FeCp^{\star}_2]\,[BAr_F]$ ($[FeCp^{\star}_2]^+$ = decamethylferrocenium, $[BAr_F]^-$ = tetrakis[3,5-bis(trifluoromethyl)phenyl]borate). Titration of these 3.8 nm NCs yields an $\langle n_{\max} \rangle$ of 0.97, consistent with the spectroscopic estimation. Titrations were also performed on d = 4.6 and 7.0 nm CdSe samples (B). Titration of the 4.6 nm NCs yields $\langle n_{\max} \rangle$ = 1.1, similar to the 1.4 estimated using absorption spectroscopy. By contrast, although the

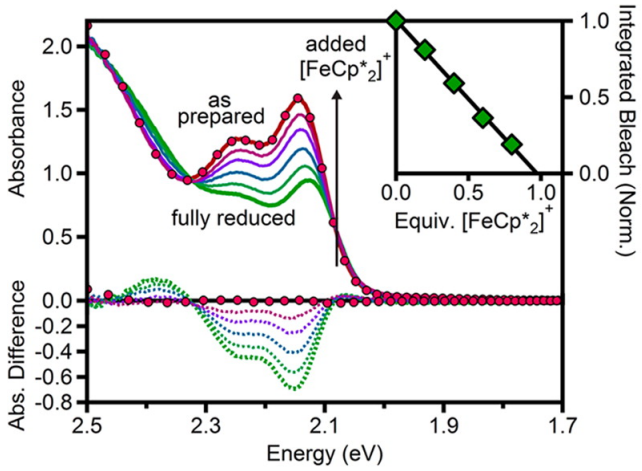

Figure 3.2: Absorption spectra of d = 3.8 nm (43 μM) CdSe NCs collected during redox titration in 1:1 toluene/THF. The red spectrum shows data collected before introduction of Li[Et_3BH]. The solid green spectrum is of the maximally photodoped NCs, and the red circles represent the reoxidized NCs. The intermediate spectra were collected following incremental oxidation by addition of $[FeCp^{\star}_2]^+$ aliquots. The corresponding difference spectra ($A - A_{\text{as prepared}}$) are plotted as dotted lines. **Inset:** Integrated absorption bleach of the first excitonic feature as a function of $[FeCp^{\star}_2]^+$ equivalents, with a solid line showing the best linear fit to the data. The crossing of this line with zero indicates 0.97 electron per NC.

absorption bleach of the 7.0 nm CdSe suggests $\sim$ 2.0 conduction-band electrons per NC, titration requires nearly 30 equiv of $[FeCp^{\star}_2]\,[BAr_F]$. This divergence suggests substantial electron trapping in these NCs, *e.g.*, by surface diselenide bonds.[26] Many previous experiments have suggested the existence of near-band-edge electron traps in CdSe NCs. Such traps have been proposed to play major roles in blinking and other physical processes,[5,13,27] but little is known about their potentials, densities, or redox reactivities. These results emphasize that titration is also sensitive to other electrons accessible at the potential defined by the titrant, such as trapped electrons that do not contribute to the band-edge absorption bleach, and titration therefore complements the spectroscopic evaluation described above.

3.2.3 Photoluminescence Studies

A second attractive feature of this photodoping methodology is that the resulting colloidal *n*-type NCs are of high spectroscopic quality, making them well suited for advanced characterization by

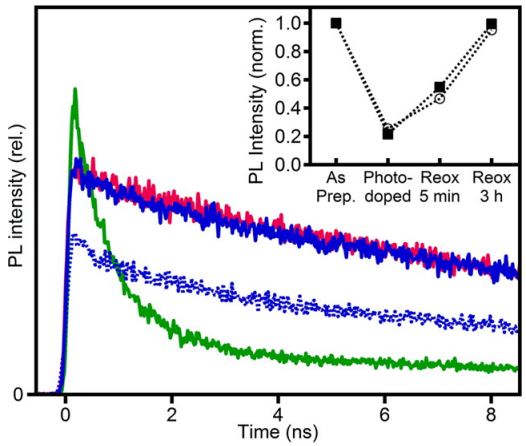

Figure 3.3: Time-resolved photoluminescence decay of d = 4.6 nm CdSe/ZnSe NCs measured before photodoping (red), after photodoping (green), after 5 min reoxidation in air (dotted blue), and after 3 h in air (solid blue). **Inset:** Normalized steady-state (squares) and time-resolved (at 7.5 ns, circles) photoluminescence intensities showing slow reoxidation in air.

various spectroscopic techniques. For illustration, Figure 3.3 summarizes the changes in room-temperature photoluminescence of d = 4.6 nm CdSe NCs upon photodoping. For these measurements, thin ZnSe shells were grown around the NCs to passivate surface traps and hence suppress nonradiative decay. Prior to photodoping, these NCs show single-exponential excitonic photoluminescence decay with a time constant of $\tau = 16$ ns. After photodoping to $\langle n \rangle \approx 0.5$ (estimated by absorption spectroscopy), their steady-state photoluminescence is quenched by $\sim 80\%$ (Figure 3.3, inset), and the two characteristic signatures of trion decay are observed in their photoluminescence decay curves: (1) an increase in luminescence intensity at short times (<500 ps) relative to the neutral NCs, and (2) appearance of a fast decay component attributable to Auger recombination. The persistence of a slow decay component in the photodoped sample reflects the presence of some undoped CdSe NCs, as expected for $\langle n \rangle \approx 0.5$. Analysis of these data yields a trion decay time of $\tau_{\infty -} = 750$ ps that agrees well with those reported previously for electrochemically reduced CdSe/CdS core/shell NCs in films,[28] but here has been collected on a high-optical-quality colloidal suspension with minimal sample perturbation.

A systematic investigation of the size dependence of negative trion (T^-) Auger recombination

rates in free-standing colloidal CdSe nanocrystals was then explored by Cohn *et al.*[29] Colloidal n-type CdSe nanocrystals of various radii are prepared photochemically, and their trion decay dynamics are measured using time-resolved photoluminescence spectroscopy. Trion Auger time constants spanning 3 orders of magnitude are observed, ranging from 57 ps (radius R = 1.4 nm) to 2.2 ns (R = 3.2 nm). The data reveal a substantially stronger size dependence than found for bi- or multiexciton Auger recombination in CdSe or other semiconductor nanocrystals, scaling in proportion to $R^{4.3}$.

Like absorption, the luminescence also recovers completely upon introduction of air, but this recovery is markedly slower than the absorption recovery. Whereas absorption recovers within seconds of exposure to air, both the time-resolved and steady-state luminescence intensities have not fully recovered even after 5 min in air (Figure 3.3, inset). This discrepancy indicates that the NC photoluminescence is sensitive not only to the presence of conduction-band electrons but also to other changes induced upon photodoping, which we tentatively associate with electron trapping. These results suggest that deeply trapped electrons react more slowly with air than conduction electrons do, as might be anticipated from Marcus theory considerations. The reactivities and reaction dynamics of redox-active traps in semiconductor NCs have been of central interest to many aspects of NC photophysics and electronics,[3,5,13,27] and the present results illustrate a promising new avenue for deliberate investigation of such trap chemistries.

3.2.4 Chemical vs. Photochemical

A final important feature of this photodoping methodology that distinguishes it from all other chalcogenide NC reduction strategies reported to date is that electrons are placed in the conduction band by photoexcitation, not by equilibrium electron injection. Photodoping is fundamentally governed by the reactivities of the quenchers toward the photogenerated holes.[21] For some applications, *n*-type nanostructures encapsulated within barrier heterostructures may be desired. In other cases, competing redox reactions may interfere with direct NC reduction. To illustrate, Figure 3.4

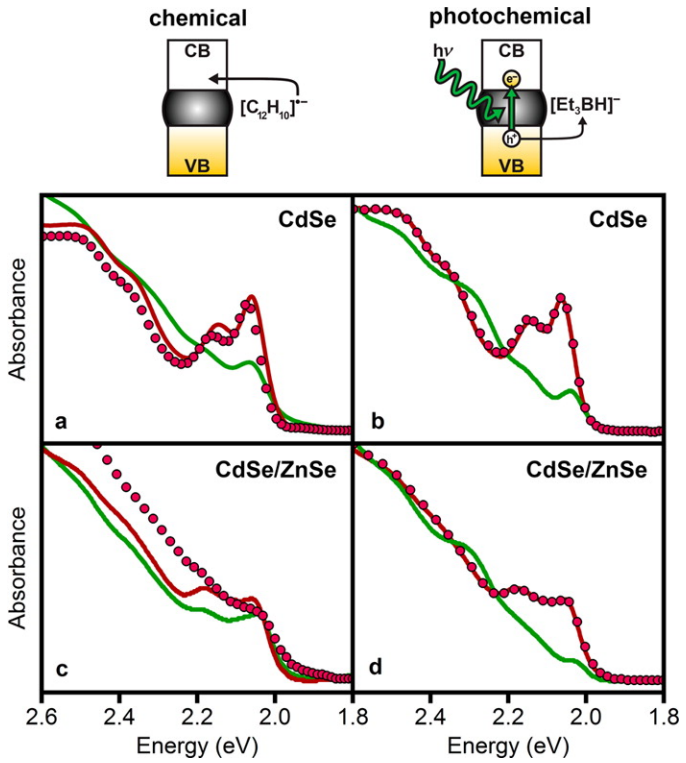

Figure 3.4: Top: Scheme outlining chemical and photochemical doping methods. Absorption spectra of d = 4.6 nm CdSe NCs with and without a $\sim$ 1 nm ZnSe shell, measured before reduction (red lines), after maximum reduction (green lines), and after reoxidation by air (red circles). Panels **a** and **c** show reduction of core and core/shell NCs using 103 and 104 equiv of Na[biphen], respectively. Panels **b** and **d** show photodoping of the same core and core/shell NCs, respectively, using $\sim$ 50 equiv of Li[Et_3BH].

summarizes the results obtained when the d = 4.6 nm CdSe NCs of Figure 3.3 and the same NCs with $\sim$ 1 nm thick ($\sim$ 4 monolayers) ZnSe shells were reduced by either chemical or photochemical methods. For chemical reduction, Na[biphen] ([biphen]$^{\bullet-}$ = biphenyl radical anion) was used, as reported previously.[15]

Figure 3.4a shows that addition of 103 equiv of Na[biphen] reduces the core d = 4.6 nm CdSe NCs, consistent with literature results.[15] The absorption bleach is similar to that achieved photochemically with the same NCs (Figure 3.4b, both $\sim$ 60%), albeit with the appearance of a small sub-bandgap tail and less complete reversibility in the case of chemical reduction. The core/shell NCs show markedly different results: Incremental addition of up to 104 equiv of Na[biphen] causes only a small ($\sim$ 20%) bleach of the first excitonic absorption (Figure 3.4c). A large sub-bandgap absorption tail and an offset at higher energy are observed, suggestive of scattering due to NC clustering or absorption due to trapped electrons. Furthermore, the spectral changes are only partially reversed upon exposure to air, suggesting substantial NC degradation. These irreversible changes are attributed to deleterious side reactions of the chemical reductant, Na[biphen]. In contrast, photodoping the same core/shell NCs (Figure 3.4d) yields a clean $\sim$ 85% bleach of the first exciton that is rapidly and completely reversed upon exposure to air. These data demonstrate superior results with photodoping compared to chemical reduction. The high optical quality of the photodoped NC samples and the excellent reversibility of the photodoping will facilitate future spectroscopic and electronic structure studies of these and related n-type nanostructures.

3.2.4.1 Photodoping of CdE (E = S, Te) nanocrystals

Although this study has focused on colloidal CdSe QDs, preliminary results have also been obtained for colloidal CdE (E = S, Te) NCs and CdSe QD films (B). CdE (E= S, Te) NCs of d = 6.0 and 4.1 nm were prepared by established methods.[30,31] Anaerobic photoexcitation of these NCs in the presence of Li[Et_3BH] leads to successful photodoping as evidenced by a band-edge absorption bleach or new IR absorption similar to that obtained for photodoped CdSe NCs. Perhaps more

intriguingly, anaerobic photoexcitation of CdSe QD solids prepared by codeposition of $d = 7.0$ colloidal CdSe NCs with Li[Et_3BH] onto fluorine-doped tin oxide electrodes also yields comparable *n*-doping to that found in solution. In all cases, these changes are fully reversed upon reoxidation in air. These results, in conjunction with our recent demonstration of enhanced ZnO NC photodoping using Li[Et_3BH],[21] demonstrate this as a general and versatile approach for preparing *n*-type semiconductor NCs, both in colloidal suspensions and in solids. The precise roles played by the charge-compensating cations (Li^+, H^+) in this chemistry remain an open topic for future research. In ZnO NCs, bulky cations slow and decrease the extent of photodoping,[21] but it is not yet known whether small cations associate with the surfaces or can intercalate into the internal volumes of such photodoped NCs.

3.3 Summary

In summary, a new method for preparation of colloidal *n*-type CdSe nanocrystals has been demonstrated that involves photodoping using Li[Et_3BH] as a hole quencher. This hydride is commercially available, shelf-stable, and compatible with the solvents and ligands commonly used for colloidal semiconductor NCs. The *n*-type CdSe NCs prepared by this method are kinetically stable, show excellent optical quality, and are readily returned to their original oxidation state upon exposure to air. Photodoping is successful even for CdSe/ZnSe core/shell heterostructures that are significantly more difficult to reduce directly with Na[biphen]. This photodoping methodology is also applicable to other colloidal chalcogenide and oxide NCs, offering a facile general approach to *in situ* NC electronic doping. As such, this methodology will enable a broad range of fundamental science experiments to address *n*-type doped NC electronic structures, electron spin dynamics, QD plasmonics, and inter-NC electron-transfer processes, among other intriguing topics. It is equally attractive for *in situ*, nondestructive, tunable carrier doping of QD solids currently of interest in more applied areas of QD photovoltaics, photodetectors, and transistors.

3.4 Notes to Chapter 3

[1] Nozik, A. J.; Beard, M. C.; Luther, J. M.; Law, M.; Ellingson, R. J.; Johnson, J. C. *Chem. Rev.* **2010**, *110*, 6873–6890.

[2] Kramer, I. J.; Sargent, E. H. *ACS Nano* **2011**, *5*, 8506–8514.

[3] Ip, A. H. et al. *Nat. Nanotech.* **2012**, *7*, 577–582.

[4] Kamat, P. V. *J. Phys. Chem. Lett.* **2013**, *4*, 908–918.

[5] Zhu, H.; Song, N.; Lian, T. *J. Am. Chem. Soc.* **2013**, *135*, 11461–11464.

[6] Su, Q.; Chang, L.; Zhang, J.; Du, G.; Xu, B. *J. Phys. Chem. C* **2013**, *117*, 4292–4298.

[7] Gregorczyk, K. E.; Liu, Y.; Sullivan, J. P.; Rubloff, G. W. *ACS Nano* **2013**, *7*, 6354–6360.

[8] Hetsch, F.; Zhao, N.; Kershaw, S. V.; Rogach, A. L. *Mater. Today* **2013**, *16*, 312–325.

[9] Loss, D.; DiVincenzo, D. P. *Phys. Rev. A* **1998**, *57*, 120–126.

[10] Hanson, R.; Kouwenhoven, L. P.; Petta, J. R.; Tarucha, S.; Vandersypen, L. M. K. *Rev. Mod. Phys.* **2007**, *79*, 1217–1265.

[11] Awschalom, D. D.; Bassett, L. C.; Dzurak, A. S.; Hu, E. L.; Petta, J. R. *Science* **2013**, *339*, 1174–1179.

[12] Mahler, B.; Spinicelli, P.; Buil, S.; Quelin, X.; Hermier, J.-P.; Dubertret, B. *Nat. Mater.* **2008**, *7*, 659–664.

[13] Galland, C.; Ghosh, Y.; Steinbeck, A.; Sykora, M.; Hollingsworth, J. A.; Klimov, V. I.; Htoon, H. *Nature* **2011**, *479*, 203–207.

[14] Chen, O.; Zhao, J.; Chauhan, V. P.; Cui, J.; Wong, C.; Harris, D. K.; Wei, H.; Han, H.-S.; Fukumura, D.; Jain, R. K.; Bawendi, M. G. *Nat. Mater.* **2013**, *12*, 445–451.

[15] Shim, M.; Guyot-Sionnest, P. *Nature* **2000**, *407*, 981–983.

[16] Yu, D.; Wehrenberg, B. L.; Jha, P.; Ma, J.; Guyot-Sionnest, P. *J. Appl. Phys.* **2006**, *99*, 104315.

[17] Fernee, M. J.; Littleton, B. N.; Rubinsztein-Dunlop, H. *ACS Nano* **2009**, *3*, 3762–3768.

[18] Haase, M.; Weller, H.; Henglein, A. *J. Phys. Chem.* **1988**, *92*, 482–487.

[19] Shim, M.; Wang, C.; Guyot-Sionnest, P. *J. Phys. Chem. B* **2001**, *105*, 2369–2373.

[20] Liu, W. K.; Whitaker, K. M.; Smith, A. L.; Kittilstved, K. R.; Robinson, B. H.; Gamelin, D. R. *Phys. Rev. Lett.* **2007**, *98*, 186804.

[21] Schimpf, A. M.; Gunthardt, C. E.; Rinehart, J. D.; Mayer, J. M.; Gamelin, D. R. *J. Am. Chem. Soc.* **2013**, *135*, 16569–16577.

[22] Carbone, L. et al. *Nano Lett.* **2007**, *7*, 2942–2950.

[23] Shimizu, K. T.; Woo, W. K.; Fisher, B. R.; Eisler, H. J.; Bawendi, M. G. *Phys. Rev. Lett.* **2002**, *89*, 117401–.

[24] Patton, B.; Langbein, W.; Woggon, U. *Phys. Rev. B* **2003**, *68*, 125316–.

[25] Wang, C.; Shim, M.; Guyot-Sionnest, P. *Science* **2001**, *291*, 2390–2392.

[26] Voznyy, O.; Thon, S. M.; Ip, A. H.; Sargent, E. H. *J. Phys. Chem. Lett.* **2013**, *4*, 987–992.

[27] Tice, D. B.; Frederick, M. T.; Chang, R. P. H.; Weiss, E. A. *J. Phys. Chem. C* **2011**, *115*, 3654–3662.

[28] Jha, P. P.; Guyot-Sionnest, P. *ACS Nano* **2009**, *3*, 1011–1015.

[29] Cohn, A. W.; Rinehart, J. D.; Schimpf, A. M.; Weaver, A. L.; Gamelin, D. R. *Nano Lett.* **2013**, *14*, 353–358.

[30] Yu, W. W.; Peng, X. *Angew. Chem. Int. Ed.* **2002**, *41*, 2368–2371.

[31] Yu, W. W.; Qu, L.; Guo, W.; Peng, X. *Chem. Mater.* **2003**, *15*, 2854–2860.

Chapter 4

Photoluminescence Brightening via Electrochemical Trap Passivation in ZnSe and Mn^{2+}-Doped ZnSe Quantum Dots

Spectroelectrochemical experiments on wide-gap semiconductor nanocrystals (ZnSe and Mn^{2+}-doped ZnSe) have allowed the influence of trap electrochemistry on nanocrystal photoluminescence to be examined in the absence of semiconductor band filling. Large photoluminescence electrobrightening is observed in both materials upon application of a reducing potential and is reversed upon return to the equilibrium potential. Electrobrightening is correlated with the transfer of electrons into nanocrystal films, implicating reductive passivation of midgap surface electron traps. Analysis indicates that the electrobrightening magnitude is determined by competition between electron trapping and photoluminescence (ZnSe) or energy transfer (Mn^{2+}-doped ZnSe) dynamics within the excitonic excited state, and that electron trapping is extremely fast ($k_{trap} \approx 10^{11}$ s^{-1}). These results shed new light on the complex surface chemistries of semiconductor nanocrystals. The work in this chapter is reprinted with permission from Weaver, A. L., Gamelin, D. R. *J. Am. Chem. Soc.*, **2012**, *134*, 6819-6825.

4.1 Introduction

The photoluminescence (PL) of colloidal semiconductor nanocrystals (or quantum dots, QDs) is strongly influenced by surface chemistry. Surface states within the semiconductor optical gap may introduce effective nonradiative decay pathways that reduce PL quantum yields.[1–6] In some cases, surface traps can be passivated by judicious selection of capping ligands[2,7,8] or by growth of conformal inorganic shell layers,[9–15] increasing PL quantum yields. Trap passivation can even occur photochemically ("photobrightening"),[16–18] which has been proposed to involve photoinduced annealing,[19–21] photooxidation or reduction,[22] ligand chemistry,[23] photoinduced adsorption of small molecules,[24–26] or photoelectrification.[27–29] Photobrightening is influenced by reducing agents,[30] and in nanowires it has been enhanced by low levels of electron injection using an AFM tip.[31] Collectively, these data provide circumstantial evidence that QD PL may be manipulated by controlling the charge states of surface traps. Spectroelectrochemical studies of the relationship between surface-trap redox chemistry and QD PL are needed to test the validity of this hypothesis.

Previous spectroelectrochemical studies of colloidal QDs have focused primarily on charge injection into quantum confined band levels of easily reduced QDs with relatively positive conduction-band (CB) potentials (e.g., CdSe, CdS, ZnO, PbSe).[32–52] It is now established that electron injection into the CBs of colloidal chalcogenide QDs bleaches the first excitonic absorption ($1S_h \rightarrow 1S_e$), introduces new absorption due to intra-conduction-band ($1S_e \rightarrow 1P_e$) electronic excitation, and substantially diminishes excitonic PL quantum yields through electron-exciton Auger recombination.[33–36,38,40–48] To date, however, there have been no reports of the spectroelectrochemistry of semiconductor nanocrystals with very negative CB potentials, for which CB filling is deliberately avoided (e.g., ZnSe, ZnS). In such QDs, midgap surface states are exposed and readily accessible to electrochemical manipulation, making them particularly attractive for investigation of the influence of surface redox chemistry on nanocrystal photophysics.

Here, we describe the spectroelectrochemistry of ZnSe QDs. A remarkably large (~40-fold)

enhancement of steady-state PL is observed when ZnSe QDs are held under a cathodic bias. In agreement with recent blinking results,[51] this electrobrightening implicates elimination of a fast nonradiative channel for exciton deactivation *via* reductive surface electron-trap passivation. Incorporation of Mn^{2+} dopants into the ZnSe QDs introduces a well-defined fast exciton-deactivation pathway that allows the electron trap kinetics to be clocked. Analysis of the difference in PL electrobrightening magnitudes with and without Mn^{2+} yields an effective electron trapping rate constant of $\sim 10^{11}$ s^{-1}, comparable to that for energy transfer to Mn^{2+}, and much greater than that for excitonic PL. These findings provide new insight into the roles of surface trap states on QD photoluminescence.

4.2 Experimental Section

Colloidal ZnSe and Mn^{2+}:ZnSe QDs were synthesized and characterized as detailed previously.[53,54] QDs made by cluster thermolysis[53] and hot-injection[54] routes gave essentially identical results. QD films were prepared by depositing QD suspensions in toluene onto a 3-mercaptopropyl-trimethoxysilane treated fluorine doped tin oxide (FTO) surface, cross-linking the QDs with 1,7-heptanediamine, and curing under vacuum at 70°C for 1 h.[42,45,47] Absorption measurements were performed using a Cary 500 (Varian) spectrometer. Continuous-wave PL spectra were collected using either 363 nm excitation and a 0.5 m monochromator and CCD for detection, or 405 nm excitation and an Ocean Optics USB2000 spectrometer for detection. Time-resolved PL measurements were performed with excitation at 360 nm and PMT detection at 590 nm (25 nm spectral band-pass). Electrobrightening was independent of excitation wavelength. Photoluminescence quantum yields were measured on QD films using an integrating sphere and were assumed to be the same in the electrochemical cell at the equilibrium potential.

The electrochemical cells consisted of silver pseudo-reference electrodes, platinum counter electrodes, and films of QDs on FTO as the working electrodes. The cells were assembled un-

der N_2 atmosphere, with 0.1 M tetrabutylammonium perchlorate (TBAP) in dimethylformamide (DMF) as the electrolyte. The electrochemical experiments were conducted using a μ-autolab II potentiostat. All measurements were performed at room temperature in cuvettes sealed under anaerobic atmosphere. Care was taken to avoid illumination of the Ag^0 electrode. For estimation of the number of electrons added per QD, the number of QDs per unit area in a given film was estimated by absorption spectroscopy using an empirical ZnSe QD molar extinction coefficient of 4.6×10^5 $M^{-1}cm^{-1}$,[55] and the total number of electrons added to a QD film was estimated by integrating the time-resolved current obtained during a potential-step experiment after subtracting a baseline determined by the steady-state current at the applied potential.[32]

As observed previously,[50,56] the equilibrium potentials of these QD films drifted over the course of many hours, and differed for measurements performed on the same films on different days, or on different films of the same QDs. The drifting equilibrium potentials likely reflect the use of Ag^0 pseudo-reference electrodes. With the exception of such variations in equilibrium potential, however, all measurements yielded very similar results. Over 25 different films from four different QD syntheses were examined, and all showed essentially the same electrobrightening as reported here. The electrobrightening results are therefore always reported together with PL measured at or near the equilibrium potential. Within a given experiment, this drift was negligible and the electrobrightening was stable, reversible, and reproducible, as illustrated by the data reported here.

4.3 Results & Analysis

4.3.1 Electrobrightening

Figure 4.1a illustrates the electrochemical cells used to introduce charge carriers into ZnSe QD films. Starting at the equilibrium potential (V_{eq}), a cathodic bias was applied (V_{app}) while mon-

itoring the QD PL. The ZnSe QD CB potentials are very negative (~ -2.0 V *vs* Ag^0), allowing selective reduction of midgap traps without injection of electrons into the CB.

Figure 4.1b plots absorption and PL spectra of a ZnSe QD film at the equilibrium potential ($V_{eq} = -0.2$ V) and after electrobrightening at $V_{app} = -1.5$ V. The absorption spectrum of the colloidal ZnSe QDs shows the first excitonic maximum at ~ 385 nm, consistent with $d \approx 3.2$ nm nanocrystals. The PL spectrum of the same QDs in a film on FTO shows a weak excitonic feature at ~ 415 nm and broad trap emission centered at ~ 500 nm. Application of a cathodic bias leads to electron transfer into the QD film and increases the total PL quantum yield (including both excitonic and trap PL) from $\Phi \approx 0.7\%$ to $\Phi \approx 11\%$. The excitonic PL intensity at 385 nm changes by $I_{EB}/I_0 \approx 40$. Trap PL at 500 nm also increases with applied potential, by $I^{tr}_{EB}/I^{tr}_0 \approx 10$. Both exciton and trap PL electrobrightening are completely reversed when the cell is returned to its equilibrium potential and the electrons are removed (*vide infra*). There is no discernible change in QD absorbance over this potential range. These observations are consistent with electrochemical passivation of surface electron traps.

An impurity can be used to create well-defined midgap electronic states that introduce new very fast nonradiative exciton deactivation channels. If fast electron trapping diminishes excitonic PL quantum yields as suggested by the above results, then less PL electrobrightening should be observed in Mn^{2+}-doped ZnSe QDs, where nonradiative exciton-to-Mn^{2+} energy transfer within a few tens of picosecond[57–60] competes with electron trapping, and the resulting luminescent Mn^{2+} $^4T_1$ excited state is not susceptible to electron trapping. To test this hypothesis, similar spectro-electrochemical measurements were performed on films of Mn^{2+}- doped ZnSe QDs (Mn^{2+}:ZnSe). Figure 4.1c plots absorption and PL spectra of Mn^{2+}:ZnSe QDs. The absorption spectrum of the colloidal QDs (dotted) shows the first excitonic feature at ~ 412 nm, consistent with $d \approx 5.0$ *nm* nanocrystals. At the equilibrium potential ($V_{eq} = -0.3$ V), the PL spectrum of the same QDs in a film on FTO (dashed) is dominated by the Mn^{2+} $^4T_1 \rightarrow ^6A_1$ *d-d* transition centered at 595 nm,[61] with $\Phi \approx 9.5\%$. Under cathodic bias ($V_{app} = -1.5$ V), electrons are transferred into the QD film

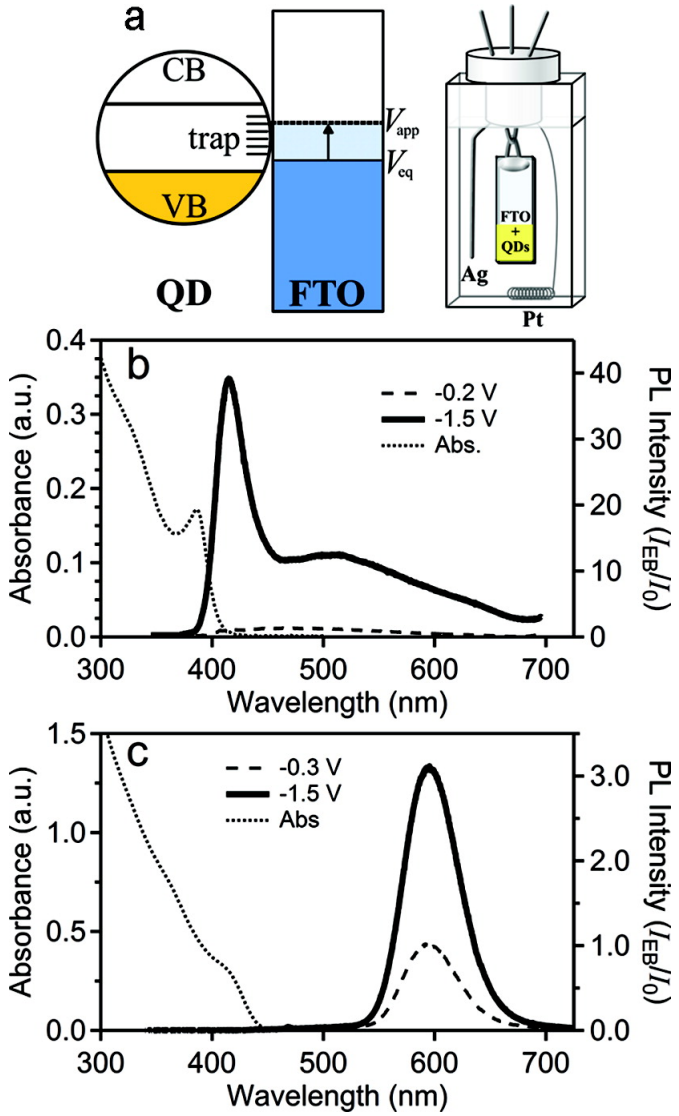

Figure 4.1: Spectroelectrochemistry of ZnSe QD films. **(a)** A schematic of an electrochemical cell (right) with a silver pseudo-reference electrode, platinum counter electrode, and a film of QDs on FTO as the working electrode. For V_{app} above the equilibrium potential of the working electrode, V_{eq}, midgap electron traps are filled (left). **(b)** The excitonic PL spectra at $V_{eq} = -0.2$ V (dashed) and after electrobrightening at $V_{app} = -1.5$ V (solid) *vs* Ag^0 for a ZnSe QD film. λ_{ex} = 363 nm. The absorption of the same ZnSe QDs as colloids is shown as a dotted line. **(c)** The Mn^{2+} PL spectra at the equilibrium potential of $V_{eq} = -0.3$ V (dashed), and after electrobrightening at $V_{app} = -1.5$ V (solid). λ_{ex} = 405 nm. The absorption of the colloidal Mn^{2+}:ZnSe QDs is shown as a dotted line.

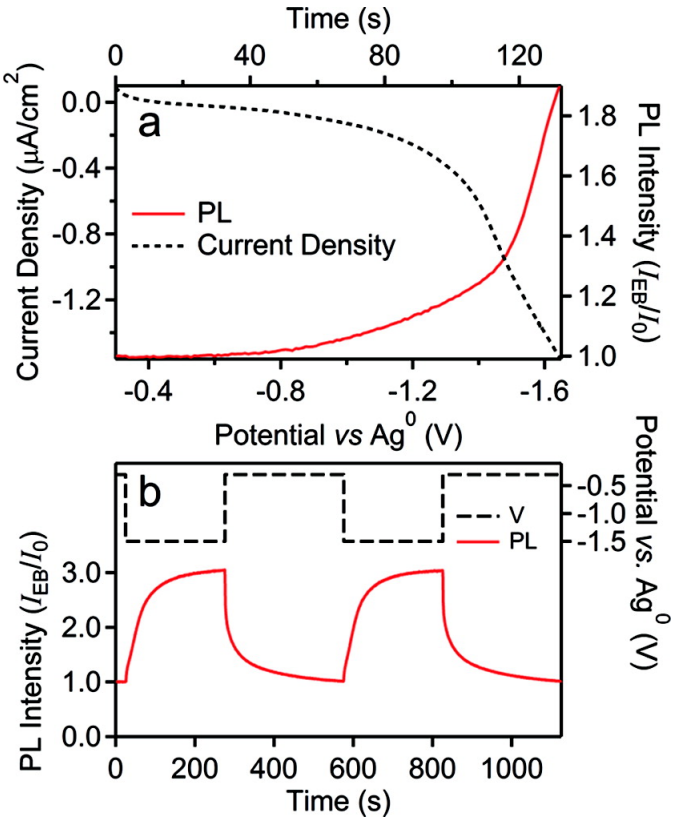

Figure 4.2: Electrobrightening of a Mn^{2+}:ZnSe QD film. **(a)** The current density (dashed) and the normalized PL intensity (solid) measured at 590 nm both increase as V_{app} is swept from -0.3 to -1.65 V at 0.01 V/s. **(b)** The normalized Mn^{2+} PL intensity (solid) and the applied potential *vs* Ag^0 (dashed) plotted versus time during a potential step experiment. λ_{ex} = 405 nm.

and the Mn^{2+} PL quantum yield increases to $\Phi \approx 29.5\%$ (solid curve), that is, $I_{EB}^{Mn}/I_0^{Mn} \approx 3$. The Mn^{2+}:ZnSe QDs thus show an order of magnitude smaller PL electrobrightening than observed in comparable ZnSe QDs. From over 25 different films prepared from four different QD syntheses, $I_{EB}^{Mn}/I_0^{Mn} \approx 2.5 \pm 0.5$ and $I_{EB}/I_0 \approx 40 \pm 10$. We note that conduction band filling in Mn^{2+}-doped CdS QDs yields exceptionally efficient Mn^{2+} PL quenching,[50] opposite from the PL enhancement observed here. Also noteworthy is the fact that the $Mn^{2+/+}$ potential resides > 1.5 eV above the ZnSe CB edge[62,63] and hence well outside the experimental potential window. These data thus support the interpretation that electrobrightening is linked to surface electron-trap passivation.

Figure 4.2a plots the Mn^{2+} PL intensity and the electrochemical current density measured si-

multaneously as a function of applied potential (V_{app}) for the Mn^{2+}:ZnSe QDs. As V_{app} becomes more negative, both the current density and the PL intensity increase in concert. The onset potential for charging is ~ -0.8 V *vs* Ag^0 below the potentials at which conduction band filling occurs in CdSe-based QDs (~ -1.0 V)[42] and CdS QDs (~ -1.3 V)[50] using similar electrochemical cells, and ~ -1.2 V below the potential for ZnSe QD conduction-band filling (~ -2.0 V *vs* Ag^0) estimated from the bulk offset potentials of CdSe, CdS, and ZnSe.[64,65] This observation and the correlation between charging and PL strongly support the interpretation that electron trap reduction increases PL intensities. Figure 4.2b plots the PL intensity *versus* time for a measurement in which the potential was alternated between V_{eq} (-0.3 V) and V_{app} (-1.5 V), as indicated by the dashed line. The electrobrightening is reversible, and in both directions, the PL reaches steady state slowly after a few hundred seconds. These kinetics are attributed to slow diffusion of charge carriers through the QD film. Previous work has demonstrated extremely low electron mobilities in QD films at potentials below the CB edge potential,[41,44,66,67] consistent with the added electrons occupying localized QD surface states. Importantly, the electrobrightening of Figure 4.2b appears to be accompanied by transfer of multiple electrons/QD, not just one or fewer. From the experimental coulometry and the number of QDs on the working electrode, a value of > 10 electrons/QD is estimated at $I_{EB}^{Mn}/I_0^{Mn} \approx 2.5 \pm 0.5$, albeit with sizable uncertainty (see Section 4.2). It is also interesting to note the inflections in both current density and PL at ~ -1.4 V, suggesting a rapidly changing trap density of states in that region.

Given that photoexcitation may itself induce PL brightening, it is necessary to address the dependence of this electrobrightening on photons. Figure 4.3 plots data intended to distinguish dark from photoinduced contributions to the electrobrightening shown in Figures 4.1 and 4.2. In these experiments, $V_{app} = -1.5$ V was applied at time = 0 with the QD film in the dark, and photons were turned on following a delay time ranging from 10 to 200 s. For comparison, the PL response obtained with continuous photoexcitation is also plotted. From these data, photoexcitation following application of a potential in the dark yields a large initial brightening followed by continued

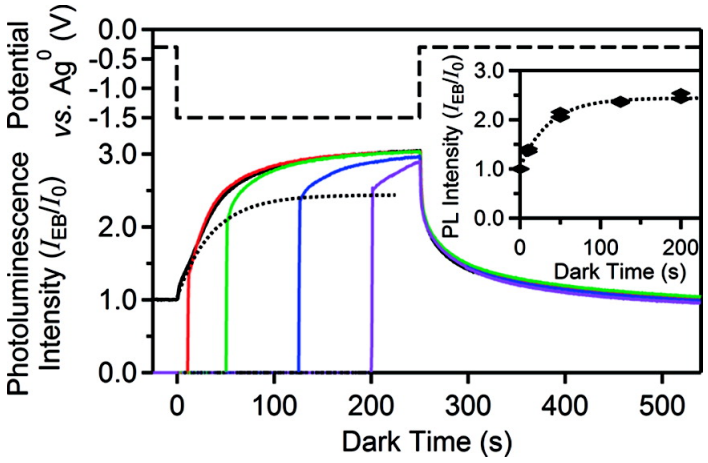

Figure 4.3: A cathodic bias ($V_{app} = -1.5$ V) is applied to a Mn^{2+}:ZnSe QD film for 250 s while the "dark time" is varied. The PL intensity at 590 nm *versus* time for dark periods of 0 s (black), 10 s (red), 50 s (green), 125 s (blue), and 200 s (purple), normalized at time = 0. An excitation power density of 150 mW/cm^2 (405 nm) was used. The dashed line represents the applied potential *vs* Ag^0 for all curves. **Inset:** The PL intensity at 590 nm measured within 1 s of photoexcitation, plotted *versus* dark time. The dotted curve shows a single-exponential fit to these data. This curve is reproduced in the main figure. λ_{ex} = 405 nm.

brightening on a much slower time scale. The magnitude of the initial brightening increases with increasing dark time (Figure 4.3, inset), converging to a value of ~ 2.5 times the PL intensity at V_{eq} with an apparent time constant of $\tau_{eff} \approx 36$ s. Because this time constant reports on a dark process that occurs prior to photoexcitation, it is interpreted as reflecting slow electron diffusion through the QD film without assistance from photons, which may relate to spectral diffusion of reducible traps (see Section 4.4).

The data in Figure 4.3 also show slow additional brightening after photoexcitation is initiated. To probe the role of photons more thoroughly, the dependence of electrobrightening on photoexcitation power density was investigated. Figure 4.4a shows electrobrightening results for the sample from Figure 4.3, measured as a function of time at various photon power densities and plotted as $\Delta I = I_{EB} - I_0$, where I_0 is the PL intensity at V_{eq}. Overall, the trend in ΔI is largely due to the trend in excitation power, with more PL at higher powers as expected. At all excitation powers, ΔI increases quickly after V_{app} is stepped to reducing potentials, followed by a slower increase

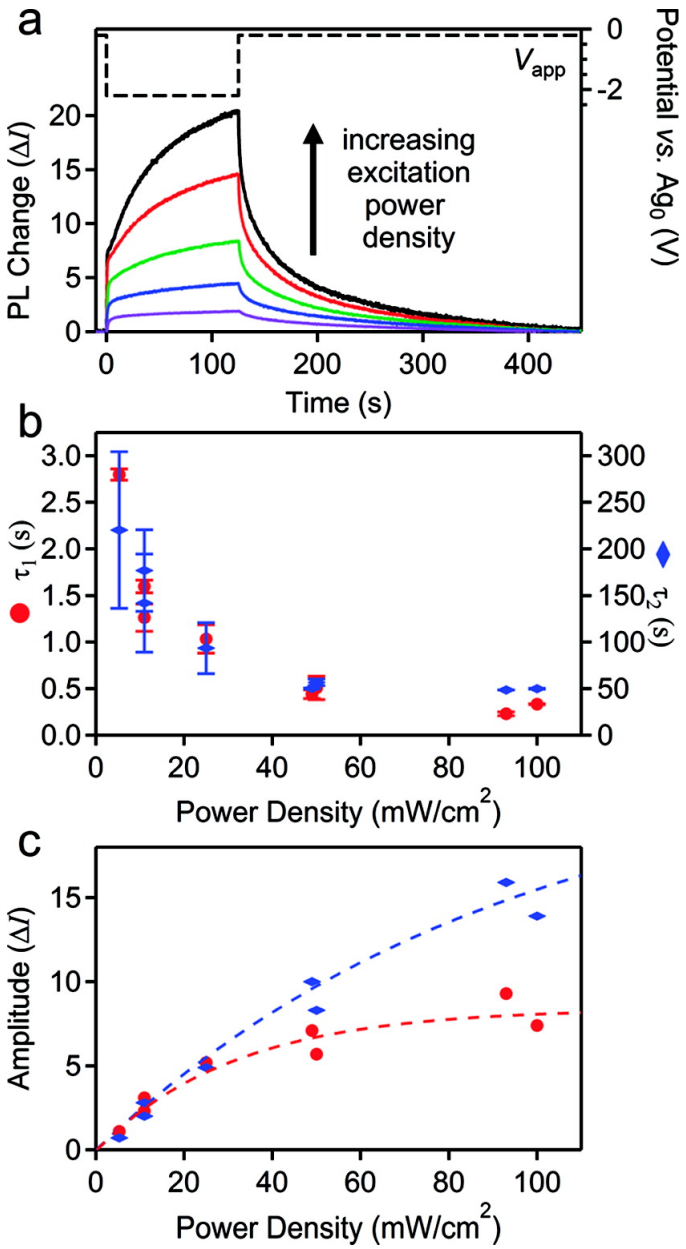

Figure 4.4: Dependence of PL electrobrightening on photoexcitation power density. **(a)** Change in Mn^{2+} PL intensity (ΔI) at 590 nm during electrobrightening measured at excitation power densities of 100, 50, 25, 11, and 5.3 mW/cm^2. The dashed line represents the cell potential *vs* Ag^0. (b) Time constants of the fast (τ_1) and slow (τ_2) contributions to the I_{EB}^{Mn} rise, plotted *versus* excitation power density. (c) Amplitudes of the fast (●) and slow (◆) components of the PL electrobrightening plotted *versus* excitation power density. The multiple data points represent results from independent measurements. The dashed curves are guides to the eye. λ_{ex} = 405 nm.

over the course of several minutes, and is describable using a double exponential function with apparent time constants τ_1 and τ_2 (see Appendix C). Both time constants decrease with increasing photoexcitation power density (Figure 4.4b). Figure 4.4c plots the amplitudes of the fast and slow electrobrightening components versus photoexcitation power density. Both amplitudes increase with increasing power density as expected, but both also show saturation at high powers. From the QD extinction coefficient at the excitation wavelength, the highest experimental power density (100 mW/cm^2) corresponds to a per-QD excitation rate of only ~ 285 s^{-1}, below where Mn^{2+} saturation occurs.

The observation of two components in the electrobrightening (Figure 4.4b,c) may reflect inhomogeneity in the contact between the QDs and the FTO. For example, QDs in direct contact with the FTO may participate in rapid electron transfer and hence show fast electrobrightening, whereas QDs separated from the FTO by additional QD layers may show electrobrightening that is subject to slow electron percolation. The excitation power dependence is very complex, however. Although additional experiments would be necessary to fully unravel this power dependence, it is clear that both components are accelerated by photons (Figure 4.4b), consistent with observations of photoconductivity in QD solids.[68] Not only does photoexcitation improve electron mobility, but it also introduces a photobias that allows additional charging of the QD film, increasing electrobrightening. From comparison of the photoassisted and dark electrobrightening magnitudes in Figure 4.3, $V_{\text{photobias}} \approx -0.1$ to -0.4 V at 100 mW/cm^2 excitation.

Figure 4.5 shows semilog plots of Mn^{2+} PL decay data measured at V_{eq}, at V_{app}, and after return to V_{eq}. The inset plots the electrobrightening in a potential step experiment as in Figure 4.2b. Although these are different samples, it is noteworthy that the electrobrightening is essentially indistinguishable with 360 nm (Figure 4.5) and 405 nm (Figure 4.2) excitation. The Mn^{2+} PL decay dynamics in these three measurements are superimposable when normalized at ~ 2.0 ms (see Appendix C), indicating that the Mn^{2+} excited state is unaffected by the applied potential. Instead, the cathodic bias leads to more Mn^{2+} excitation. This result confirms that electrobrightening

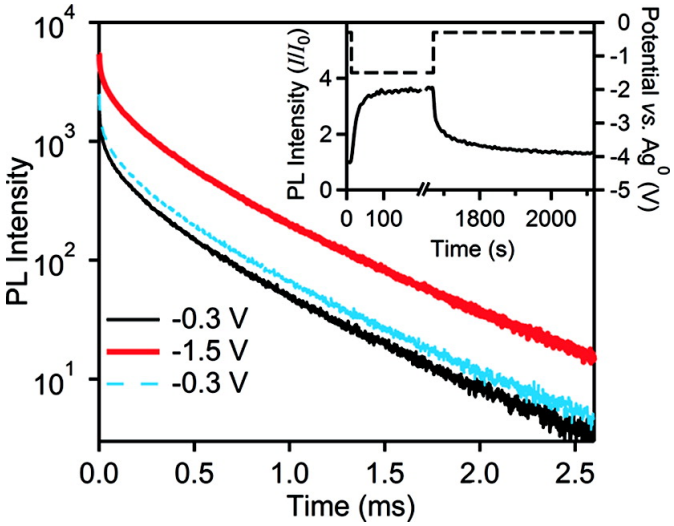

Figure 4.5: Mn^{2+} PL decay (590 nm) measured at various potentials for a film of Mn^{2+}:ZnSe QDs. The decay at $V_{eq} = -0.3$ V (black), $V_{app} = -1.5$ V (red, measured 190 s after V_{app}), and after the potential has been returned to $V_{eq} = -0.3$V (blue, measured 480 s after return to V_{eq}). **Inset:** Mn^{2+} PL intensity at 590 nm (solid), normalized at 0 s. The dashed line represents the cell potential *vs* Ag^0. λ_{ex} = 360 nm.

stems from elimination of exciton nonradiative decay pathways, which compete with the exciton-to-Mn^{2+} energy transfer. Exciton-to-Mn^{2+} energy transfer is extremely fast in these and related doped semiconductor nanocrystals, with typical rate constants of $k_{ET} \approx 10^{11}$ s^{-1},[57–60] and the data thus imply a similarly large rate constant for the relevant exciton nonradiative decay process that is eliminated under cathodic bias.

4.3.2 Kinetic Model

The electrobrightening data presented above can be understood using a simple kinetic model. Figure 4.6 depicts the decay pathways that are active following photoexcitation of ZnSe and Mn^{2+}:ZnSe QDs. In the ZnSe QDs, k_{PL} is the rate constant describing excitonic PL and has a value of $10^8 - 10^9$ s^{-1},[69] k_{t1} describes nonradiative relaxation *via* the set of electron traps that can be reduced at V_{app}, and k_{t2} describes nonradiative relaxation *via* traps that are inaccessible at V_{app} (*e.g.*, hole traps, or electron traps at too negative a potential). For the Mn^{2+}:ZnSe QDs, k_{ET} describes exciton-to-Mn^{2+} energy transfer and has a value of $\sim 10^{11}$ s^{-1}.[57–60] k_{Mn} describes

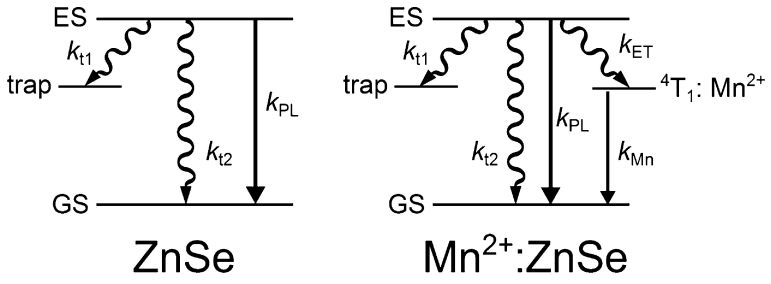

Figure 4.6: Depiction of the active relaxation pathways following photoexcitation of ZnSe and Mn^{2+}-doped ZnSe QDs. For ZnSe QDs, the photogenerated exciton can decay radiatively (k_{PL}), nonradiatively through an electron trap that is filled at V_{app} (k_{t1}), or nonradiatively through a trap that is unaffected by V_{app} (k_{t2}). For Mn^{2+}-doped ZnSe QDs, the exciton can additionally decay *via* energy transfer to Mn^{2+} (k_{ET}), which is followed by Mn^{2+} PL (k_{Mn}).

decay of the Mn^{2+} $^4T_1$ excited state. For simplicity, nonradiative $^4T_1$ decay is neglected, but the same conclusions are reached if it is treated explicitly. From these schemes, the observation that $I_{EB}/I_0 \approx 40$ for the ZnSe QDs whereas $I_{EB}^{Mn}/I_0^{Mn} \approx 3$ for the Mn^{2+}:ZnSe QDs can be attributed to the introduction of k_{ET} in the latter, as detailed below.

For the ZnSe QDs, the quantum yield for excitonic PL is given by eq 4.1.

$$\Phi_{PL}^{0} = \frac{k_{PL}}{k_{PL} + k_{t1} + k_{t2}} \tag{4.1}$$

The Mn^{2+} PL quantum yield in the Mn^{2+}:ZnSe QDs is governed by the energy transfer quantum efficiency (*i.e.*, the branching ratio of the exciton decay), as described by eq 4.2.

$$\Phi_{Mn}^{0} = \frac{k_{ET}}{k_{ET} + k_{PL} + k_{t1} + k_{t2}} \tag{4.2}$$

Under a cathodic bias of V_{app}, the accessible traps are reduced and $k_{t1} = 0$. The PL quantum yields for the ZnSe and Mn^{2+}:ZnSe QDs are then described by eqs 4.3 and 4.4, respectively.

$$\Phi_{PL}^{EB} = \frac{k_{PL}}{k_{PL} + k_{t2}} \tag{4.3}$$

$$\Phi_{\mathrm{Mn}}^{\mathrm{EB}} = \frac{k_{\mathrm{ET}}}{k_{\mathrm{ET}} + k_{\mathrm{PL}} + k_{\mathrm{t2}}} \tag{4.4}$$

Solving eq 1 for k_{t2}, substitution into eq 4.3, and rearrangement gives eq 4.5. Similarly, solving eq 4.2 for k_{t2} and substitution into eq 4.4 yields eq 4.6.

$$\frac{k_{\mathrm{t1}}}{k_{\mathrm{PL}}} = \frac{\Phi_{\mathrm{PL}}^{\mathrm{EB}} - \Phi_{\mathrm{PL}}^{0}}{\Phi_{\mathrm{PL}}^{\mathrm{EB}} \Phi_{\mathrm{PL}}^{0}} \tag{4.5}$$

$$\frac{k_{\mathrm{t1}}}{k_{\mathrm{ET}}} = \frac{\Phi_{\mathrm{Mn}}^{\mathrm{EB}} - \Phi_{\mathrm{Mn}}^{0}}{\Phi_{\mathrm{Mn}}^{\mathrm{EB}} \Phi_{\mathrm{Mn}}^{0}} \tag{4.6}$$

Equations 4.5 and 4.6 illustrate that large electrobrightening occurs when k_{t1} is large relative to the competing rate constant that leads to luminescence (k_{PL} in ZnSe QDs, and k_{ET} in Mn^{2+}:ZnSe QDs). The difference in electrobrightening between ZnSe and Mn^{2+}:ZnSe QDs is thus primarily due to the large difference between k_{ET} and k_{PL} ($\sim 10^{11}$ s^{-1} *vs* $\sim 10^{9}$ s^{-1}).

Experimentally, the electrobrightening ratios can be measured more reliably than absolute quantum yields. Recasting eq 4.6 solely in terms of electrobrightening ratios yields eq 7.

$$\frac{k_{\mathrm{t1}}}{k_{\mathrm{ET}}} = \frac{\left(I_{\mathrm{EB}}/I_0 - 1\right)\left(I_{\mathrm{EB}}^{\mathrm{Mn}}/I_0^{\mathrm{Mn}} - 1\right)}{I_{\mathrm{EB}}/I_0 - I_{\mathrm{EB}}^{\mathrm{Mn}}/I_0^{\mathrm{Mn}}} \tag{4.7}$$

From eq 7, it is evident that in the limit of small Mn^{2+}:ZnSe electrobrightening relative to ZnSe electrobrightening, $k_{\mathrm{t1}}/k_{\mathrm{ET}} \approx \left(I_{\mathrm{EB}}^{\mathrm{Mn}}/I_0^{\mathrm{Mn}} - 1\right)$. Inserting the experimental electrobrightening ratios from Figure 4.1 into eq 4.7 yields $k_{\mathrm{t1}} \approx 2k_{\mathrm{ET}}$, or also $\sim 10^{11}$ s^{-1}. Using the average electrobrightening ratios of all films of each given type yields $k_{\mathrm{t1}} \approx 1.5k_{\mathrm{ET}}$. Although any precise value of this ratio should be interpreted cautiously because of the arbitrariness of the potentials at which electrobrightening was measured, the fact that k_{t1} and k_{ET} are on the same order of magnitude allows the firm conclusions that (i) electron trapping is fast relative to excitonic PL in ZnSe QDs, and (ii) electrobrightening is suppressed by Mn^{2+} doping because energy transfer to Mn^{2+} is comparably

fast.

4.4 Discussion

The data presented here show that electrobrightening of QD photoluminescence can be large. By changing from CdSe (or other shallow-CB materials) to ZnSe, the CB potential is shifted ~ 1.0 V more negative, exposing many more electron traps within the semiconductor gap. ZnSe QDs are thus more susceptible to electron trapping than CdSe-based QDs, and hence also show more pronounced and recognizable electrobrightening.

The results here also relate to the proposed "B-type" blinking process deduced from recent single-particle spectroelectrochemical measurements on CdSe/CdS QDs.[51] In these studies, blinking could be suppressed by application of cathodic potentials below the band reduction potential, and hence was associated with surface electron traps. The data here indicate that trapping of photogenerated electrons is extremely fast in ZnSe QDs, and additionally that hot electrons are not integral to this process, as they are in CdSe/CdS QDs.[51] The very negative CB potentials of ZnSe QDs make electron trapping efficient even from the low-energy excitons generated by resonant excitation ($\lambda = 405$ nm, see Figure 4.2). This negative CB potential leads to much more pronounced electrobrightening in ZnSe QDs ($I_{EB}/I_0 \approx 50$) as compared to that estimated from the B-type blinking data of the CdSe/CdS QDs reported in ref 51 ($I_{EB}/I_0 \approx 4$), consistent with a greater density of reducible midgap traps in the ZnSe QDs. The data presented here are thus broadly consistent with the interpretation of electrochemically suppressed blinking proposed in ref 51.

Moreover, our data show that electrobrightening is due to addition of multiple electrons per ZnSe QD; that is, there must be several reducible midgap traps per QD. This observation is important because the reported B-type blinking is a binary phenomenon ("ON" and "OFF" states),[51] and the absence of intermediate PL therefore suggests that even just one active electron trap is sufficient to place a QD in its OFF state. These two considerations may be reconciled if the electron trap pop-

ulation is itself fluxional, for example, through interconversion between different surface ligation modes or related mechanisms of trap spectral diffusion.[70] In this scenario, traps would be electrochemically reduced when such fluctuations cause them to appear below V_{app}, and PL of a given QD would become progressively less intermittent as more traps are reduced. It should be noted that precisely the opposite effect (PL quenching) from surface trap filling has also been concluded from spectroelectrochemical studies of CdSe/CdS/ZnS nanocrystals,[46] which obviously cannot be due to the same mechanism as active in the electrobrightening reported here and therefore serves as a reminder of the diversity of QD surface chemistries.

This discussion highlights the fact that little is known about the microscopic identities of surface traps in colloidal QDs. Indeed, the microscopic origins of B-type *blinking* (*i.e.*, the actual cause of the transition between ON and OFF states in the absence of any applied potential) were not explicitly addressed in ref 51. Electron paramagnetic resonance spectroscopy (data not shown) rules out the presence of unpaired electrons at the surfaces of our ZnSe nanocrystals prior to electrochemical reduction, and simple one-electron reduction ("trap filling") of any lattice ion to generate a radical is unlikely. For example, the instability of CB electrons in ZnSe QDs is generally rationalized by comparison of the CB edge potential (~ -1.5 V *vs* SHE, pH 1) with the two-electron reduction of Zn^{2+} to Zn^0 (~ -0.8 V vs SHE, pH 1) because the one-electron reduction (Zn^{2+} to Zn^+) is unattainable. The relevant surface electrochemistry here likely entails reduction coupled with surface reconstruction involving exogenous ligands. At this time, however, these interesting microscopic issues remain unresolved. Nevertheless, the demonstration here of large electrobrightening in ZnSe QDs reveals a promising and accessible approach to characterization of redox-active surface traps in QDs, with important implications for improving our understanding and control of QD photophysics.

4.5 Summary

Large photoluminescence electrobrightening has been observed upon application of a cathodic bias to ZnSe and Mn^{2+}-doped ZnSe QD films in electrochemical cells. The electrobrightening is stable and reversible and can be augmented by photoassisted electrobrightening *via* a photobias effect. The electrobrightening is attributed to reductive passivation of surface traps at potentials well positive of the ZnSe conduction band potential. The magnitude of the electrobrightening reflects the kinetic competition in the excitonic excited state between electron trapping and processes leading to luminescence. In ZnSe QDs, electron trapping is much faster than radiative electron-hole recombination, and electrobrightening is large. In Mn^{2+}:ZnSe QDs, fast exciton-to-Mn^{2+} energy transfer competes effectively with electron trapping, and consequently the electrobrightening is smaller. These results complement recent observations of reduced blinking in single CdSe-based QDs under cathodic bias[49,51,52] by providing new insight into three aspects of electron-trap-mediated nonradiative decay: (i) electron trapping is fast ($k_{tr} \approx 10^{11}$ s^{-1} at V_{eq}); (ii) multiple electrons per QD are needed to suppress this nonradiative decay channel; and (iii) hot electrons are not integral to the electron-trapping mechanism (even though they may be in specific cases). Overall, the large electrobrightening observed here highlights the attractive possibilities that ZnSe and related semiconductor nanocrystals with very negative conduction-band potentials offer for investigating the trap-related photophysics and spectroelectrochemistry of colloidal QDs. By improving our understanding of how to control QD surface redox chemistries, such investigations may ultimately contribute to improvement of QD-based photovoltaics, light-emitting devices, and bioimaging technologies.

4.6 Notes to Chapter 4

[1] Nirmal, M.; Murray, C. B.; Bawendi, M. G. *Phys. Rev. B* **1994**, *50*, 2293–2300.

[2] Kuno, M.; Lee, J. K.; Dabbousi, B. O.; Mikulec, F. V.; Bawendi, M. G. *J. Chem. Phys.* **1997**, *106*, 9869–9882.

[3] Burda, C.; Link, S.; Mohamed, M.; El-Sayed, M. *J. Phys. Chem. B* **2001**, *105*, 12286–12292.

[4] Qu, L.; Peng, X. *J. Am. Chem. Soc.* **2002**, *124*, 2049–2055.

[5] Talapin, D. V.; Rogach, A. L.; Shevchenko, E. V.; Kornowski, A.; Haase, M.; Weller, H. *J. Am. Chem. Soc.* **2002**, *124*, 5782–5790.

[6] Kilina, S.; Ivanov, S.; Tretiak, S. *J. Am. Chem. Soc.* **2009**, *131*, 7717–7726.

[7] Wuister, S. F.; de Mello Donega, C.; Meijerink, A. *J. Phys. Chem. B* **2004**, *108*, 17393–17397.

[8] Kalyuzhny, G.; Murray, R. W. *J. Phys. Chem. B* **2005**, *109*, 7012–7021.

[9] Hines, M. A.; Guyot-Sionnest, P. *J. Phys. Chem.* **1996**, *100*, 468–471.

[10] Dabbousi, B. O.; Rodriguez-Viejo, J.; Mikulec, F. V.; Heine, J. R.; Mattoussi, H.; Ober, R.; Jensen, K. F.; Bawendi, M. G. *J. Phys. Chem. B* **1997**, *101*, 9463–9475.

[11] van Embden, J.; Jasieniak, J.; Gomez, D. E.; Mulvaney, P.; Giersig, M. *Aust. J. Chem.* **2007**, *60*, 457–471.

[12] Mahler, B.; Spinicelli, P.; Buil, S.; Quelin, X.; Hermier, J.-P.; Dubertret, B. *Nat. Mater.* **2008**, *7*, 659–664.

[13] Chen, Y.; Vela, J.; Htoon, H.; Casson, J. L.; Werder, D. J.; Bussian, D. A.; Klimov, V. I.; Hollingsworth, J. A. *J. Am. Chem. Soc.* **2008**, *130*, 5026–5027.

[14] Reiss, P.; ProtiÃšre, M.; Li, L. *Small* **2009**, *5*, 154–168.

[15] Wang, X.; Ren, X.; Kahen, K.; Hahn, M. A.; Rajeswaran, M.; Maccagnano-Zacher, S.; Silcox, J.; Cragg, G. E.; Efros, A. L.; Krauss, T. D. *Nature* **2009**, *459*, 686.

[16] Nazzal, A. Y.; Wang, X.; Qu, L.; Yu, W.; Wang, Y.; Peng, X.; Xiao, M. *J. Phys. Chem. B* **2004**, *108*, 5507–5515.

[17] Jasieniak, J.; Mulvaney, P. *J. Am. Chem. Soc.* **2007**, *129*, 2841–2848.

[18] Lee, D., Steven F.; Osborne, D., Mark A. *ChemPhysChem* **2009**, *10*, 2174–2191.

[19] Hess, B. C.; Okhrimenko, I. G.; Davis, R. C.; Stevens, B. C.; Schulzke, Q. A.; Wright, K. C.; Bass, C. D.; Evans, C. D.; Summers, S. L. *Phys. Rev. Lett.* **2001**, *86*, 3132.

[20] Manna, L.; Scher, E. C.; Li, L.-S.; Alivisatos, A. P. *J. Am. Chem. Soc.* **2002**, *124*, 7136–7145.

[21] Jones, M.; Nedeljkovic, J.; Ellingson, R. J.; Nozik, A. J.; Rumbles, G. *J. Phys. Chem. B* **2003**, *107*, 11346–11352.

[22] Wang, Y.; Tang, Z.; Correa-Duarte, M. A.; Pastoriza-Santos, I.; Giersig, M.; Kotov, N. A.; Liz-Marzan, L. M. *J. Phys. Chem. B* **2004**, *108*, 15461–15469.

[23] Asami, H.; Abe, Y.; Ohtsu, T.; Kamiya, I.; Hara, M. *J. Phys. Chem. B* **2003**, *107*, 12566–12568.

[24] Cordero, S. R.; Carson, P. J.; Estabrook, R. A.; Strouse, G. F.; Buratto, S. K. *J. Phys. Chem. B* **2000**, *104*, 12137–12142.

[25] Simurda, M.; Nemec, P.; Trojnek, F.; Mal, P. *Thin Solid Films* **2004**, *453-454*, 300–303.

[26] Oda, M.; Hasegawa, A.; Iwami, N.; Nishiura, K.; Ando, N.; Nishiyama, A.; Horiuchi, H.; Tani, T. *J. Lumin.* **2007**, *127*, 198–203.

[27] Maenosono, S. *Chem. Phys. Lett.* **2003**, *376*, 666–670.

[28] Kimura, J.; Uematsu, T.; Maenosono, S.; Yamaguchi, Y. *J. Phys. Chem. B* **2004**, *108*, 13258–13264.

[29] Tice, D. B.; Frederick, M. T.; Chang, R. P. H.; Weiss, E. A. *J. Phys. Chem. C* **2011**, *115*, 3654–3662.

[30] Duncan, T. V.; Polanco, M. A. M.; Kim, Y.; Park, S.-J. *J. Phys. Chem. C* **2009**, *113*, 7561–7566.

[31] Schafer, S.; Wang, Z.; Kipp, T.; Mews, A. *Phys. Rev. Lett.* **2011**, *107*, 137403.

[32] Hoyer, P.; Weller, H. *J. Phys. Chem.* **1995**, *99*, 14096–14100.

[33] Shim, M.; Guyot-Sionnest, P. *Nature* **2000**, *407*, 981–983.

[34] Shim, M.; Wang, C.; Guyot-Sionnest, P. *J. Phys. Chem. B* **2001**, *105*, 2369–2373.

[35] Wang, C.; Shim, M.; Guyot-Sionnest, P. *Science* **2001**, *291*, 2390–2392.

[36] Haram, S. K.; Quinn, B. M.; Bard, A. J. *J. Am. Chem. Soc.* **2001**, *123*, 8860–8861.

[37] Alperson, B.; Rubinstein, I.; Hodes, G. *Phys. Rev. B* **2001**, *63*, 081303.

[38] Wang, C.; Shim, M.; Guyot-Sionnest, P. *Appl. Phys. Lett.* **2002**, *80*, 4–6.

[39] Roest, A. L.; Kelly, J. J.; Vanmaekelbergh, D.; Meulenkamp, E. A. *Phys. Rev. Lett.* **2002**, *89*, 036801.

[40] Wehrenberg, B. L.; Guyot-Sionnest, P. *J. Am. Chem. Soc.* **2003**, *125*, 7806–7807.

[41] Yu, D.; Wang, C.; Guyot-Sionnest, P. *Science* **2003**, *300*, 1277–1280.

[42] Guyot-Sionnest, P.; Wang, C. *J. Phys. Chem. B* **2003**, *107*, 7355–7359.

[43] Wang, C.; Wehrenberg, B. L.; Woo, C. Y.; Guyot-Sionnest, P. *J. Phys. Chem. B* **2004**, *108*, 9027–9031.

[44] Yu, D.; Wehrenberg, B. L.; Jha, P.; Ma, J.; Guyot-Sionnest, P. *J. Appl. Phys.* **2006**, *99*, 104315.

[45] Jha, P. P.; Guyot-Sionnest, P. *J. Phys. Chem. C* **2007**, *111*, 15440–15445.

[46] Gooding, A. K.; Gomez, D. E.; Mulvaney, P. *ACS Nano* **2008**, *2*, 669–676.

[47] Jha, P. P.; Guyot-Sionnest, P. *ACS Nano* **2009**, *3*, 1011–1015.

[48] Araci, Z. O.; Shallcross, C. R.; Armstrong, N. R.; Saavedra, S. S. *J. Phys. Chem. Lett.* **2010**, *1*, 1900–1905.

[49] Jha, P. P.; Guyot-Sionnest, P. *J. Phys. Chem. C* **2010**, *114*, 21138–21141.

[50] White, M. A.; Weaver, A. L.; Beaulac, R.; Gamelin, D. R. *ACS Nano* **2011**, *5*, 4158–4168.

[51] Galland, C.; Ghosh, Y.; Steinbeck, A.; Sykora, M.; Hollingsworth, J. A.; Klimov, V. I.; Htoon, H. *Nature* **2011**, *479*, 203–207.

[52] Qin, W.; Shah, R. A.; Guyot-Sionnest, P. *ACS Nano* **2012**, *6*, 912–918.

[53] Archer, P. I.; Santangelo, S. A.; Gamelin, D. R. *J. Am. Chem. Soc.* **2007**, *129*, 9808–9818.

[54] Li, L. S.; Pradhan, N.; Wang, Y.; Peng, X. *Nano Lett.* **2004**, *4*, 2261–2264.

[55] Norberg, N. S.; Parks, G. L.; Salley, G. M.; Gamelin, D. R. *J. Am. Chem. Soc.* **2006**, *128*, 13195–13203.

[56] Houtepen, A. J.; Vanmaekelbergh, D. *J. Phys. Chem. B* **2005**, *109*, 19634–19642.

[57] Shibata, K.; Nakayama, E.; Souma, I.; Murayama, A.; Oka, Y. *Phys. Status Solidi B* **2002**, *229*, 473–476.

[58] Seufert, J.; Bacher, G.; Scheibner, M.; Forchel, A.; Lee, S.; Dobrowolska, M.; Furdyna, J. K. *Phys. Rev. Lett.* **2002**, *88*, 027402.

[59] Chen, H.-Y.; Chen, T.-Y.; Son, D. H. *J. Phys. Chem. C* **2010**, *114*, 4418–4423.

[60] Vlaskin, V. A.; Janssen, N.; van Rijssel, J.; Beaulac, R.; Gamelin, D. R. *Nano Lett.* **2010**, *10*, 3670–3674.

[61] Beaulac, R.; Ochsenbein, S. T.; Gamelin, D. R. In *Nanocrystal Quantum Dots*, 2nd ed.; Klimov, V. I., Ed.; Taylor & Francis: London, 2010.

[62] Beaulac, R.; Gamelin, D. R. *Phys. Rev. B* **2010**, *82*, 224401.

[63] Beaulac, R.; Feng, Y.; May, J. W.; Badaeva, E.; Gamelin, D. R.; Li, X. *Phys. Rev. B* **2011**, *84*, 195324.

[64] Madelung, O. *Semiconductors: Data Handbook*, 3rd ed.; Springer:Berlin, 2004.

[65] Wei, S.-H.; Zunger, A. *Appl. Phys. Lett.* **1998**, *72*, 2011–2013.

[66] Vanmaekelbergh, D.; Liljeroth, P. *Chem. Soc. Rev.* **2005**, *34*, 299–312.

[67] Liu, Y.; Gibbs, M.; Puthussery, J.; Gaik, S.; Ihly, R.; Hillhouse, H. W.; Law, M. *Nano Lett.* **2010**, *10*, 1960–1969.

[68] Leatherdale, C. A.; Kagan, C. R.; Morgan, N. Y.; Empedocles, S. A.; Kastner, M. A.; Bawendi, M. G. *Phys. Rev. B* **2000**, *62*, 2669.

[69] Balet, L. P.; Ivanov, S. A.; Piryatinski, A.; Achermann, M.; Klimov, V. I. *Nano Lett.* **2004**, *4*, 1485–1488.

[70] Frantsuzov, P.; Kuno, M.; Janko, B.; Marcus, R. A. *Nat. Phys.* **2008**, *4*, 519–522.

Chapter 5

Redox Brightening of Colloidal Semiconductor Nanocrystals using Molecular Reductants

Chemical reductants of sub-conduction-band potentials are demonstrated to induce large photoluminescence enhancement in colloidal ZnSe-based nanocrystals. The photoluminescence quantum yield of colloidal Mn^{2+}-doped ZnSe nanocrystals has been improved from 14% to 80% simply by addition of an outer-sphere reductant. Up to 48-fold redox brightening is observed for nanocrystals with lower starting quantum yields. These increases are quickly reversed upon exposure to air and are temporary even under anaerobic conditions. This redox brightening process offers a new and systematic approach to understanding redox-active surface "trap states" and their contributions to the physical properties of colloidal semiconductor nanocrystals. The work in this chapter is reprinted with permission from Rinehart, J. D., Weaver, A. L., Gamelin, D. R. *J. Am. Chem. Soc.*, **2012**, *134*, 16175-16177. Copyright 2012 American Chemical Society.

5.1 Introduction

The redox chemistries of colloidal semiconductor nanocrystals (NCs, or quantum dots, QDs) remain relatively unexplored. Many studies have focused on the challenges of introducing and

characterizing extra delocalized bandlike charge carriers.[1–4] Nanocrystal surfaces are also often redox-active, but surface "traps" have proven difficult to characterize despite their ability to influence many physical properties of the target QDs. For example, midgap surface traps can strongly suppress the excitonic photoluminescence (PL) of colloidal QDs[5–11] or compromise the transport properties of QD solids.[12] Controlling such traps thus represents a long-standing challenge in nanocrystal research. The most successful routes to surface-trap passivation have involved shell growth to provide spatial separation of the carriers from the surface[6,11,13–15] without necessarily eliminating the traps themselves. In some cases, binding of electron-rich ligands appears to have enhanced the ensemble PL and reduced single-particle blinking.[16–21] Electrochemical measurements on single CdSe based nanocrystals on electrode surfaces have demonstrated reduced blinking under cathodic bias, attributed to electron trap filling.[22–24] We recently reported the reversible electrochemical passivation of electron traps in wide-gap ZnSe and Mn^{2+}-doped ZnSe (Mn^{2+}:ZnSe) NC films, which yielded strongly enhanced ensemble PL ("electrobrightening").[25] As in the blinking studies, the microscopic origins of this brightening remain unclear, and in particular, it is important to determine whether this phenomenon is limited to NCs on electrode surfaces or if it is truly a property of the freestanding colloidal NCs.

Redox passivation of the surface traps of colloidal QDs would address this ambiguity and perhaps facilitate identification of the microscopic origins of this brightening by enabling chemical analysis of the redox-active traps themselves using techniques that are incompatible with electrode surfaces. Electrochemistry on the freestanding colloidal QDs poses several daunting challenges, however, including the lack of a uniform potential throughout the solution and diffusive reoxidation at the counter electrode. Such challenges can be circumvented using a purely chemical approach. Here we demonstrate large increases in the PL quantum yields of colloidal Mn^{2+}:ZnSe NCs through the controlled addition of midgap electrons *via* molecular electron shuttles. Mn^{2+}:ZnSe NCs are described here for practical reasons, because the large energy shift between absorption and PL facilitates the measurements, but the underlying electron trapping phenomenon is the same

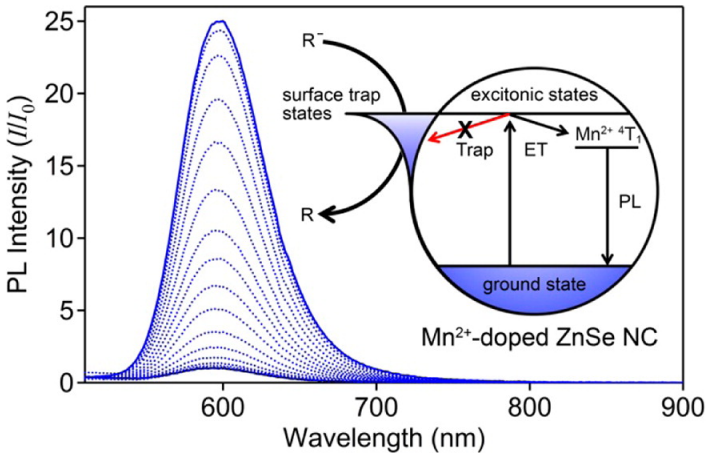

Figure 5.1: PL increase due to reductive passivation of surface traps in 0.6% Mn^{2+}:ZnSe nanocrystals (1.3×10^{-6} M; d = 4.6 nm) under 405 nm excitation. PL intensities (I) are normalized to the original intensity (I_0). **Inset:** schematic of the redox process leading to PL enhancement. R is a reductant. Arrows illustrate nonradiative electron trapping (Trap) and energy transfer (ET) from the exciton to excite Mn^{2+}: into its $^4T_1$ state, from which the PL occurs.

for undoped ZnSe NCs.[25]

5.2 Results & Discussion

Colloidal trioctylphosphine oxide (TOPO)-capped Mn^{2+}:ZnSe NCs were prepared as described previously (see Appendix D). To study traps, our first experiments were performed on NCs with deliberately small PL quantum yields ($\phi = 0.4\%$). Initial attempts at reductive passivation of the surface traps on these NCs involved the addition of sodium-potassium alloy (NaK_2) to stirred 1.3×10^{-6} M NC suspensions in tetrahydrofuran (THF) under an inert atmosphere. The addition of NaK_2 indeed induced PL brightening (Figure 5.1), but only after a long ($\sim$ 1 h) induction period. After a maximum of $\sim$ 25-fold brightening was reached, the NCs slowly precipitated, and the PL was eventually lost (Figure 5.2). To improve the reduction kinetics, 2,2´-bipyridine (bpy) was introduced as a molecular electron shuttle. This addition not only caused a 6-fold acceleration of the brightening but also yielded a $\sim$ 2-fold increase in the maximum PL relative to NaK_2 alone. As with the NaK_2 reaction, the PL of these NCs was not stable, and slowly decreased again after

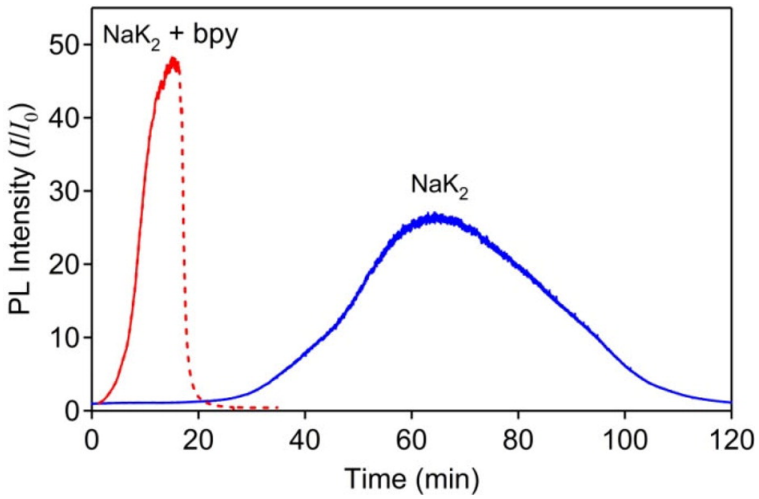

Figure 5.2: Traces of the time evolution of the chemical brightening for colloidal Mn^{2+}:ZnSe nanocrystals (1.3×10^{-6} M; d = 4.6 nm) with NaK_2 (blue) or NaK_2 plus 2,2´-bipyridine (red). The PL intensity (I) is plotted in terms of multiples of the original intensity (I_0). Exposure to air rapidly reverses the PL brightening (dashed).

reaching maximum brightening, although the PL change became difficult to monitor because of absorption at the same energies from accumulating bpy radical (data not shown). Exposing the brightened solution to ambient atmosphere resulted in rapid PL loss (Figure 5.2), confirming the redox nature of the transformation. These results demonstrate the importance of reducible surface states in free-standing colloidal NCs as well as the concept of targeted chemical delivery of redox equivalents to the surfaces of such NCs.

Electrochemical studies of Mn^{2+}:ZnSe NC films showed reduction starting as low as $\sim$ 1.2 V below the conduction-band minimum and increasing gradually at more cathodic potentials, suggesting broadly distributed surface-state potentials.[25] To probe the distribution of traps in the colloidal NCs, electrons were titrated into stirring solutions of Mn^{2+}:ZnSe NCs using molecular reductants with different redox potentials. Titration of bis(cyclopentadienyl)cobalt(II) [cobaltocene, -1.3 V *vs* the ferrocene (Fc)/ferrocenium (Fc^+) couple[26]]* led to escalating PL before eventual saturation at $\sim$ 10-fold brightening (to $\phi_{max} = 4\%$) with $\sim$ 350 equiv. We hypothesized that the

*All potentials quoted are for glyme solutions. Significant variation is not expected for the THF solutions used in the present work.

smaller brightening here compared with Figure 5.2 is related to the fact that the redox potential of cobaltocene is insufficient to reduce some surface traps. This hypothesis was confirmed by switching to anthracene radical as the reductant,[†] which has a redox potential of -2.5 V vs Fc/Fc^+.[26] For up to ~ 225 equiv, anthracene radical induced an almost identical 4-fold PL brightening as cobaltocene (Figure 5.3). Beyond this amount, however, anthracene radical addition accelerated the PL brightening relative to cobaltocene, eventually maximizing at a ~ 33-fold increase (to $\phi_{max} = 13\%$) with ~ 400 equiv of reductant. These results demonstrate that the potential of the supplied electron dictates the magnitude of the PL enhancement, thereby implicating a broad distribution of reducible trap potentials in these colloidal NCs. The absence of any detectable changes in the absorption spectra during the course of these experiments (Figure D.1 in Appendix D) eliminated nanocrystal etching, growth, or conduction-band filling as possible origins of the redox brightening. In contrast with the NCs subjected to a continuous source of reductant (Figure 5.2), NCs reduced by titration remained stable against precipitation, indicating that the effectively unlimited reducing capacity of the vast excess of NaK_2 used for Figure 5.2 caused the NC precipitation.

Interestingly, the saturation of the redox brightening in Figure 5.3 occurred at reductant:NC ratios of at least 300:1 (*i.e.*, a large excess of reductant). The contrast between the extent of reductant required here and that estimated for QD electrobrightening [$I/I_0(\text{max})$ at greater than ~ 10 electrons/NC][25] may reflect either the importance of increased surface area and ligand mobility in colloidal suspensions or the difference between stoichiometric and steady-state reducing conditions. Moreover, brightening occurred only following what resembled an induction stage, where initial reductant aliquots produced less PL increase than later aliquots. These results could indicate that impurities (e.g., trace O_2, water, or excess NC ligand) intercepted some of the reducing equivalents. Alternatively, they could reflect a large surface capacitance and a nonlinear PL response to progressive trap passivation. To test the possibility that this induction period was somehow related to the small initial PL quantum yields of these NCs, experiments were next performed using NCs

[†]The anthracene radical was generated by NaK_2 reduction of anthracene in THF.

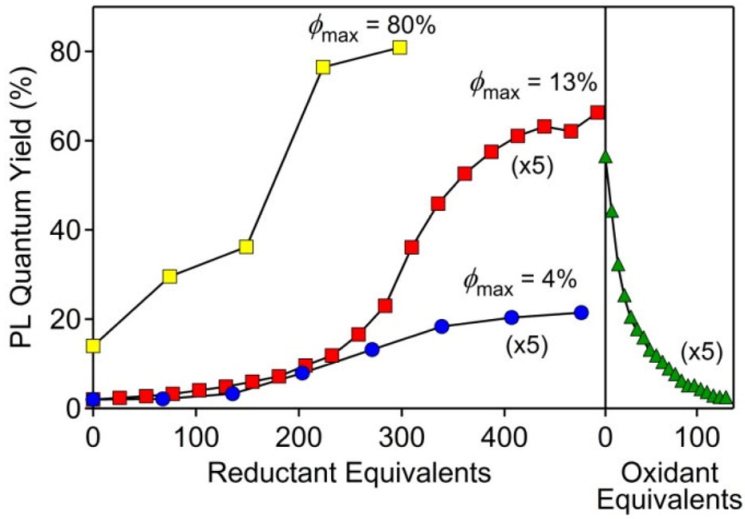

Figure 5.3: Changes in Mn^{2+} $^4T_1 \rightarrow {}^6A_1$ PL quantum yield in colloidal Mn^{2+}:ZnSe NCs (2.6×10^{-7} M; d = 4.6 nm) *vs* equivalents of reductant or oxidant. Data for reduction of as-prepared NCs by cobaltocene (blue ● [$\phi_{initial} = 0.4\%$]) and anthracene radical (red ■ [$\phi_{initial} = 0.4\%$] and yellow ■ [$\phi_{initial} = 14\%$]) and for oxidation of maximally brightened NCs by BAHA (green ▲) are shown. The data for NCs with initial quantum yields of 0.4% have been multiplied by 5 for clarity.

with larger initial quantum yields (d = 3.8 nm, 1% Mn^{2+}; $\phi = 14\%$). Redox-brightening data collected using anthracene radical as the reductant are included in Figure 3. Not only was less reductant needed to achieve maximum brightening ($\phi_{max} = 80\%$ at $\sim$ 300 electrons/NC, I/I_0 = 5.7), but the data also no longer showed a similar induction stage before the PL increased. The two experiments were performed under essentially identical conditions, arguing against attribution of the induction stage in the low-quantum-yield NCs to spurious oxidants. Instead, the data suggest that reduction of the deepest traps occurs without significant PL improvement. The nonlinear PL response to added reducing equivalents is thus consistent with the conclusion that the largest PL increase per added electron comes when the number of remaining traps is smallest (Figure D.2).

As an independent test, the outer-sphere one-electron oxidant tris(4-bromophenyl)aminium hexachloroantimonate (BAHA) was titrated against a reductively brightened colloidal suspension of the low-quantum-yield Mn^{2+}:ZnSe NCs used in Figure 5.2. The NC PL approached its initial value upon removal of $\sim$ 100 electrons/NC (Figure 5.3, right), $\sim$ 4 times fewer electrons than had

been added but comparable to the number of electrons needed to span the same range of PL intensities in the other direction. These data are consistent with the conclusion that the low-quantum-yield reductive brightening shown in Figure 5.3 involves at least 100 reduction events per NC. Although this number appears to be large, it is comparable to the number of unpassivated surface sites estimated for these NCs, or the number of coordinating ligands. For a d = 4.6 nm NC, approximately one-quarter of the ZnSe is at the surface, which would correspond to $\sim$ 250 ZnSe units. Typical packing densities of TOPO may provide $\sim$ 30% surface coverage,[17] meaning $\sim$ 75 surfactant ligands and $\sim$ 175 unpassivated surface binding sites would be present [*i.e.*, sufficient capacity to accommodate the electrons provided by the chemical reductants plus cations (*e.g.*, Na^+ or K^+) to compensate for the additional charge]. Regardless of the precise numbers, well beyond stoichiometric quantities of reductant are required for maximum redox brightening of both the low- and high- quantum-yield NCs.

In all of the samples, the PL decreased slowly after reductive brightening (Figure D.2), possibly because of the slow introduction of adventitious oxygen or interactions of the reduced NCs with other molecules in solution. This PL decrease was greatly accelerated by air (Figure 5.2), demonstrating that reductive trap passivation under these conditions is easily reversed by exposure to oxidants. Whereas surface-trap reduction can form high-quantum-yield ZnSe-based NCs, stabilization of these high quantum yields must be accomplished by independent means. Such experiments are presently underway.

5.3 Summary

The results presented here demonstrate redox brightening of freestanding colloidal Mn^{2+}:ZnSe NCs *via* the addition of noncoordinating molecular reductants. The potential of the reductant determines the extent of redox brightening. Titration showed that the brightening is associated with multiple reducing equivalents per NC, which can be rationalized by consideration of the large

surface-to-volume ratios and imperfect surface passivation of these NCs. These results highlight the importance of surface electron traps in the PL of colloidal ZnSe-based NCs. Understanding the microscopic origins of redox brightening in this model system will be generally informative because of the paucity of molecular-level information about surface traps and may enable extension to other related NCs where redox-active surfaces inhibit performance. Future experiments will therefore focus on characterizing the microscopic identities of the redox-active traps and on the development of chemical methods for making this brightening robust against reversal by air.

5.4 Notes to Chapter 5

[1] Shim, M.; Guyot-Sionnest, P. *Nature* **2000**, *407*, 981–983.

[2] Shim, M.; Wang, C.; Guyot-Sionnest, P. *J. Phys. Chem. B* **2001**, *105*, 2369–2373.

[3] Liu, W. K.; Whitaker, K. M.; Smith, A. L.; Kittilstved, K. R.; Robinson, B. H.; Gamelin, D. R. *Phys. Rev. Lett.* **2007**, *98*, 186804.

[4] Whitaker, K. M.; Ochsenbein, S. T.; Polinger, V. Z.; Gamelin, D. R. *J. Phys. Chem. C* **2008**, *112*, 14331–14335.

[5] Nirmal, M.; Murray, C. B.; Bawendi, M. G. *Phys. Rev. B* **1994**, *50*, 2293–2300.

[6] Hines, M. A.; Guyot-Sionnest, P. *J. Phys. Chem.* **1996**, *100*, 468–471.

[7] Kuno, M.; Lee, J. K.; Dabbousi, B. O.; Mikulec, F. V.; Bawendi, M. G. *J. Chem. Phys.* **1997**, *106*, 9869–9882.

[8] Burda, C.; Link, S.; Mohamed, M.; El-Sayed, M. *J. Phys. Chem. B* **2001**, *105*, 12286–12292.

[9] Wuister, S. F.; de Mello Donega, C.; Meijerink, A. *J. Phys. Chem. B* **2004**, *108*, 17393–17397.

[10] Kalyuzhny, G.; Murray, R. W. *J. Phys. Chem. B* **2005**, *109*, 7012–7021.

[11] Chen, Y.; Vela, J.; Htoon, H.; Casson, J. L.; Werder, D. J.; Bussian, D. A.; Klimov, V. I.; Hollingsworth, J. A. *J. Am. Chem. Soc.* **2008**, *130*, 5026–5027.

[12] Geyer, S.; Porter, V. J.; Halpert, J. E.; Mentzel, T. S.; Kastner, M. A.; Bawendi, M. G. *Phys. Rev. B* **2010**, *82*, 155201–.

[13] Dabbousi, B. O.; Rodriguez-Viejo, J.; Mikulec, F. V.; Heine, J. R.; Mattoussi, H.; Ober, R.; Jensen, K. F.; Bawendi, M. G. *J. Phys. Chem. B* **1997**, *101*, 9463–9475.

[14] Mahler, B.; Spinicelli, P.; Buil, S.; Quelin, X.; Hermier, J.-P.; Dubertret, B. *Nat. Mater.* **2008**, *7*, 659–664.

[15] Wang, X.; Ren, X.; Kahen, K.; Hahn, M. A.; Rajeswaran, M.; Maccagnano-Zacher, S.; Silcox, J.; Cragg, G. E.; Efros, A. L.; Krauss, T. D. *Nature* **2009**, *459*, 686.

[16] Qu, L.; Peng, X. *J. Am. Chem. Soc.* **2002**, *124*, 2049–2055.

[17] Bullen, C.; Mulvaney, P. *Langmuir* **2006**, *22*, 3007–3013.

[18] Jasieniak, J.; Mulvaney, P. *J. Am. Chem. Soc.* **2007**, *129*, 2841–2848.

[19] Munro, A. M.; Plante, I. J.-L.; Ng, M. S.; Ginger, D. S. *J. Phys. Chem. C* **2007**, *111*, 6220–6227.

[20] Duncan, T. V.; Polanco, M. A. M.; Kim, Y.; Park, S.-J. *J. Phys. Chem. C* **2009**, *113*, 7561–7566.

[21] Evans, C. M.; Cass, L. C.; Knowles, K. E.; Tice, D. B.; Chang, R. P.; Weiss, E. A. *J. Coord. Chem.* **2012**, *65*, 2391–2414.

[22] Jha, P. P.; Guyot-Sionnest, P. *J. Phys. Chem. C* **2010**, *114*, 21138–21141.

[23] Galland, C.; Ghosh, Y.; Steinbeck, A.; Sykora, M.; Hollingsworth, J. A.; Klimov, V. I.; Htoon, H. *Nature* **2011**, *479*, 203–207.

[24] Qin, W.; Shah, R. A.; Guyot-Sionnest, P. *ACS Nano* **2012**, *6*, 912–918.

[25] Weaver, A. L.; Gamelin, D. R. *J. Am. Chem. Soc.* **2012**, *134*, 6819–6825.

[26] Connelly, N. G.; Geiger, W. E. *Chem. Rev.* **1996**, *96*, 877–910.

Chapter 6

Summary and Outlook

6.1 Summary

The previous chapters have addressed the role of electronic doping and trap reduction in undoped and Mn^{2+}-doped chalcogenide quantum dots.

Chapter 2 explored the e^-_{CB}-Mn^{2+} exchange interaction in Mn^{2+}-doped CdS QDs and its effect on Mn^{2+} PL. Spectroelectrochemical measurements were used to study the absorption and photoluminescence changes upon electron injection into a Mn^{2+}:CdS QD film. The investigation revealed a Mn-Auger de-excitation pathway (with $k_{Aug} \approx 0.2 \times 10^{10}$ $s^{-1}(e^-/QD)^{-1}$) that was more effective at quenching photoluminescence than the comparative trion Auger pathway in undoped QDs. It was determined that the relatively long lifetime of the Mn^{2+} excited state allows for deactivation of numerous excited QDs with just one electron. Additionally, it was proposed that the hybridization between the empty Mn^{2+}(4s) orbital and the CB-edge plus a large density of e^-_{CB} excited states ~ 2.1 eV above the $1S_e$ state facilitate *s-d* exchange and are related to k_{Aug}.

Chapter 3 examined photochemical electronic doping of colloidal CdSe nanocrystals with a borohydride hole quencher, Li[Et_3BH]. Previously, photochemical methods of charging were used with oxide QDs, but the shallow valence bands of chalcogenide QDs were not reactive with the

common hole quenchers used with oxides. Li[Et_3BH] provides a facile and reversible method for forming stable *n*-type CdSe QDs while also eliminating the surface degradation usually caused by chemical reductants. Chemical titrations with an oxidant confirmed electron accumulation in the QDs and suggested that for some samples many electrons were trapped at the surface.

Chapter 4 investigated the role of electron traps during charge injection. For this study, a wide bandgap semiconductor material (ZnSe) was chosen to allow specific targeting of electron traps within the semiconductor bandgap. Spectroelectrochemical studies monitored the charge injection in a QD film through voltammetric analysis with correlation to the changes in photoluminescence intensity. It was shown that enhancement of the QD PL was directly related to electron injection into the QD film. Both undoped and Mn^{2+}-doped ZnSe exhibited this electrobrightening behavior, but it was more pronounced in the undoped samples. By comparison of the various relaxation pathways in the undoped and Mn^{2+}-doped QDs to experimentally determined quantum yields, it was proposed that electron trapping (k_{t1}) is competitive with energy transfer to the Mn^{2+}excited state (k_{ET}) with $k_{t1} \approx 2k_{ET}$. Hence, in undoped QDs the brightening is more pronounced since the much slower excitonic emission (k_{PL}) is now the competing relaxation pathway.

Chapter 5 explored an extension of the electrobrightening from Chapter 4 by moving to colloidal suspensions of Mn^{2+}-doped ZnSe QDs and using chemical reductants. The redox-active surface sites on the QDs were easily reduced with biphenyl and anthracene radical, yielding impressive QY enhancement from 14% - 80% and up to 48-fold enhancement for lower starting quantum yields. All the experiments were conducted under anaerobic conditions due to the reversiblity of the brightening in the presence of oxidants, but the results suggest routes for permanent enhancement and encourage further study of the nature of the redox-active surface sites.

6.2 Outlook

6.2.1 Mn^{2+}:CdS Photodoping

Extending photodoping to colloidal suspensions of Mn^{2+}:CdS QDs would allow for further investigation of the Mn-Auger phenomena discussed in Chapter 2. The electron hopping mechanism is a major contributor to the extremely efficient Auger quenching of the Mn^{2+} PL in QD films as it allows for one electron to sample multiple excited QDs on the time scale of the Mn^{2+} PL lifetime. In colloidal suspensions, the electron hopping will be affected by the concentration of the QDs and therefore may lead to a concentration dependence of the Auger quenching. Additionally, the optical quality improves by moving away from electrochemical films and into colloidal suspensions and would allow for further confirmation of the results presented in Chapter 2. Finally, colloidal suspensions would allow for the first EPR measurements of charged Mn^{2+}-doped chalcogenide QDs that would complement what is all ready known about the magenetic properties of Mn^{2+} in ZnO[1] and chalcogenide[2] QDs.

Photodoping of colloidal undoped and Mn^{2+}-doped CdS QDs has been attempted, but with limited success thus far. In Figure 6.1 photodoping of undoped CdS with Li[Et_3BH] is achieved as is shown by the characteristic reversible bleach of the first excitonic transition. However, the Mn^{2+}-doped CdS appears to be resistant to photodoping with Li[Et_3BH] as no changes in the absorption were observed. It is likely that the presence of more surface traps on the large Mn^{2+}:CdS is contributing towards the difference in behavior between these two smaples, but further investigations are needed to determine whether Mn^{2+}:CdS can be effectively photodoped.

6.2.2 Microscopic Nature of ZnSe Surface Traps

The methods of electrobrightening in Chapter 4 and redox brightening in Chapter 5 exist due to the significantly large number of surface traps present on ZnSe QDs.[3–6] While it is commonly

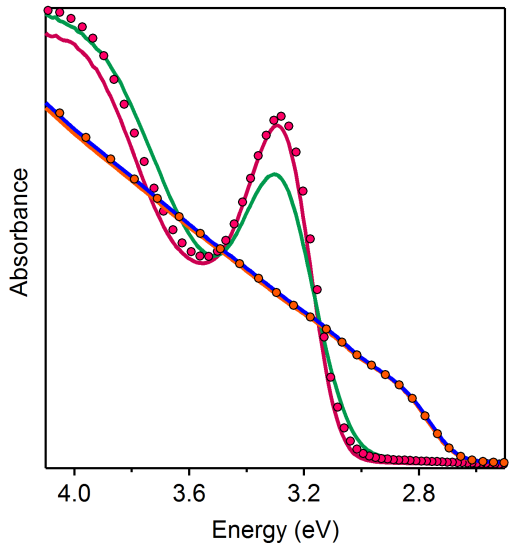

Figure 6.1: Attempted photodoping of colloidal undoped and Mn^{2+}-doped CdS QDs. Absorption spectra are shown before exposure to Li[Et_3BH], after addition of Li[Et_3BH] and photoexcitation, and upon reoxidation in air for d = 3.0 nm undoped CdS (red solid, green solid, and red circles, respectively) and d = 5.0 nm Mn^{2+}-doped CdS (orange solid, blue solid, and orange circles, respectively).

accepted that the ZnSe surface is extremely susceptible to the formation of traps, very little is known about the microscopic nature of these traps and hence the chemical mechanism that leads to electrobrightening and redox brightening is unclear. If the mechanism could be understood, it could possibly be exploited to yield higher QY QDs without the need for synthetic shell growth.

Future experiments should focus on examining the brightening properties of QDs with engineered surfaces that would address the reactivity of expected traps. For example, the brightening characteristics of QDs with either a Se-rich or Zn-rich surface could be examined to determine whether the active trap sites are due to unpassivated Zn or Se. It is also possible that the native ligands on the QDs undergo a chemical reaction in the presence of a reductive species. Recent NMR studies of QDs have been able to determine the nature of bound and unbound ligands on QDs,[6–10] and this technique could be used to determine whether the bound/unbound fraction changes upon brightening and whether the ligands themselves are being chemically reduced.

6.3 Notes to Chapter 6

[1] Ochsenbein, S. T.; Feng, Y.; Whitaker, K. M.; Badaeva, E.; Liu, W. K.; Li, X.; Gamelin, D. R. *Nat. Nanotech.* **2009**, *4*, 681–687.

[2] Beaulac, R.; Schneider, L.; Archer, P. I.; Bacher, G.; Gamelin, D. R. *Science* **2009**, *325*, 973–976.

[3] Alivisatos, A. P. *Science* **1996**, *271*, 933–937.

[4] Kilina, S.; Ivanov, S.; Tretiak, S. *J. Am. Chem. Soc.* **2009**, *131*, 7717–7726.

[5] Bryant, G. W.; Jaskolski, W. *J. Phys. Chem. B* **2005**, *109*, 19650–19656.

[6] Morris-Cohen, A. J.; Malicki, M.; Peterson, M. D.; Slavin, J. W. J.; Weiss, E. A. *Chem. Mater.* **2012**,

[7] Moreels, I.; Martins, J. C.; Hens, Z. *Sens. Actuators, B* **2007**, *126*, 283–288.

[8] Moreels, I.; Fritzinger, B.; Martins, J. C.; Hens, Z. *J. Am. Chem. Soc.* **2008**, *130*, 15081–15086.

[9] Ji, X.; Copenhaver, D.; Sichmeller, C.; Peng, X. *J. Am. Chem. Soc.* **2008**, *130*, 5726–5735.

[10] Fritzinger, B.; Moreels, I.; Lommens, P.; Koole, R.; Hens, Z.; Martins, J. C. *J. Am. Chem. Soc.* **2009**, *131*, 3024–3032.

Appendix A

Supporting Information for Chapter 2

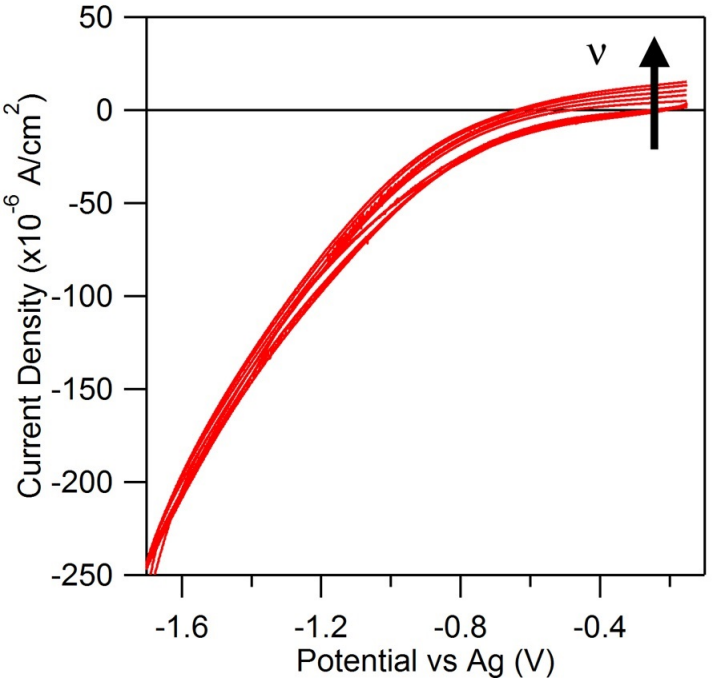

Figure A.1: Cyclic voltammogram of MPTMS-treated FTO in 0.1 M TBAP in DMF. Increasing the scan rate from 5 to 100 mV/s causes an increase in current, probably due to the slow oxidation of the FTO. The current observed at negative potentials likely contributes to the asymmetry between forward and reverse scans in the CV data of Fig. 2.3a.

A.1 $k_{\mathbf{Aug}}$ and $k_{\mathbf{ex}}$ in undoped CdSe QDs from literature

The values of k_{Aug} and k_{ex} used to calculate the dashed line for undoped QDs shown in Fig. 2.5c of the main text were obtained from refs. 1 and 2 as follows: The trion's (exciton plus e^{-}_{CB}) lifetime was reported in ref. 1 to be $\tau_{\mathrm{T}^{-}} \sim 1ns$ and its radiative lifetime was reported to be $\sim$ 10 ns. Using eq A.1, these values yield a trion Auger rate constant of $k_{\mathrm{Aug}} = 0.9 \times 10^{9}\ \mathrm{s}^{-1}$. From the range of reported QD diameters from 5.3 to 6.7 nm, this value corresponds to $k_{\mathrm{Aug}} =$

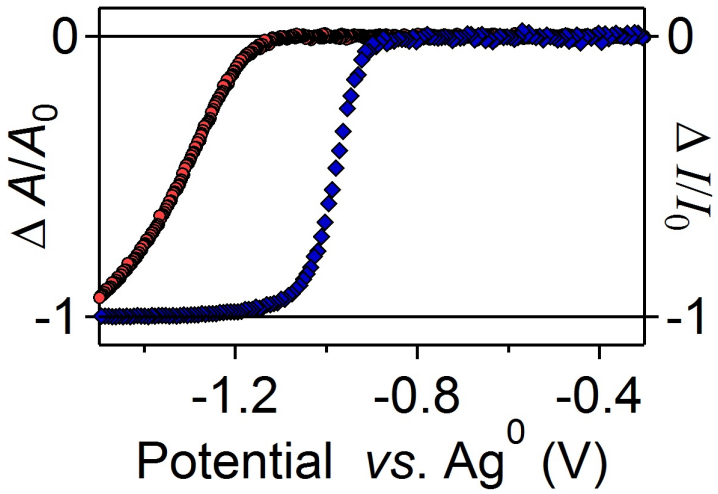

Figure A.2: Voltage response of $\Delta A/A_0$ at 2.8 eV (●) and $\Delta I/I_0$ integrated between 2.0 and 2.5 eV (◆) for the Mn^{2+}:CdS QDs from Fig. 2.6, plotted *vs* Ag^0.

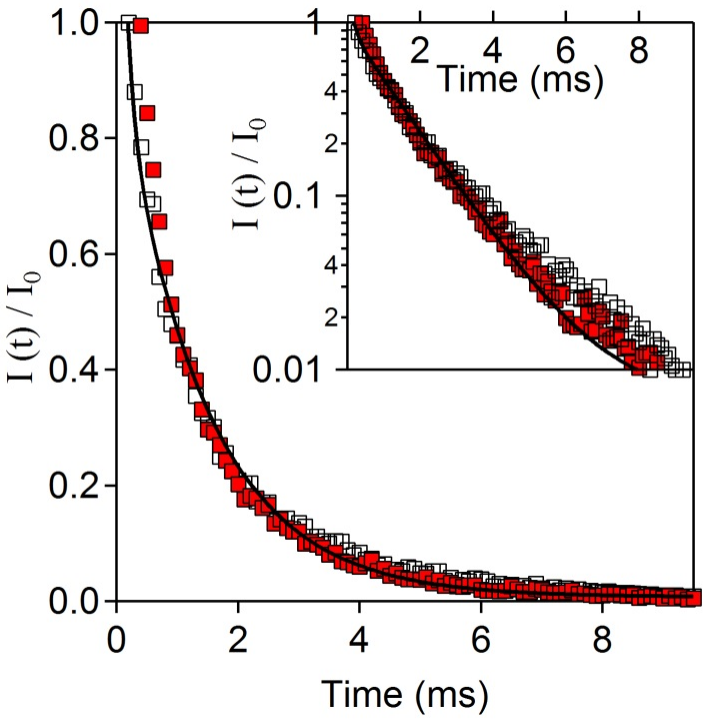

Figure A.3: Room-temperature photoluminescence decay curves measured between 2.0 and 2.5 eV for $d_{QD} = 4.5$ nm 0.5% Mn^{2+}:CdS QDs in colloidal suspension (❑) and as an uncharged film on FTO (■). The solid line shows a biexponential fit of the colloidal QD decay curve (48% $\tau_1 = 1.2 \times 10^{-4}$ s, 52% $\tau_2 = 1.4 \times 10^{-3}$ s). The Mn^{2+} PL decay dynamics do not change significantly upon film formation.

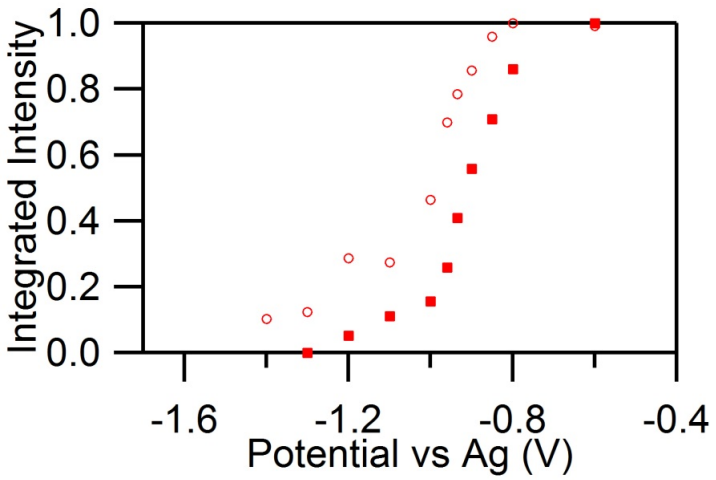

Figure A.4: Integrated Mn^{2+} (■, 2.075-2.15 eV) and trap (○, 1.75-1.80 eV) PL intensities for $d_{QD} = 4.5$ nm 0.5% Mn^{2+}:CdS QDs, measured as a function of applied electrochemical potential. The trap PL quenches at a potential ∼100 meV more negative than the Mn^{2+} PL.

0.9×10^9 cm^3s^{-1} to 1.0×10^{-10} cm^3s^{-1}.

$$k_{Aug} = \frac{1}{\tau_{T^-}} - \frac{1}{\tau_{T^-}^{rad}} \tag{A.1}$$

Similarly, the rate constant describing non-radiative contributions to the exciton's lifetime was reported in ref. 2 to be $k_{ex}^{nonrad} = 3.3$ ns^{-1} ($1/0.3$ ns), and the exciton's radiative lifetime was reported to be $\tau_{ex}^{rad} = 15$ ns (or $k_{ex}^{rad} = 6.7 \times 10^7$ s^{-1}). Using eq A.2, these data yield an exciton decay rate constant of $k_{ex} = 3.4 \times 10^9$ s^{-1}.

$$k_{ex} = k_{ex}^{rad} + k_{ex}^{nonrad} \tag{A.2}$$

These values were used to simulate the PL quenching data for undoped QDs shown in Fig. 2.5c using eq 2.5 from the main text. All other parameters used for these calculations were fixed at the same values as used for simulation of the Mn^{2+}:CdS QD data.

A.2 Additional experimental details

A.2.1 Synthesis

Colloidal wurtzite 0.5% Mn^{2+}:CdS nanocrystals were prepared following literature methods,[3] with the following modifications: A flask containing a solution of manganese acetate tetrahydrate (0.032 mmol) in oleylamine (OA, 4.60 mmol) was degassed at room temperature, purged with dry nitrogen gas, and degassed under vacuum again while gently heating to remove the hydrates. The flask was then flushed with nitrogen gas before its contents were injected into the cadmium oleate solution at 310°C. The temperature dropped to 285°C and was re-stabilized at 290°C. A solution of 68.8 mg S^0 (2.15 mmol) in 3.26 g ODE was degassed at ∼100 °C for 5 minutes, purged with dry nitrogen gas, and quickly injected into the colorless cation solution at 290°C. Heating the solutions of manganese acetate and sulfur dehydrated the manganese acetate and helped to dissolve all the solids. After repeated washings with ethanol, the nanocrystals were re-suspended in trioctylphosphine oxide (TOPO) at 160°C and sonicated for 10 minutes at 60°C. In order to increase the PL quantum yield, 2 mL of heptane was used to re-suspend the particles after precipitation with ethanol. This suspension was added at 100°C to a mixture of 7.96 g ODE and 4.13 g OA that had been degassed at 130 °C for 30 minutes. Avoiding exposure to air, 7.5 mL trioctylphosphine (TOP) was carefully injected, and the solution was stirred for ∼6 days at 130°C. Following this procedure, the nanocrystals were precipitated twice more as above and stored as a colloidal suspension in toluene.

A.2.2 Electrochemistry

Electrochemical films of nanocrystalline Mn^{2+}:CdS QDs were prepared according to literature methods.[1,2,4] Fluorine doped tin oxide (FTO) slides (Hartford Glass, 20 × 6 mm) were cleaned and their conductive surfaces treated with 3-mercaptopropyltrimethoxysilane while heating at 70°C for

15 minutes. The slides were rinsed with chloroform to remove excess silane, then cured at 120°C for 30 minutes. The FTO was masked to an area of 0.36 cm^2, and the colloidal nanocrystals were drop-coated from toluene. After drying, the mask was removed and a wire was soldered to the FTO. The QDs were cross-linked in an N_2 glovebox by dipping in a 1%(V/V) solution of 1,7–heptanediamine in ethanol at 70°C for one minute then heating the substrate at 70 °C for between 0.5 and 3.0 hours. The films were then placed under vacuum for 1 hour. The electrochemical cells were assembled under N_2 atmosphere using a platinum wire as the counter electrode, a silver wire as a pseudo-reference electrode, and a 0.1 M solution of tetrabutylammonium perchlorate (TBAP) in dimethylformamide (DMF) as electrolyte.[2,4,5] An 8 mm diameter NMR tube (Wilmad) was used as the body of the electrochemical cell. A μ-autolab II potentiostat was used to control the potential and record the current in linear sweep and cyclic voltammetry modes. All electrochemical measurements were performed at 210 K in a flow cryostat under N_2 atmosphere.

A.2.3 Analytical characterization

Manganese and cadmium concentrations were determined by inductively coupled plasma atomic emission spectroscopy (ICP-AES, Jarrel Ash model 955). Powder X-ray diffraction was collected on a Bruker D5000 instrument with a copper Kα source. EPR spectra were measured on colloidal Mn^{2+}:CdS QDs in toluene using an Bruker E580 Xband spectrometer. Quantum yields were measured exciting at 375 nm using a Hamamatsu C9920 Absolute PL Quantum Yield Measurement System.

A.2.4 Spectroscopy

Electronic absorption spectra were collected using a Cary 500 (Varian) spectrophotometer on free-standing colloids in toluene at 300 K, or on electrochemical films at 210 K. MCD spectra were collected on drop-coated films using an Aviv 40DS spectropolarimeter and a high-field superconducting magneto-optical cryostat (Cryo-Industries) with a variable-temperature sample compartment

positioned in the Faraday configuration. MCD intensities are reported as differential absorbance, $\Delta A = A_L - A_R$, where A_L and A_R refer to the absorption of left and right circularly polarized photons following the sign convention of Piepho and Schatz.[6] CW photoluminescence spectra were collected using the 366 nm line of a CW Ar^+ laser (Spectra-Physics). A 0.5 m monochromator (Acton) and CCD detector (Princeton) were used for detection. Photoluminescence excitation measurements were performed using a 200 W halogen lamp dispersed through a 0.3 m monochromator (Acton) and a PMT with lock-in amplification for detection (λ = 585 nm, 25 nm spectral band pass). For absorption measurements performed simultaneously with PL measurements, a PMT and photon counter were used for PL detection, and a silicon photodiode with lock-in detection was used for detection of transmitted photons. Lifetime measurements were performed using the 366 nm output of a $\sim$10 Hz pulsed N_2/dye laser for excitation and a PMT with photon counting for detection (λ = 585 nm, 25 nm spectral band pass). All PL measurements involved excitation well above the band edge to minimize changes in excitation density due to absorption bleaching.

A.3 References

[1] Jha, P. P.; Guyot-Sionnest, P. *ACS Nano* **2009**, *3*, 1011–1015.

[2] Jha, P. P.; Guyot-Sionnest, P. *J. Phys. Chem. C* **2007**, *111*, 15440–15445.

[3] Nag, A.; Chakraborty, S.; Sarma, D. D. *J. Am. Chem. Soc.* **2008**, *130*, 10605–10611.

[4] Guyot-Sionnest, P.; Wang, C. *J. Phys. Chem. B* **2003**, *107*, 7355–7359.

[5] Haram, S. K.; Quinn, B. M.; Bard, A. J. *J. Am. Chem. Soc.* **2001**, *123*, 8860–8861.

[6] Piepho, S. B.; Schatz, P. *Group Theory in Spectroscopy: With Applications to Magnetic Circular Dichroism*; Wiley, New York, 1983; Vol. 88; pp 1023–1023.

Appendix B

Supporting Information for Chapter 3

B.1 Methods

B.1.1 Synthesis of CdSe nanocrystals

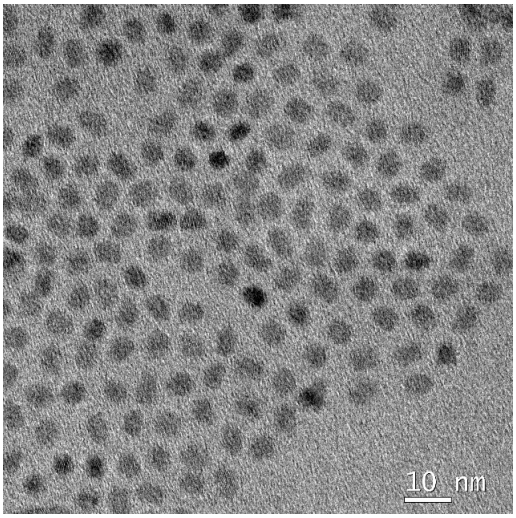

Figure B.1: Representative TEM image of 4.6 nm CdSe nanocrystals.

CdSe nanocrystals were synthesized according to a literature method.[1] For 4.6 nm nanocrystals, cadmium oxide (60 mg), octadecylphosphonic acid (280 mg) and trioctylphosphine oxide (3.0 g) were added to a 50 mL round bottom flask, heated to $\sim$130°C and degassed under vacuum for $\sim$1.5 hours. The reaction mixture was heated under nitrogen to above 350°C to form an optically clear and colorless solution. After adding 1.0 mL trioctylphosphine (TOP) to the solution, the temperature was brought up to 375°C, at which point Se/TOP (60 mg Se in 0.5 mL TOP) solution was swiftly injected into the flask. The CdSe cores were grown at $\sim$370°C until desired size was reached (2-5 min) at which point growth was halted by removing the heating mantle. The

cooled CdSe nanocrystals were washed repeatedly by precipitating with ethanol and redissolving in toluene.

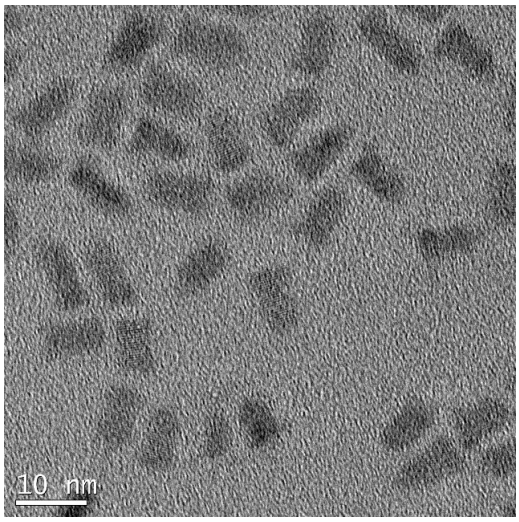

Figure B.2: Representative TEM image of 4.6 nm CdSe nanocrystals with a ZnSe shell. Because of shape anisotropy, an average shell thickness was estimated by distributing the total shell volume equally around the central CdSe core. Core/shell volumes were modeled as rectangular cuboids with a = b $<$ c, estimated from TEM data.

B.1.2 Synthesis of CdSe/ZnSe core/shell nanocrystals

CdSe/ZnSe QDs were synthesized according to a literature method[2] with modifications. A 50 mL round bottom flask with $\sim 2 \times 10^{-7}$ mol of washed CdSe cores, oleylamine (5 mL), and octadecane (5 mL) was heated to $\sim$115°C and degassed under vacuum for $\sim$1.5 hours. Stock solutions of $\sim$0.2 M selenium dissolved in TOP and $\sim$0.2 M Zn-oleate in 1:1 (m/m) octadecene and decylamine were used as precursors for shell growth. The exact amount of precursors used for each monolayer of shell growth was calculated according to the increase in volume of each shell monolayer, taking into account the change in total QD size throughout growth. The reaction temperature was set at 200°C under nitrogen. Growth times were 2.5 h for each cadmium addition and 1 h for each selenium addition. Aliquots were taken during growth and the amount for each addition of shell precursor was adjusted to take into account the lesser amount of remaining QDs. The cooled

CdSe/ZnSe nanocrystals were washed repeatedly by precipitating with ethanol and redissolving in toluene.

B.1.3 Syntehsis of CdE (E = S, Te) nanocrystals

CdS nanocrystals were synthesized by published methods.[3] CdTe nanocrystals were synthesized by a slight modification of published methods.[4] Briefly, CdO (13 mg), hexadecylphosphonic acid (60 mg), and octadecene (3.9 g) were degassed at 110°C for 40 min and heated to 300°C under nitrogen. To this stirring solution, an air-free solution of Te (25 mg) tributylphosphine (0.6 mL), and octadecene (1.5 g) was injected swiftly. The stirring solution cooled to ∼270°C and was held there for 3 min. The solution was cooled to room temperature and twice precipitated with acetone, centrifuged and redissolved in toluene.

B.1.4 Photoluminescence

Time resolved PL measurements were taken by exciting with the frequency doubled output of a Ti:Sapphire with the repetition rate reduced from 76 MHz to 500 kHz using a pulse picker (400 nm, 150 fs pulse with, 0.7 nJ/pulse) and detected using a streak camera coupled to a monochromator with an IRF of $\sim$ 15 ps. Concurrent quasi-CW measurements were detected using a perpendicular Ocean Optics 2000+ spectrometer.

B.1.5 IR Absorption

For infrared (IR) absorption measurements, nanocrystal solutions were prepared in the dark in a nitrogen glove box to be 10-100 μM in toluene with 250-1000 equivalents Li[Et_3BH]. These solutions were loaded into an air-free IR cell comprised of a 100 μm spacer between two CaF_2 windows, which was kept in the dark until background absorption measurements were taken. The as-prepared nanocrystal solutions were used as a background. The IR cell was then exposed to visible light using the white light LED on a Galaxy Nexus by Samsung smartphone (λ_{max} = 436,

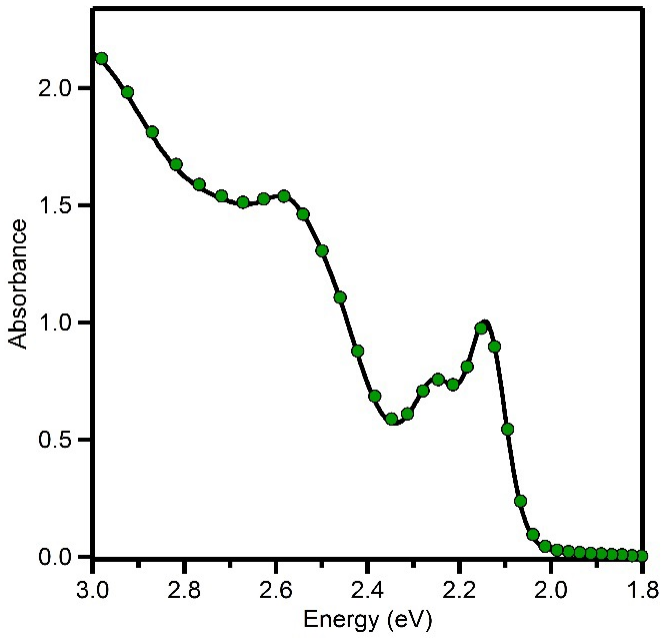

Figure B.3: Absorption spectra of d = 3.8 nm CdSe nanocrystals before and after the addition of Li[Et_3BH] but without exposure to light other than the spectrometer source used for the measurement of these spectra.

535 nm) for short times (1−20 s between spectra). The IR absorption was monitored until no further increase was observed.

B.1.6 Photodoping using Li[Et_3BH]

Li[Et_3BH] was purchased from Sigma-Aldrich as a 1 M solution in THF, and was diluted with dry THF for photodoping experiments. Photodoping experiments could be done under a wide range of conditions, but typically worked best with 10-100 equivalents of Li[Et_3BH] per CdSe nanocrystal. CdSe nanocrystal concentrations were determined by absorption.[4] Solutions were prepared and kept in the dark until photodoping. Without exposure to visible light (beyond the low-level excitation used in the absorption measurement), no measureable nanocrystal absorption bleach or IR absorption was detected (Fig. B.3). Photodoping was achieved with a variety of light sources. Many samples could be photodoped in the presence of ambient room light, but more efficient photodoping could be achieved using a white light LED or photolysis lamp with a λ =

450 nm cutoff filter (to prevent UV illumination) and a water IR filter (to prevent sample heating).

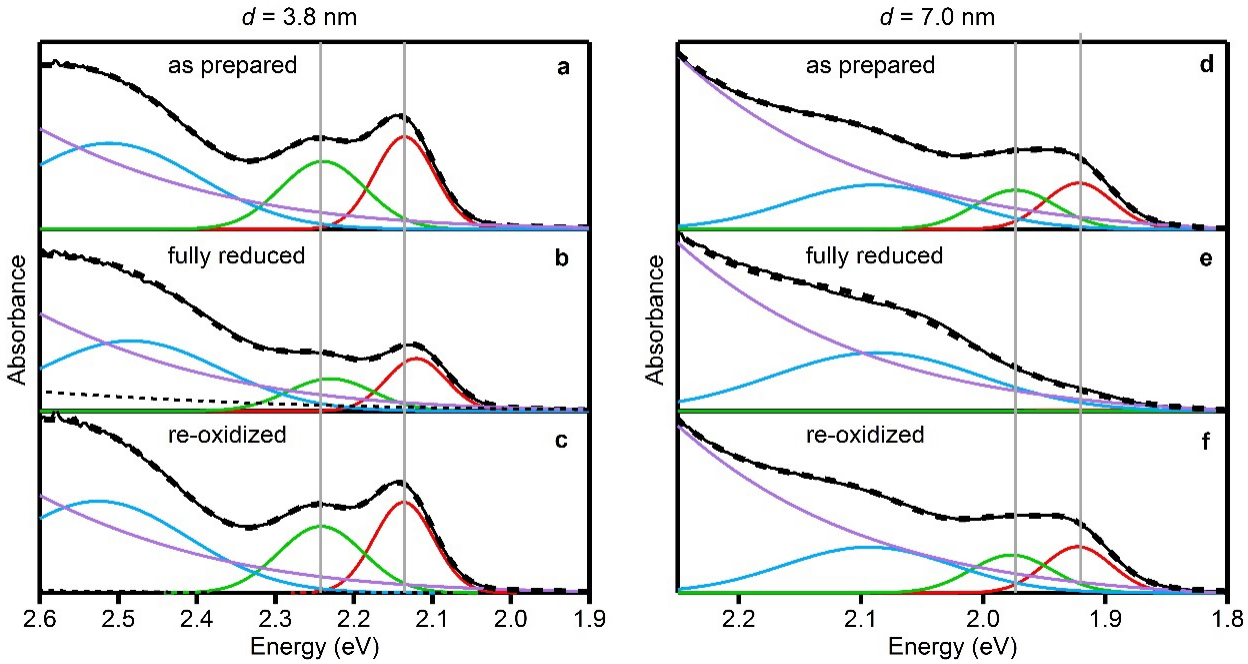

Figure B.4: Multi-Gaussian fits (thick black dashed) of absorption spectra (thin black) of d = 3.8 nm **(a,b,c)** and d = 7.0 nm **(d,e,f)** CdSe nanocrystals before photodoping **(a,d)**, at maximum photodoping **(b,e)**, and after re-oxidation **(c,f)**. All absorption spectra are fitted with a sum of four Gaussians. The magnitudes, positions, and widths of the three lowest-energy Gaussians (red, green, blue) were allowed to float during fitting. The highest-energy Gaussian (purple) accounts for rising absorption in the high-energy region, and its amplitude, position, and width were fixed to be equal across all three panels for a given nanocrystal. The fitting of the smaller nanocrystals also incorporated a small additional Gaussian (thin black dashed) to account for the slight pre-edge tail that appears after photodoping.

B.1.7 Electron counting by titration against $[FeCp^{\star}_2][BAr_F]$

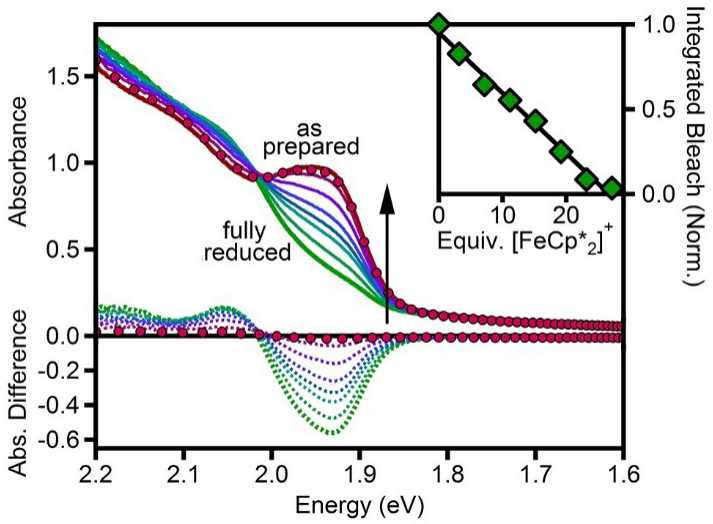

Figure B.5: Absorption spectra of $d = 7.0$ nm (4.4 μM) CdSe nanocrystals collected during redox titration in 1:1 toluene/THF. The red spectrum shows data collected before introduction of $Li[Et_3BH]$. The solid green spectrum is of the maximally photodoped nanocrystals. The other spectra were collected following addition of various amounts of $[FeCp^{\star}_2]^+$ (increasing with direction of arrow). The red circles show the solution after reoxidation with air. The corresponding difference spectra ($A - A_{\text{as prepared}}$) are plotted as dotted lines. **Inset:** The integrated absorption bleach of the first excitonic feature as a function of equivalents of $[FeCp^{\star}_2]^+$. The solid line shows a linear fit to the data. The crossing of this line with zero indicates the equivalence point, corresponding to 27 electrons per nanocrystal.

For comparison with numbers determined by fitting of the optical bleach, the average number of excess electrons per nanocrystal ($\langle n_{\text{max}} \rangle$) was determined by titration against $[FeCp^{\star}_2][BAr_F]$.[5–7] Direct reaction of $[FeCp^{\star}_2][BAr_F]$ with excess $Li[Et_3BH]$ was found to be slow compared to the nanocrystal oxidation, ruling out the possibility of anomalously large electron counts due to the titration method. Additionally, a nanocrystal-catalyzed reaction of $[FeCp^{\star}_2][BAr_F]$ with excess $Li[Et_3BH]$ can be ruled out because both d = 3.8 and 4.6 nm nanocrystals showed much lower electron counts than the d = 7.0 nm nanocrystals despite similar concentrations of $Li[Et_3BH]$. All titrations, including absorption measurements, were conducted in a nitrogen glove box. A solution of 1-50 μM CdSe nanocrystals in 1:1 toluene/THF was prepared in a 1 cm quartz cuvette with a 2 mm sample path-length. Excess trioctylphosphine oxide was added to aid in solubility. A

starting absorption spectrum (denoted "as prepared") was measured using an Ocean Optics 2000+ spectrometer with an absorption attachment. To the cuvette, 20-100 equivalents $Li[Et_3BH]$ was added as a solution in 10 μL THF. The absorption was monitored using the Ocean Optics, which simultaneously provided light for photodoping. The nanocrystal solutions were left in the Ocean Optics lamp until the first exciton absorption stopped decreasing. To these maximally photodoped nanocrystals, 10 μL aliquots of $[FeCp^{\star}_2]\,[BAr_F]$ in THF were added and recovery of the first exciton absorption was monitored. To analyze the titration data, difference spectra (maximally photodoped - as prepared) were integrated over the first exciton, and the amount of bleach was plotted as a function of added $[FeCp^{\star}_2]\,[BAr_F]$. The data were fit to a line, with the x-intercept representing the equivalence point.

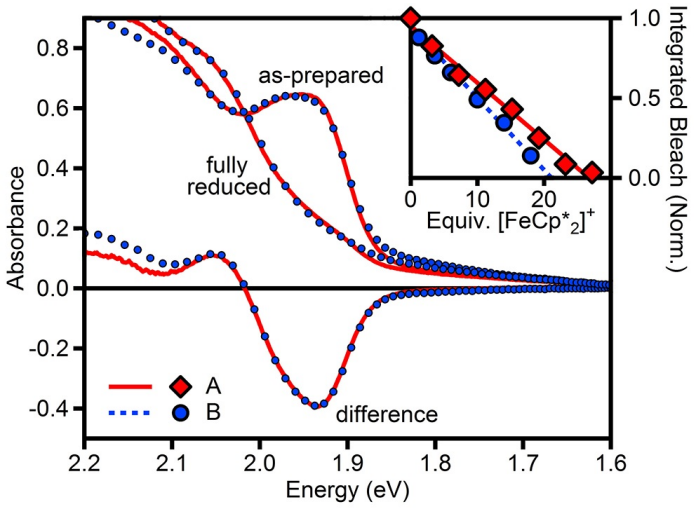

Figure B.6: Absorption spectra of two different samples of the same d = 7.0 nm (4.4 μM) CdSe nanocrystals collected during redox titration in 1:1 toluene/THF. The samples differ in their history, (A) having been stored under N_2 and (B) having been stored in air for a different duration, and the accompanying differences in sample handling in preparation necessary for these measurements. The absorption data for the two samples before and after photodoping are essentially indistinguishable, but the titration data show a significant difference in the number of electrons retrieved from these nanocrystals (of $\sim$ 7 electrons/nanocrystal). These data support the conclusion that the absorption bleach reports on the delocalized conduction electrons, whereas the chemical titration is also sensitive to other (trapped) electrons.

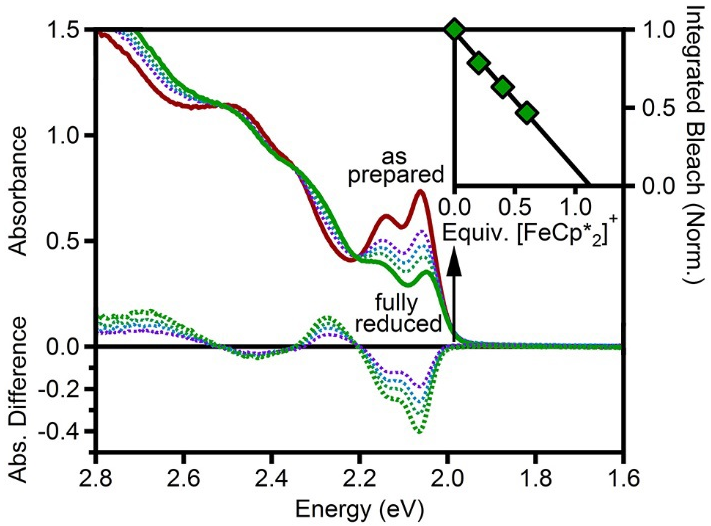

Figure B.7: Absorption spectra of $d = 4.6$ nm (10.6 μM) CdSe nanocrystals collected during redox titration in 1:1 toluene/THF. The red spectrum shows data collected before introduction of $Li[Et_3BH]$. The solid green spectrum is of the maximally photodoped nanocrystals. The other spectra were collected following addition of various amounts of $[FeCp^{\star}_2]^+$. (increasing with direction of arrow). The corresponding difference spectra ($A - A_{\text{as prepared}}$) are plotted as dotted lines. Inset: The integrated absorption bleach of the first excitonic feature as a function of equivalents of $[FeCp^{\star}_2]^+$.. The solid line shows a linear fit to the data. The crossing of this line with zero indicates the equivalence point, corresponding to 1.1 electrons per nanocrystal.

B.2 Photodoping of CdE (E = S, Te) nanocrystals

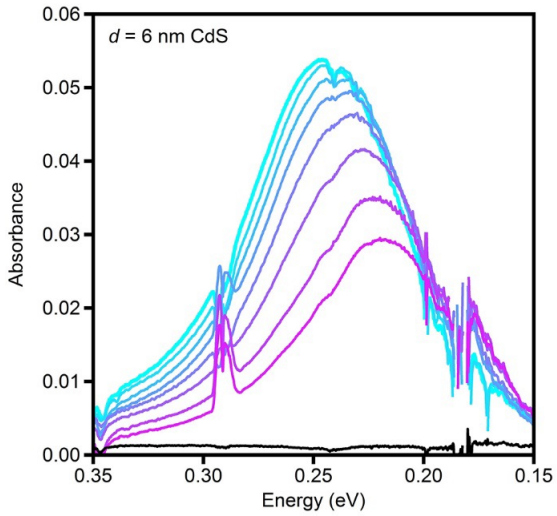

Figure B.8: IR spectra demonstrating the introduction of electrons into the conduction band of a 1:1 THF:toluene CdS nanocrystal colloidal suspension after introduction of Li[Et_3BH] and incremental exposure to UV/Vis radiation.

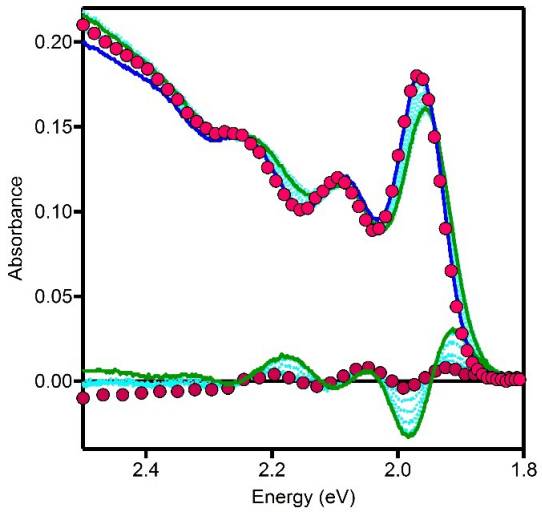

Figure B.9: Absorption spectra of CdTe (d = 4 nm) in THF solution (1 μM) as prepared (blue line), after addition of 40 equivalents of Li[Et_3BH] and $\lambda > 450$ nm light exposure (dotted blue and green lines), and after reoxidation in air (red circles). Difference spectra of matching colors are shown below.

B.3 Per-electron molar extinction coefficient

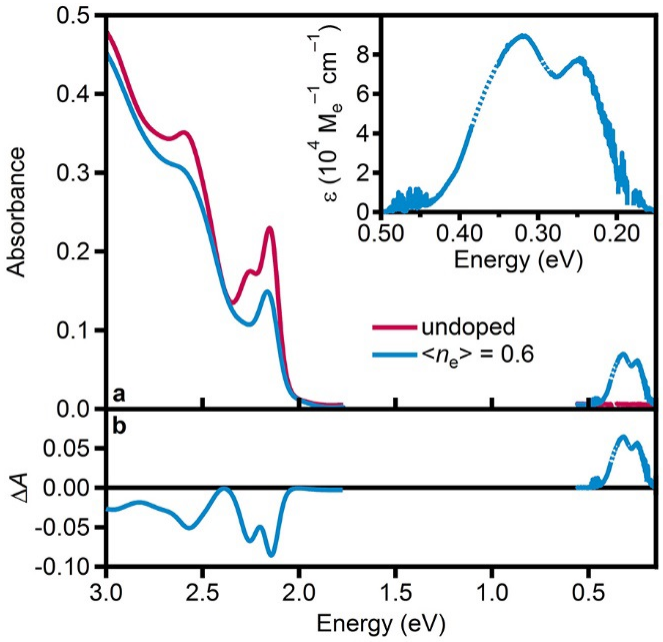

Figure B.10: **(a)** Visible/IR absorption spectra for undoped (purple) d = 3.8 nm CdSe nanocrystals and the same nanocrystals photodoped to $\langle n_e \rangle$ = 0.6 electrons per nanocrystal (blue). Regions of intense C-H and CO_2 vibrational absorption are interpolated (dotted lines). **(b)** Difference spectra (photodoped - undoped), from the spectra in (a). **Inset:** Extinction coefficient plot for the IR absorption in units of $M_e^{-1} \cdot cm^{-1}$, where M_e is the molar concentration of conduction-band electrons. The per-electron molar extinction coefficient for the IR absorption maximum in these nanocrystals is $8.9 \pm 0.6 \times 10^4$ $M_e^{-1} \cdot cm^{-1}$ at 0.32 eV. Note that this extinction coefficient is for this specific nanocrystal diameter, because the spectrum changes with nanocrystal diameter (Figure 3.1).

B.4 CdSe Film Photodoping

CdSe quantum dots (d = 7.0 nm) were drop cast onto a fluorine-doped tin oxide (FTO) substrate and dried under inert atmosphere. A THF solution of $Li[Et_3BH]$ (20 μL, 0.1 M) was introduced to the dried CdSe film and allowed to dry. Absorption spectra were collected with exposure to visible light and after reoxidation using an Ocean Optics 2000+ spectrometer with an absorption attachment.

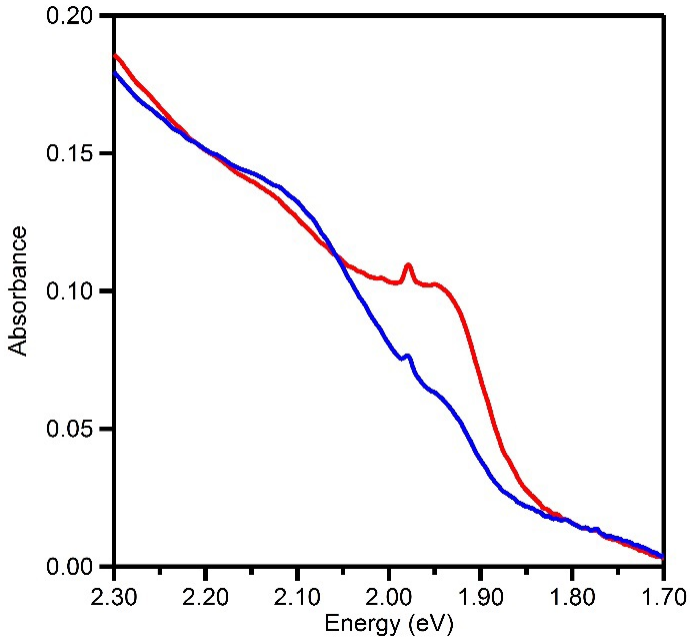

Figure B.11: Absorption spectra of $d = 7.0$ nm quantum dot film on FTO maximally photodoped (blue) and reoxidized (red). The small sharp peak at ~ 1.98 eV is due to film reflections.

B.5 References

[1] Carbone, L. et al. *Nano Lett.* **2007**, *7*, 2942–2950.

[2] Ghosh, Y.; Mangum, B. D.; Casson, J. L.; Williams, D. J.; Htoon, H.; Hollingsworth, J. A. *J. Am. Chem. Soc.* **2012**, *134*, 9634–9643.

[3] Yu, W. W.; Peng, X. *Angew. Chem. Int. Ed.* **2002**, *41*, 2368–2371.

[4] Yu, W. W.; Qu, L.; Guo, W.; Peng, X. *Chem. Mater.* **2003**, *15*, 2854–2860.

[5] Schrauben, J. N.; Hayoun, R.; Valdez, C. N.; Braten, M.; Fridley, L.; Mayer, J. M. *Science* **2012**, *336*, 1298–1301.

[6] Schimpf, A. M.; Ochsenbein, S. T.; Buonsanti, R.; Milliron, D. J.; Gamelin, D. R. *Chem. Commun.* **2012**, *48*, 9352–9354.

[7] Schimpf, A. M.; Gunthardt, C. E.; Rinehart, J. D.; Mayer, J. M.; Gamelin, D. R. *J. Am. Chem. Soc.* **2013**, *135*, 16569–16577.

Appendix C

Supporting Information for Chapter 4

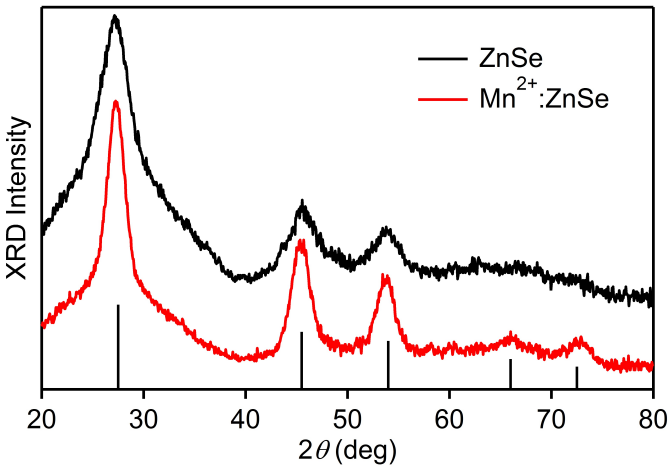

Figure C.1: Powder XRD of ZnSe (black) and 2.5% Mn^{2+}:ZnSe (red) QDs. The black bars indicate the anticipated powder diffraction peak positions for wurtzite ZnSe.

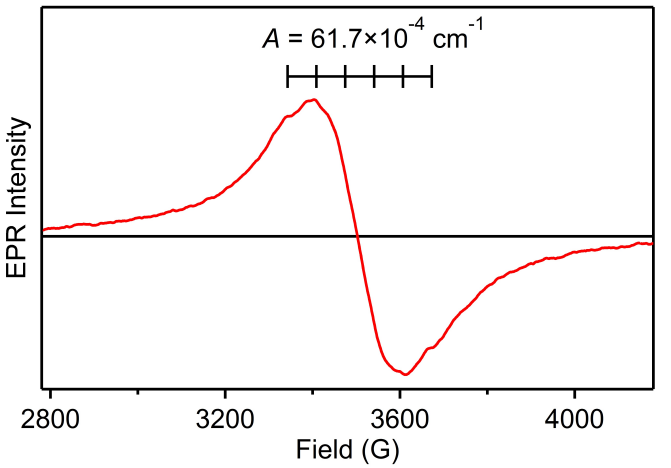

Figure C.2: Room temperature EPR spectrum of 2.5% Mn^{2+}:ZnSe QDs suspended in toluene. The anticipated hyperfine splitting pattern of Mn^{2+} in ZnSe is shown as a reference and coincides well with the observed structure. The spectrum is broadened due to the elevated Mn^{2+} concentration.

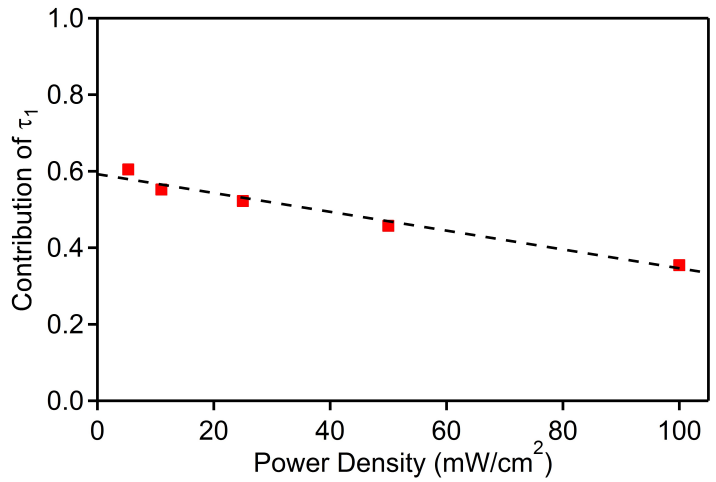

Figure C.4: Contribution of the fast component (τ_1) from Fig. 4.4 to the total electrobrightening at different excitation power densities. A linear fit of the data (black dashed) indicates $\sim 60\%$ contribution from the fast component in the limit of zero power density.

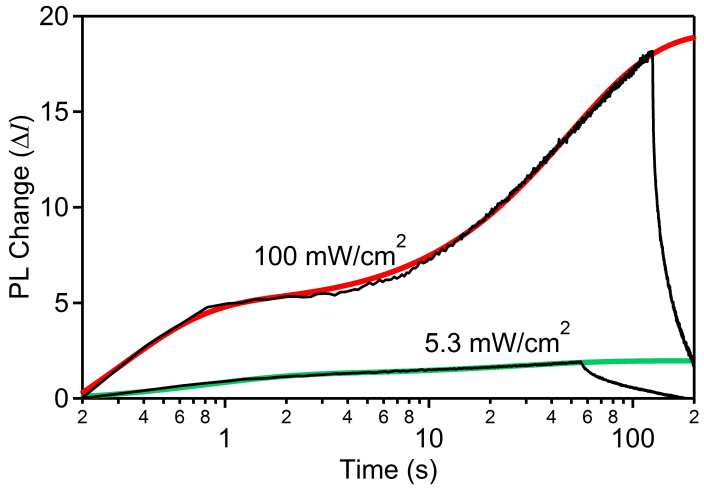

Figure C.3: Photoluminescence data from Fig. 4.4a, re-plotted on a semi-log scale to emphasize short times. These data describe the change in Mn^{2+} PL intensity (ΔI) at 590 nm during electrobrightening, measured at 100 and 5.3 mW/cm^2. The bi-exponential fits used to determine the two time constants (τ_1 and τ_2) plotted in Fig. 4.4b are also included.

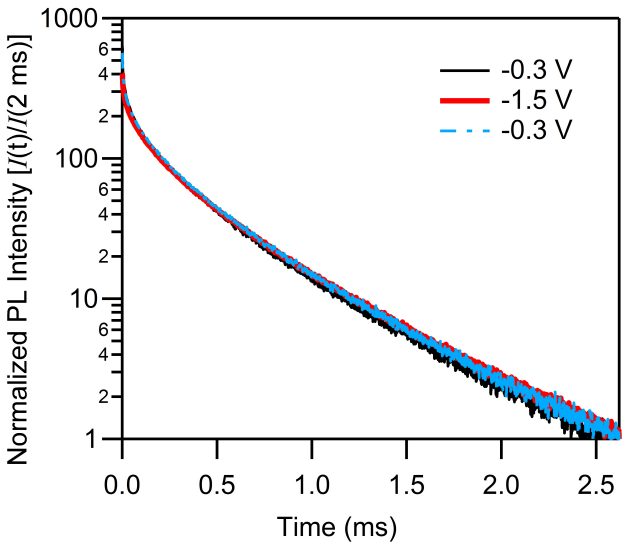

Figure C.5: The PL decay data of Fig. 4.5 re-plotted after normalization at 2.0 ms to emphasize that applied voltage does not influence the Mn^{2+} PL decay dynamics.

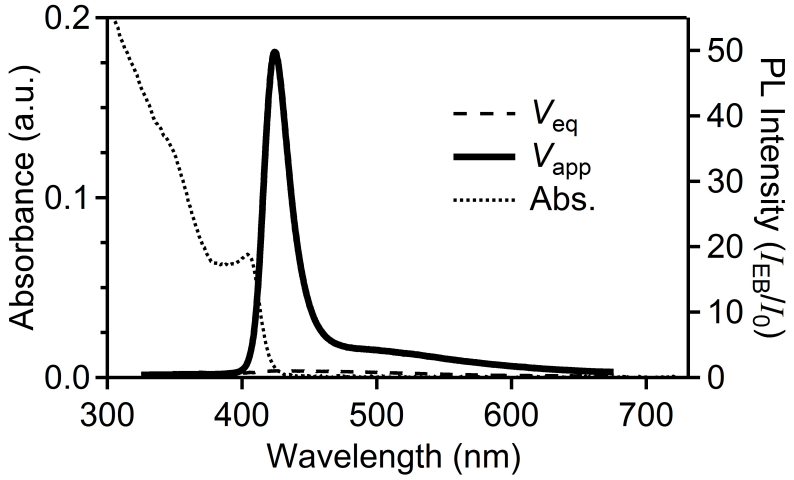

Figure C.6: Electrobrightening for a different ZnSe QD film from the one shown in Fig. 4.1, showing the same properties but less trap PL. For this film, $V_{eq} = -0.7$ V (most likely high due to drift of the Ag^0 pseudo-reference electrode) and $V_{app} = -2.0$ V. The PL quantum yield increases from 0.4% to 19.9%. The excitonic PL electrobrightening for this sample is $I_{EB}/I_0 \sim 50$. The absorption of the same ZnSe QDs as colloids is shown as a dotted line.

Appendix D

Supporting Information for Chapter 5

D.1 Methods

D.1.1 Synthesis

Colloidal Mn^{2+}:ZnSe nanocrystals (NCs) were synthesized by modification of a previously published procedure.[1] To briefly summarize, 10.8 g of hexadecylamine ($C_{16}H_{35}N$, 90%, Acros) and 8 mg $MnCl_2 \cdot 6H_2O$ were degassed under vacuum at 130°C for 1.5 h. The reaction vessel was placed under N_2 and the temperature reduced to 60°C, at which point 0.2 g of $(Me_4N)_2[Zn_4(SePh)_{10}]$ and 20 mg of selenium (99.9%, Aldrich) were introduced. The temperature was increased to 130°C under vacuum, maintained for 2 h, and then increased to 275°C under nitrogen and kept constant until the desired NC size was achieved. After growth, the solution was rapidly cooled to <100°C, and the particles were isolated by addition of $\sim$ 5 mL of toluene and $\sim$ 30 mL of ethanol. The isolated NCs were then resuspended in toluene. The process of precipitation with ethanol followed by resuspension in toluene was repeated three times to remove excess reagents. The precipitated nanocrystals were then gently heated in 6 g of 1-octadecene (90%, Aldrich), 1.5 g oleylamine (70%, Aldrich), and 3 mL TOP (TOP, 97%, Strem) at 120°C under nitrogen for $\sim$ 3 days.

For low quantum yield samples, the NCs were then precipitated with ethanol, resuspended in toluene, and stored in air for several months until a stable quantum yield of $\phi = 0.4\%$ was obtained. For high quantum yield samples, the NCs were precipitated with ethanol and resuspended in toluene under an inert atmosphere for storage.

D.1.2 Analytical Characterization

Manganese and zinc concentrations were determined by inductively coupled plasma optical emission spectrometry (ICP-OES, Perkin Elmer Optima 8300). Photoluminescence data was collected by exciting the nanocrystals using an unfocused 405 nm, 5 mW laser diode and detecting emitted photons using an Ocean Optics 2000+ fiber-coupled spectrometer.

D.1.3 Redox Brightening

In a typical experiment with sodium-potassium alloy on silica gel (NaK_2; Stage 1, Aldrich, main text Figure 5.2), 100 μL of a 26 μM toluene solution of colloidal Mn^{2+}:ZnSe NCs was placed in an air-free 1 cm quartz cuvette with 2 mL tetrahydrofuran (THF) and a small Teflon stir bar. For experiments with a molecular electron shuttle, 1 mg 2,2'-bipyridine was dissolved as well. Photoluminescence was monitored before and after addition of $\sim$ 5 mg NaK_2 with vigorous stirring.

In a typical brightening titration experiment (Figure 5.3), 20 μL of a 26 μM toluene solution of colloidal Mn^{2+}:ZnSe NCs was placed in an air-free 1 cm quartz cuvette with 2 mL tetrahydrofuran (THF) and a small Teflon stir bar. To eliminate potential complications from photobrightening, prior to titration experiments each sample was excited with a cw 405 nm laser until no further changes in PL intensity were observed. Subsequently, aliquots of reductant (anthracene radical, cobaltocene) were added by microliter syringe with vigorous stirring. Photoluminescence was measured shortly after each addition of reductant

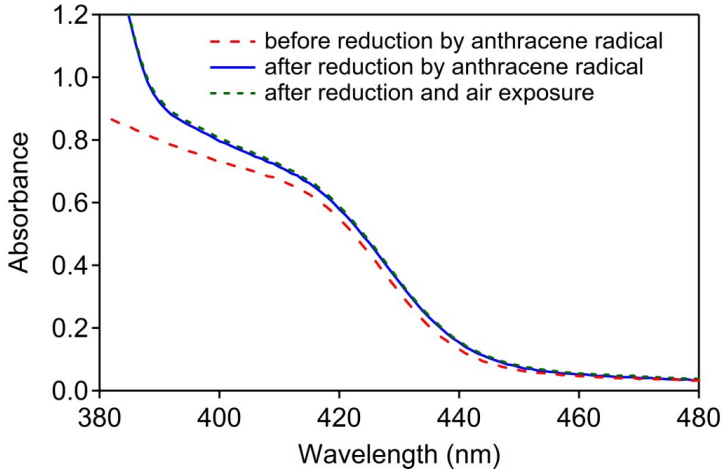

Figure D.1: Absorption spectra of 0.6% Mn^{2+}:ZnSe NCs suspended in tetrahydrofuran collected before and after brightening using anthracene radical, and again following air exposure of the brightened nanocrystals. The difference between spectra collected before and after brightening is due to absorption by oxidized anthracene radical (anthracene).

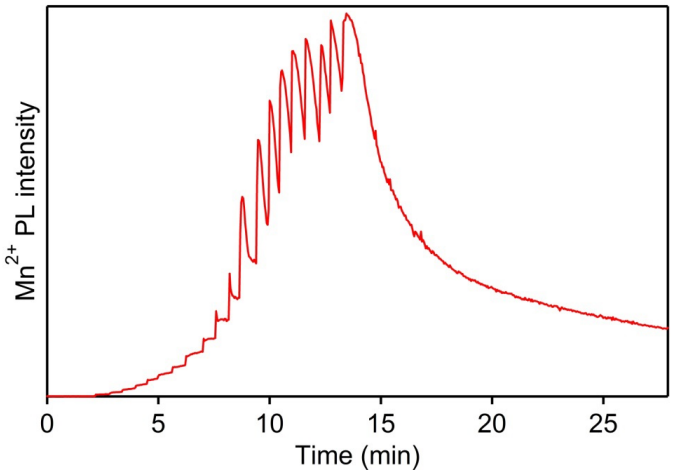

Figure D.2: Plot of Mn^{2+} PL intensity *vs* time during a typical reductant titration experiment. Spikes in the PL intensity mark additions of anthracene radical as described in Chapter 5.

D.2 References

[1] Archer, P. I.; Santangelo, S. A.; Gamelin, D. R. *J. Am. Chem. Soc.* **2007**, *129*, 9808–9818.

Vita

Amanda Leigh Thorsen was born Amanda Leigh Weaver in 1985 in Lancaster County, Pennsylvania. She was valedictorian of the Pequea Valley High School class of 2004 in Kinzers, Pennsylvania. In 2008, she earned a Bachelor of Science degree in Chemistry from Pennsylvania State University in State College, Pennsylvania. Afterwards, she joined the research lab of Professor Daniel R. Gamelin in 2009 at the University of Washington in Seattle, Washington. In the fall of 2012, she married Tyler James Thorsen, a fellow PSU alum and graduate student in the Atmospheric Science Department at the University of Washington. She earned a Doctor of Philosophy in Chemistry in 2014.